Time-Resolved Magneto-Optical Kerr Effect for the Study of Ultrafast Magnetization Dynamics in Magnetic Thin Films

A THESIS

SUBMITTED TO THE FACULTY OF THE
UNIVERSITY OF MINNESOTA

BY

Dustin Michael Lattery

IN PARTIAL FULFILLMENT OF THE REQUIREMENTS

FOR THE DEGREE OF

DOCTOR OF PHILOSOPHY

Adviser: Xiaojia Wang

May 2020

ACKNOWLEDGEMENTS

In order to make my way through my graduate education, it's important to acknowledge all of the help I've gotten along the way. My time at the University of Minnesota has been filled with all sorts of collaborations, to the point where it would be difficult to thank everyone that helped to guide me and provided an immeasurable amount of assistance in the pursuit of my doctorate.

I'd first like to thank all of the members (both current and former) of the MNTTL for all of their assistance. Prof. Hu Zhang helped getting me started in research, specifically his help setting up the monochromator system in the MNTTL and assistance in measuring silver nanorod samples (provided by Dr. Funing Chen and Prof. Yiping Zhao). Prof. Jie Zhu almost singlehandedly started me on the path that led to the research that makes up the majority of this thesis. While I have made some updates and adjustments to the TR-MOKE method to measure ultrafast dynamics, he set up the initial measurement and initiated the concept of measuring ultrafast magnetism with the MNTTL laser system. Dr. Xuewang Wu started in the lab before me and was always available whenever I had a question about the laser setup or TDTR measurements. Haidong Ma helped with the design and machining of the components for our high temperature stage. Daehyun Kim also provided additional help later down this path. And finally, Saichao Dang, Chi Zhang, Matthew Thompson, Daehyun Kim, Dingbin Huang, Yingying Zhang, Lis Stolik, and Bill Peria taught me by allowing me to teach them. Having to think about concepts enough to explain them to other researchers is the final step necessary to becoming a professional in a specific research area.

Just as important to my education were my collaborators in research. Mingeon Kim, Jongin Choi, and Prof. Bong Jae Lee provided the simulations of silver nanorods with FDTD to finally complete my initial research into optics. Dr. Junyang Chen created magnetic thin-film transducers for thermal TR-MOKE measurements which provided an opportunity for me to provide information for my first publication. Dr. Delin Zhang prepared the majority of the samples for my measurements presented in this work. Dr. Tao Qu helped with micromagnetic simulations of magnetization to compare to TR-MOKE results. Prof. Paul Crowell has provided a significant amount of help to interpret TR-MOKE data and acted as an initial audience to my theories and interpretations of magnetization dynamics. Prof. Randall Victora provided physical explanations and simulations to understand the TR-MOKE results and taught the course that acted as my original magnetic background. Prof. Jian-Ping Wang also added to my education not just by teaching me about spintronics, but also provided connections to Delin Zhang, Junyang Chen, Xudong Hang, and many of his students and post-docs that helped me along the way.

Lastly, I would like to acknowledge the help that my graduate committee has provided to me. Prof. Terry Simon has been teaching me since my undergraduate education and continues to be gracious with his help whenever I should need it. Prof. Chris Hogan as the director of graduate studies has not only helped by answering my questions about graduate education, but also by motivating me to branch out and help within the department. Prof. Jian-Ping Wang has already been acknowledged, but I think it is important to acknowledge the amount of work he has done for my benefit. My advisor Prof. Xiaojia Wang motivated me into not only researching a new and exciting topic but also to transfer into the doctoral program and allowed freedom to research projects that I found interesting. Finally, although John Gardner is not on my committee, he has helped me through every step of the graduate process, and I am very thankful.

DEDICATION

This thesis is dedicated to my friends and family. This time of my life has been an adventure for all of us. Although it looked like it would never end, it has, and it is only because of you. Thank you for putting up with me in my highs and lows.

ABSTRACT

As traditional complementary metal oxide semiconductors (CMOS) struggle to extend previous industrial trends, new technologies must be researched and delivered. One of the most important aspects that must be considered is the transport of heat within the material. By advancing the design of materials and interfaces, heat transfer within electronic devices can be improved. At the same time, novel technologies that rely on the magnetism of thin films also need to have their transient magnetic behavior optimized. By measuring the magnetic response of the materials, engineers can select the best-matched materials to design and fabricate devices with lower power consumption and higher processing speed, and thus improved performance. Such material transport studies require new methods and metrology development that can provide highly sensitive and accurate characterization of the materials. The time-resolved magneto-optical Kerr effect (TR-MOKE) technique is capable of probing both thermophysical and magnetic properties of a variety of materials, and it offers superb spatial (micrometer) and temporal (sub-picosecond) resolutions. In this thesis, information about this technique will be discussed including thorough examples of its applications in the study of magnetization dynamics.

TABLE OF CONTENTS

LIST OF TABLES

LIST OF FIGURES

LIST OF ABBREVIATIONS

3TM (Three-Temperature Model)

AGM (Alternating Gradient Magnetometry)

CMOS (Complementary Metal-Oxide-Semiconductor)

DOS (Density of States)

EOM (Electro-Optical Modulator)

EHF (Extremely-High Frequency)

FMR (Ferromagnetic Resonance)

HAMR (Heat-Assisted Magnetic Recording)

LLB (Landau-Lifshitz-Bloch)

LLG (Landau-Lifshitz-Gilbert)

MOKE (Magneto-Optical Kerr Effect)

MRAM (Magnetic Random-Access Memory)

PMA (Perpendicular Magnetic Anisotropy)

PPMS (Physical Property Measurement System)

SAF (Synthetic Antiferromagnet)

SNR (Signal-to-Noise Ratio)

SOT-MRAM (Spin-Orbit Torque MRAM)

SQUID (Superconducting Quantum Interference Device)

STT-MRAM (Spin-Transfer Torque MRAM)

TDTR (Time-Domain Thermoreflectance)

TR-MOKE (Time-Resolved Magneto-Optical Kerr Effect)

VSM (Vibrating Sample Magnetometry)

XRD/XRR (X-ray Diffraction/ X-Ray Reflectivity)

LIST OF SYMBOLS

$\hbar$: Reduced Planck's constant (erg s in Gaussian Units (CGS) or J s in SI)

α: Gilbert Damping (dimensionless)

γ: Gyromagnetic ratio (rad s^{-1} Oe^{-1} in CGS or rad s^{-1} $Tesla^{-1}$ (rad s^{-1} T^{-1}) in SI)

ε: Electrical Permittivity (F m^{-1} in SI)

η_s: Spin polarization (dimensionless)

η: Magnetic Relaxation Rate (Hz or s^{-1}) – inverse of τ

θ: Polar Equilibrium Direction of Magnetization (rad)

θ_H: Polar Direction of external magnetic field (rad)

θ_k: Kerr rotation angle (degrees or radians)

Λ: Thermal conductivity (W m^{-1} K^{-1})

λ_{LL}: Landau-Lifshitz relaxation (electromagnetic units (emu) cm^{-3} s^{-1} Oe^{-1} in CGS)

μ: Atomic moment (emu in CGS or A m^2 in SI)

μ_0: Magnetic permeability of free space (H m^{-1})

μ_m: Magnetic moment (emu in CGS or A m^2 in SI)

ξ: Scattering length (cm)

τ: Relaxation Time (ps)

φ: Azimuthal Equilibrium Direction of Magnetization (rad)

φ_H: Azimuthal Direction of external magnetic field (rad)

ω: Angular resonance frequency (rad s^{-1})

C: Volumetric heat capacity (J m^{-3} K^{-1})

e: Electron charge (statcoulomb in CGS or C in SI)

f: Resonance Frequency (GHz)

F: Free magnetic energy density (erg cm^{-3} in CGS or J m^{-3} in SI)

G: Interfacial conductance (W K^{-1})

H_{eff}: Effective internal magnetic field (Oe in CGS or A m^{-1} in SI)

H_{ext}: External (applied) magnetic field (Oe in CGS or A m^{-1} in SI)

$H_{k,eff}$: Effective anisotropy field (Oe or A m^{-1})

J_c: Critical switching current (A cm^{-2} in CGS or A m^{-2} in SI)

J_s: Spin current (A cm^{-2} in CGS or A m^{-2} in SI)

k_B: Boltzmann constant (erg K^{-1} in CGS or J K^{-1} in SI)

M: Magnetization (emu cm^{-3} in CGS or A m^{-1} in SI)

m: Normalized magnetization (dimensionless)

M_s: Saturation magnetization (emu cm^{-3} in CGS or A m^{-1} in SI)

Q: Magneto-optical constant (dimensionless)

T_C: Curie Temperature (K)

t_F: Free magnetic layer thickness (cm in CGS or m in SI)

CHAPTER 1: INTRODUCTION

This chapter is an introduction to the state of magnetic transport properties and how they can be measured with a TR-MOKE system. Parts of this introduction were originally published as a book chapter:

1. Lattery, D., Zhu, J., Huang, D., and Wang, X.J., "Ultrafast Thermal and Magnetic Characterization of Materials Enabled by the Time-Resolved Magneto-Optical Kerr Effect", invited IOP Book Chapter in Nanoscale Energy Transport: Emerging Phenomena, Methods and Applications (2020), pp. 9-1 to 9-30.

Transport properties (e.g., electrical conductivity, thermal conductivity, and the transfer of magnetic moment of materials) are of critical importance to a broad range of engineering applications. In this thesis, I will highlight the state-of-the-art Time-Resolved Magneto-Optical Kerr Effect (TR-MOKE) methodology, based on the ultrafast pump-probe technique, for characterizing magnetic transport properties of several representative materials. These materials are of technological importance, serving as building blocks for the next generation of electronic, spintronic, and data storage devices. For decades, these device components have been manufactured following Moore's law which states that the number of transistors per chip should double every two years [1]. Semiconductor industries have pushed to maintain this trend, but they are finally being limited by the power density of device operation, or more simply, heat extraction [2]. By moving electrons through more closely-spaced transistors at faster switching speeds, these devices are producing progressively more dense heat loads, imposing a continually-growing need for thermal management (the capability of redistributing and removing heat). The solutions proposed by researchers have followed two main paths: (1) developing new technologies that require less power and (2) engineering new materials and better interfaces that can be scaled down without increasing heat generation or impeding heat transfer.

Following the first path, the field of spintronics (spin-electronics) has proven a promising direction since the discovery of giant magnetoresistance [3,4]. At the fundamental level, spintronics

focuses on advancing materials by manipulating the magnetization (or spin) in magnetic materials to achieve so-called “beyond CMOS” (complementary metal oxide semiconductor) technologies. Theoretically, spintronic devices have the benefits of minuscule amounts of power required for switching, fast switching speeds, and non-volatility (i.e., they do not require power to retain information), making them ideal for both processing and memory. Spintronics have already been adopted in widespread applications. The most common application can be found in magnetic random-access memory (MRAM), which has rapidly gone from utilizing a magnetic field to switch memory [5], to spin-transfer torque (STT-MRAM) [6,7], and to spin-orbit torque (SOT-MRAM), [8,9] making use of cutting-edge physics along the way. The unique advantages of these memory technologies have further enabled advanced applications in all-spin logic (using only spin transport for computation) [10,11], probabilistic computing [12], spin torque oscillators [13-16], and heat-assisted magnetic recording (HAMR) [17-19], among others. While these technologies are all proven, future generations will require an optimization of material properties depending on the application. It is crucial to understand the magnetic properties (such as the Gilbert damping α) of materials at short time scale (e.g., sub-nanosecond) to guide further research and development.

The characterization of magnetic properties up to this point has been dominated the technique of ferromagnetic resonance (FMR) [20]. FMR uses a microwave signal to excite a magnetic sample. The change in magnetic susceptibility of the sample is measured through a change in microwave absorption as the sample goes through its resonance condition, during which, the external field and frequency agree with the theory pioneered by Kittel [21]. The resulting microwave absorption, as a function of frequency or field, can be fitted to a Lorentzian or anti-Lorentzian function, where the width of the Lorentzian (the so-called linewidth) is dependent on the damping α [22]. While this highly versatile technique has adapted through advanced techniques (such as stripline FMR among others [23]), it has difficulty characterizing new technologically relevant materials with large perpendicular magnetic anisotropy (PMA). The large anisotropy requires a high-power input to

excite the magnetization, and the relatively large damping of metallic materials leads to large linewidths. The search for alternative measurement techniques has been motivated by these challenges faced by FMR.

For these emerging materials and technologies, ultrafast laser-based pump-probe techniques provide sensitive, powerful, and high-throughput capabilities for the study of transport in materials. The high temporal resolution of the ultrafast pump-probe method makes it suitable for studying dynamics occurring on time scales from hundreds of femtoseconds (fs, 10^{-15} s) to several nanoseconds (ns, 10^{-9} s), for both thermal and magnetic transport processes. Time-resolved magneto-optical Kerr effect (TR-MOKE), a system initially invented to probe magnetization dynamics [24,25], can be extended to thermal measurements by taking advantage of the temperature-dependent magnetization of the transducer [26,27]. For magnetic transport studies, TR-MOKE can detect magnetization dynamics of materials with superb spatial (diffraction-limited beam spots) and temporal (sub-picosecond) resolutions. Particularly, the use of optical pumping and detection in TR-MOKE allows it to capture the ultrafast magnetization of "hard" materials (with large magnetic anisotropy) that are not detectable using conventional FMR methods.

In this thesis, I will detail my research focusing on measuring the magnetization dynamics of magnetic thin films. Specifically, I will focus on 3 main projects: a study of the optimization of TR-MOKE signal of perpendicular magnetic materials; annealing temperature-dependent magnetic properties of tungsten-seeded CoFeB; and the coupling between acoustic strains and magnetization dynamics in Co/Pd multilayers. I will also discuss a few projects that I started that will be researched more by new PhD students in my group. The results of this research can be used to guide development and optimization of new magnetic technologies.

CHAPTER 2: THEORY

The theory presented in this section will cover the critical concepts used in ultrafast magnetization dynamics. While many of the theories are derived starting from the quantum theory, and indeed some concepts in spintronics only make sense with a background in quantum mechanics and solid-state physics, the purpose of this section is to present the theory in a semi-classical approach. The study of ultrafast magnetism has been dominated in the past by physicists and electrical engineers, but because I had no experience in either field prior to this research, I have tried to develop my own understanding as a mechanical engineer. In other words, my goal here is to present critical information in terms that can be understood by most individuals with an engineering or scientific background.

2.1 Equations for Precessional Magnetic Motion

The concept of angular momentum is often a case of confusion when it is initially taught in undergraduate level physics courses. It is often useful to discuss a simple object, such as a top, to introduce this concept. When a top is spun, angular momentum keeps the top rotating without falling over, thereby acting against gravity by resisting a change to its angular momentum (i.e. its desire to keep spinning keeps it from falling over). When the rotating body is tilted and its center of rotation does not align with the direction of gravity, a torque is generated (a change in angular momentum). The imposed torque will cause the rotational axis of the top to continuously change, so the rotational axis will trace a circular path in space as it rotates. This continuously changing axis of rotation is called “precession”, a concept that is used to describe the movement of the earth all the way down to the motion of the direction of magnetization in a material.

In the field of magnetism, the magnetization of ferromagnetic materials is associated with the angular momentum or “spin” of the electrons. Analogous to how a torque is imparted on a rotating

top, an effective internal magnetic field ($\mathbf{H}_{\text{eff}}$) can provide a torque ($\mathbf{T}$) on the angular momentum inside magnetic materials. The torque acting on a magnetic moment ($\mu_{\mathbf{m}}$) is given by the equation:

$$\mathbf{T} = -\mu_{\mathbf{m}} \times \mathbf{H}_{\text{eff}} \tag{2.1}$$

Through a conservation of angular momentum ($\mathbf{L}$), the change in angular momentum in time must be equal to a torque, or in other words:

$$\frac{d\mathbf{L}}{dt} = -\mu_{\mathbf{m}} \times \mathbf{H}_{\text{eff}} \tag{2.2}$$

Averaging the magnetic moment over an entire system, the magnetic moment can be replaced by the magnetization of the system ($\mathbf{M}$).

$$\frac{d\mathbf{M}}{dt} = -\gamma \mathbf{M} \times \mathbf{H}_{\text{eff}} \tag{2.3}$$

This equation describes "Larmor Precession" or the precession of magnetization around a magnetic field and introduces the concept of the gyromagnetic ratio (γ), which is a ratio of the magnetic moment to the angular momentum ($\gamma = L/\mu_{\mathbf{m}}$). The value of γ changes from material to material through a dimensionless g-factor (a factor that represents the total magnetization for a material system which is approximately equal to 2 for an electron).

From Eq. 2.3, if the magnetization vector is parallel to $\mathbf{H}_{\text{eff}}$, then $\mathbf{M}$ will not change in time ($\mathbf{M}$ is in equilibrium). This equilibrium should only happen when an associated energy is minimized. For magnetism, this equilibrium occurs when the magnetic free energy density (F) of the system is minimized with respect to $\mathbf{M}$. The magnetic free energy, as introduced by Stoner and Wohlfarth [28,29] is typically represented by the sum of several energy terms:

$$F = F_0 + F_Z + F_K + F_D \tag{2.4}$$

where F_0 is an offset (the constant energy term that does not impact dynamics), F_Z is the Zeeman energy (energy from an external magnetic field), F_K is the anisotropy energy (an energy related to the magnetic properties of the material), and F_D is the demagnetization energy (energy from an internal magnetic field depending on the shape of the sample). The concept of equilibrium when $\mathbf{M}$ is parallel to $\mathbf{H}_{eff}$ is captured by the definition of effective field in Eq. 2.5.

$$\mathbf{H}_{\text{eff}} = -\nabla_{\mathbf{M}} F \tag{2.5}$$

While Eq. 2.3 is useful to understand the concept of magnetization (or spin) precession inside of a magnetic material, the lack of a relaxation mechanism makes it unphysical. One of the first methods to account for the damping in a system, the Landau-Lifshitz equation, assumed that the magnetization within a system was constant ($\|\mathbf{M}\| = M_s$, where M_s is known as the saturation magnetization), and simply added a relaxation constant (λ_{LL}, units of emu cm^{-3} s^{-1} Oe^{-1}) to allow for the system to relax towards the equilibrium direction along $\mathbf{H}_{eff}$.

$$\frac{d\mathbf{M}}{dt} = -\gamma \mathbf{M} \times \mathbf{H}_{\text{eff}} - \frac{\lambda_{\text{LL}}}{M_s^2} \mathbf{M} \times \left(\mathbf{M} \times \mathbf{H}_{\text{eff}} \right) \tag{0.1}$$

This equation simply provides a phenomenological method of describing the damping process in dynamic magnetism. The processes that cause a system to relax (a few of which are discussed in Section 2.3) are combined into this single damping term. Other methods of accounting for this damping process have been proposed, such as the most widely used equation developed by Gilbert which theorizes a "viscous" damping that depends on the "velocity" of the changing magnetization as captured in the Landau-Lifshitz-Gilbert (LLG) equation, shown in Eq. 2.7 [30].

$$\frac{d\mathbf{M}}{dt} = -\gamma \mathbf{M} \times \mathbf{H}_{\text{eff}} + \frac{\alpha}{M_s} \left(\mathbf{M} \times \frac{d\mathbf{M}}{dt} \right) \tag{0.2}$$

The dimensionless damping constant presented in Eq. 2.7 (α, the Gilbert damping) is the typically reported value of damping constant that describes the dynamics in technologically relevant materials. The values of this constant range from 10^{-5} to 0.1 [31,32], largely depending on the material studied, the thickness of the material, growth conditions, and temperature.

It is often useful to predict the behavior of the magnetization within magnetic materials with the appropriate anisotropy and Gilbert damping through computer simulations (i.e., numerical methods), but the nature of the LLG equation in the form of Eq. 2.7 is not conducive to numerical simulation. Through the process outlined in Appendix A, the LLG equation can be converted into a form similar to the original Landau-Lifshitz equation:

$$\frac{d\mathbf{M}}{dt} = -\frac{\gamma}{1+\alpha^2}\mathbf{M}\times\mathbf{H}_{\text{eff}} - \frac{\alpha\gamma}{M_s\left(1+\alpha^2\right)}\mathbf{M}\times\left(\mathbf{M}\times\mathbf{H}_{\text{eff}}\right). \qquad 0.3$$

By separating the Cartesian components of the vectors of **M** and $\mathbf{H}_{\text{eff}}$, the cross products can be readily solved, and the resulting differential equation is only first order in time. While there is an entire field originally established by William Fuller Brown at the University of Minnesota which combines the solution of this differential equation with a finite element method (micromagnetic simulations) [33], "simulations" in this thesis refer to the simulation of a single magnetization (single-spin or macromagnetic simulations) unless otherwise indicated.

2.2 The Importance of Gilbert Damping: Macrospin Simulations

Most modern applications of spintronics rely on binary states of magnetization (i.e., up and down) for computation. Magnetic storage is an example where data is stored in bit sequences made up of a series of "1s" and "0s" made of magnetic grains with magnetization pointing either up or down. Switching between these two states (or being able to write data) is a crucial aspect of

consumer devices. As such, it is critical to understand how the different aspects of the LLG equation impact the switching speed inside a magnetic film.

For the simplest case where an external field is applied to the magnetic system at an initial time, the magnetization will feel a large torque due to the $\mathbf{M}\times\mathbf{H}_{eff}$ term. The speed of the magnetization should depend on the amplitude of this torque (which is represented in the first part of the Eq. 2.7). At the same time, the 2nd term in Eq. 2.7 will resist a change in the magnetization with a strength that is proportional to α. To further understand the influence of damping on precession, I will discuss the influence of a few parameters through LLG simulations.

The first thing I will present is the influence of torque on precession duration. I will change the torque by modifying the $\mathbf{M}\times\mathbf{H}_{eff}$ cross-product by varying the initial angle of the magnetization (θ_i). By increasing the angle between the two terms, the rate of the change in magnetization should increase with increasing angle. For the sake of these plots, I will compare the times for the magnetization to achieve 99.99% of the switching process (the magnetization goes from θ_i to the equilibrium direction).

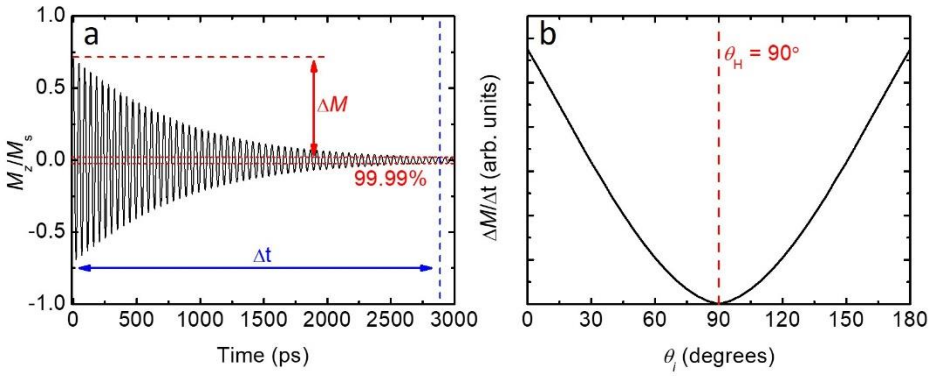

Figure 2.1 Macrospin simulation showing how the rate of change of magnetization changes with varying initial conditions. (a) The time trace of the *z*-component of magnetization as a function of time for the case where the magnetization is 45 degrees from the equilibrium direction. (b) The rate of change of magnetization (where ΔM and Δt are defined in (a) as a function of initial angle (θ_i) from equilibrium (which in this case is the direction of external field (θ_H)).

As shown by these plots, while the damping remains consistent, increasing the torque helps to speed up switching. Counterintuitively, increasing the damping for a specific torque also helps to increase the switching rate. While it takes a longer time to partially switch, once switched, the system is overdamped and cannot oscillate around the equilibrium. This is particularly useful in magnetic storage applications.

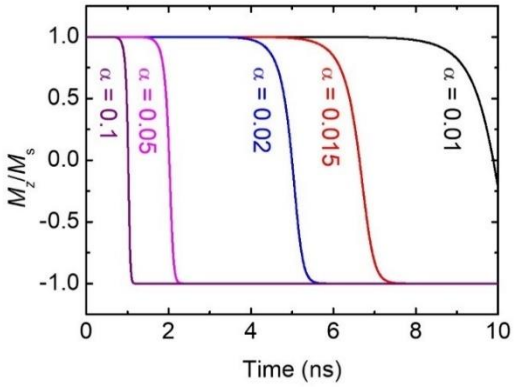

Figure 2.2 Macrospin simulation of the switching process from up (positive values of M_z/M_s) to down (negative values of M_z/M_s) for various values of α. Higher values of α complete the switching process faster.

Based on these results, it might seem useful to always maximize the damping parameter for applications, but for STT-MRAM, the switching behavior is caused by an applied spin current. This spin current can be accounted for through the addition of a so-called "Slonczewski" term in the LLG, as in Eq. 2.9 [6,34,35].

$$\frac{d\mathbf{M}}{dt} = -\frac{\gamma}{1+\alpha^2}\mathbf{M}\times\mathbf{H}_{\text{eff}} - \frac{\alpha\gamma}{M_s\left(1+\alpha^2\right)}\mathbf{M}\times\left(\mathbf{M}\times\mathbf{H}_{\text{eff}}\right) + \frac{\hbar}{2e}\frac{\eta_s J_s \gamma}{t_F M_s^2\left(1+\alpha^2\right)}\left(\mathbf{M}\times\mathbf{M}\times\mathbf{m}_{\text{fixed}}\right) \quad 0.9$$

The last term introduces a few new variables associated with the spin current ($\hbar$ is the reduced Planck constant, e is the electron charge, η_s is the spin polarization, t_F is the thickness of the layer, J_s is spin current density, and $\mathbf{m}_{\text{fixed}}$ is the direction of the magnetization in the polarizing layer), but is otherwise the same as Eq. 2.7. The last term introduces an anti-damping-like torque (a torque

that acts against damping) into the system that will always depend on an external magnetic moment ($\mathbf{m}_{\text{fixed}}$). Just to exhibit how this differs from a purely field-switched system, Fig. 2.3 illustrates two different switching scenarios, a field-switched and a current switched system.

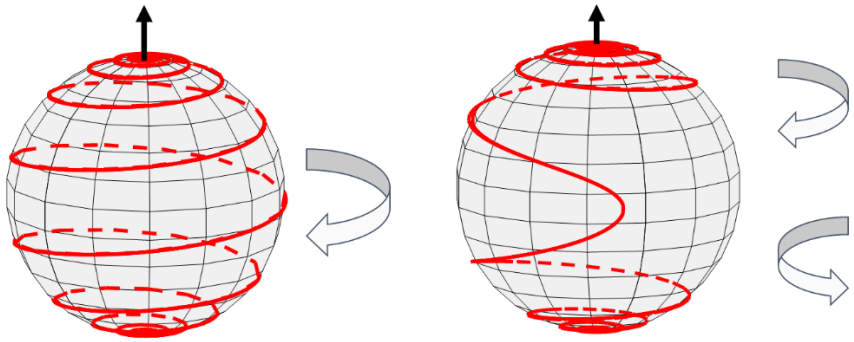

Figure 2.3 Macrospin simulation of switching. The spheres indicate a sphere of constant M_s in 3D cartesian space. The black arrows show the initial direction of magnetization and the red lines show the path of magnetization as it switches from pointing up to down. (a) is the switching path for field-assisted switching while (b) is a spin-transfer torque switching.

While the field-switched scenario always follows the same path, the current-switched system changes direction. This is because the spin-transfer torque changes sign and becomes a damping-like torque past a certain point. To account for this, a simplification has been proposed that provides a critical switching current for a perpendicular film in terms of previously defined magnetic properties and the effective anisotropy field ($H_{\text{k,eff}}$ a measure of the field required to rotate the magnetization from the easy axis to a hard axis) that is given by [36]:

$$J_c = \frac{2eM_s t_F \alpha}{\hbar \eta_s} H_{\text{k,eff}} \,. \qquad 2.10$$

This equation indicates that the critical spin current (J_c) has α in the numerator meaning that reducing damping is one method of reducing the energy required (related to J_c) to switch a device with spin-transfer torque.

To summarize, for applications such as MRAM where the only goal is to switch a magnetization with the smallest amount of current possible, it is beneficial to reduce the amplitude of α, whereas for magnetic storage, a large α helps to prevent the magnetization from spontaneous switching and thus speeds up writing. For both cases, understanding this material property α is critical to developing consistent devices.

2.3 Damping Mechanisms

As discussed in the previous section, the damping parameter is one of the most important material properties for many spintronic devices. To better understand this phenomenological parameter, it is helpful to understand a few of the many theories that have been presented to better understand the magnetic damping. These physical mechanisms provide much of the information for what we understand as the contributors to the damping.

2.3.1 Kamberský Damping: Spin Orbit Dissipation

One of the most cited contributors to the field of predicting magnetic damping through computational methods is Vladimír Kamberský. As a method to describe the purely intrinsic damping mechanisms, Kamberský described two possible intrinsic mechanisms that cause the energy from magnetization to damp [37]. The first mechanism is a dissipation from the magnons (a quantized packet of spins described as a wave) directly into phonons (a quantized packet of lattice vibrations) via spin-flip scattering events as described by Elliott and Yafet [38]. The other mechanism discussed utilizes an understanding of the shifting electron orbital shifts due to a change in magnetization.

This torque correlation (or breathing Fermi surface) model describes the change to the electron density of states (the available states at a given energy that are available) for up and down spins and is used as a first-principles method of predicting the damping in metals [39-42]. By incorporating both the interband (conductivity-like) and intraband (resistivity-like) scattering, the

damping can be predicted for various electron scattering times (related to the temperature of the material) [43,44].

This has been previously used to predict the damping in technologically relevant materials such as $L1_0$-ordered alloys of FePd [45-48] and FePt [46,47,49] and found to have a strong dependence (roughly quadratic) on the spin-orbit coupling (a relativistic coupling between the spin of an electron and its orbit). Because the spin-orbit coupling also determines the amplitude of the magnetocyrstalline anisotropy [50], this means that a material with large spin-orbit interactions (such as alloys with the heavy metal Pt) tend to have both high anisotropy and damping. Outside of the materially-dependent properties that are captured by the Kamberský model, there are other extrinsic methods of damping that can be tuned based on the operation conditions of the material.

2.3.2 Two-Magnon Scattering

The previous discussion of damping has been damping within a single magnetic element (single magnetic domain) with no imperfections, which is not possible in real materials and devices. As magnetic solids begin to be discussed, it becomes important to understand the impact of microscopic magnetic interactions between multiple magnetic domains within a magnetic solid. One such resulting physical phenomena is the spin wave, a magnetic wave that propagates through a solid via interacting magnetic domains as pictured in Fig. 2.4.

A quantized spin-wave packet is known as a "magnon" and is a quasiparticle that obeys Bose-Einstein statistics (a boson). The relationship between spin wave and magnon is analogous to that between a lattice vibration and a phonon. The concept of a magnon was originally used to describe the temperature dependence of ferromagnets at low temperature (Bloch $T^{3/2}$ law), but it has become important to understand these quasiparticles to describe damping processes in magnetic devices.

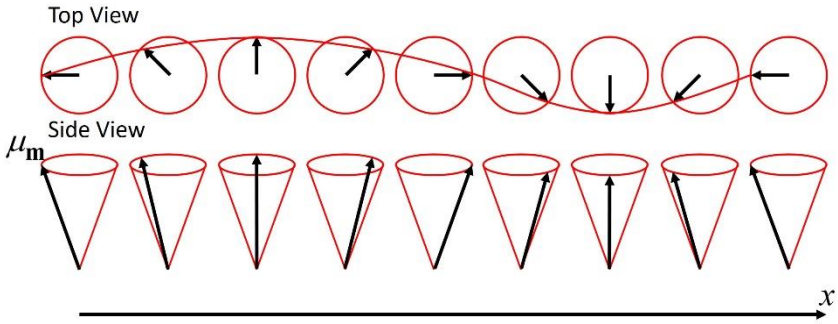

Figure 2.4 Illustration of a spin wave. Due to ferromagnetic coupling between individual spins in a solid, a perturbation of a single magnetic moment (μ_m) will cause a movement of neighboring moments. This will lead to a spin wave with a wavelength (indicated by the line in the top view) determined by the material properties. A quantization of spin waves with a set energy is called a magnon.

As with a discussion of any quantized energy carrier in solid state physics, a discussion of energy flow due to magnons begins by understanding the magnon dispersion (a distribution of the magnon energy given in terms of angular frequency ω with respect to the reciprocal lattice vector **k**). The derivation of this dispersion has been briefly discussed in many papers [51-53] and is also carried out in Appendix C for thin films with perpendicular magnetic anisotropy. A plot of an example magnon dispersion is shown in Figure 2.5.

At **k** = 0 the frequency indicates the uniform precession mode (i.e. the frequency for the case where the magnetization of the film is precessing at the same frequency). This **k** = 0 mode is the mode of interest for most discussions of magnetization dynamics, but when magnons are introduced, there is also the possibility of the existence of degenerate modes (modes with the same energy). Through two-magnon scattering (named because there are only two magnon states involved in the process) a **k** = 0 magnon scatters into a degenerate **k** ≠ 0 magnon. A non-zero wavevector indicates that this new magnon mode has a momentum associated with it (i.e., the energy of the magnon is moving within or out of the system). Because momentum is not conserved

in this process, it requires an impurity to scatter the magnon. A few of the relationships for various impurities are discussed more elsewhere [53].

For a magnon dispersion in a magnetic thin film (the focus of this work) typically only supports magnons in the two in-plane dimensions (the out-of-plane is too thin to support multiple domains), so we can think of the magnon dispersion as a surface as shown in Fig. 2.5. If a constant energy surface is superimposed over the surface, we will see a "figure 8" shape where the frequency of a $\mathbf{k} = 0$ magnon (ω_0) is equal to that of a $\mathbf{k} \neq 0$ magnon ($\omega_{\mathbf{k}}$) as indicated by the dotted red line in Fig. 2.5.

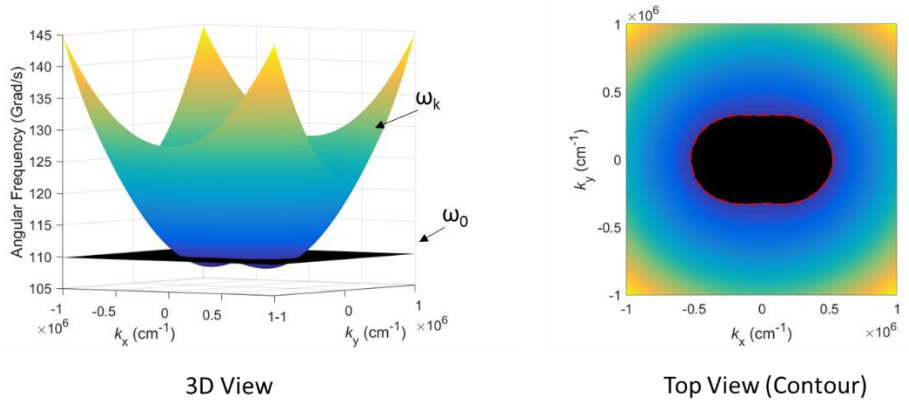

Figure 2.5 Figure of the magnon dispersion in a perpendicular magnetic thin film. The surface denoted by $\omega_{\mathbf{k}}$ indicates the frequency of a magnon with a wavevector given by **k** (a vector made of components k_x and k_y). The surface indicated by ω_0 is the uniform precession frequency. The overlapping part of these two surfaces indicates the degenerate magnon modes (indicated by the dotted red line in the contour).The magnetic properties are based on the W/CoFeB sample in Chapter 4 and an exchange of 10^{-6} erg cm^{-1}.

The length of this path indicates the number of available modes for the uniform magnon to scatter into. With more available modes, the probability of a scattering event becomes more likely (also increasing impurities), so the damping from this process will increase. Appendix C discusses how to convert a scattering probability into a relaxation time, but the concept of the density of states (DOS) can also help when comparing the scattering in two different scenarios. The DOS is the measure of the number of available modes to scatter into at a given energy. For TR-MOKE

measurements, it is often helpful to know how the likelihood of two-magnon scattering changes with external field amplitude (H_{ext}) and direction (θ_H defined in Appendix B), such as in Fig. 2.6.

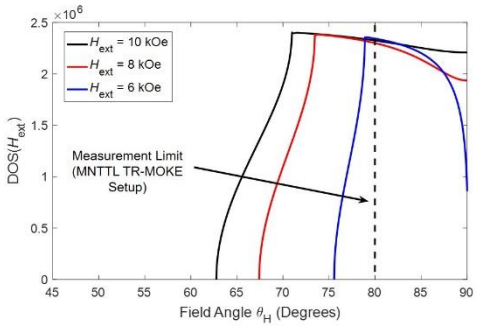

Figure 2.6 Figure of the magnon Density of States (DOS) in a perpendicular magnetic thin film as a function of external field direction (θ_H) at various H_{ext} (6 kOe which is near $H_{k,eff}$ of 6.1 kOe, 8 kOe, and 10 kOe). The vertical dotted line indicates the measurement limitations of the Minnesota TR-MOKE setup.

Based on Fig. 2.6, a critical value of θ_H occurs where the DOS goes to 0 (there are no available scattering states, which occurs when the magnetization is 45° or less from the out-of-plane direction), but this point is always above our measurement limitations (indicated by the dashed line). Because of this, for a typical TR-MOKE measurement in the Micro/Nano Thermal Transport Lab (MNTTL), two-magnon scattering should be considered unless other damping mechanisms are shown to be more dominant.

2.3.3 Multi-Magnon Scattering

The previous section discussed the influence of two-magnon scattering on damping, which is crucial for the understanding of damping in TR-MOKE measurements. When this concept is expanded to account for three-magnon scattering (one magnon scattering into two states where energy and momentum are conserved), 4-magnon scattering (two magnons scattering into two other magnon states where energy and momentum are conserved), or any other scattering process, one might expect the influence of these to also be important. In fact, it is difficult to accurately predict the influence of these complex events purely based on TR-MOKE measurements where

temperature change is a critical aspect of the measurement. Groups have simulated these events, such as the amount of four-magnon scattering as a function of θ_H for high-power FMR measurements [54], but further cross-collaboration between simulation and experimental groups needs to exist to confirm theoretical trends.

2.3.4 Spin Pumping

Up to this point, the damping mechanisms have been purely related with the material under study, but since technologically relevant materials are often built in stacks (layers of thin films stacked together) it is also important to understand the influence of surrounding materials to the damping. At the interface of between a ferromagnetic material and a heavy metal, the precessing magnetization can induce an interfacial spin current to be pumped into the metal. This spin pumping leads to a loss of angular momentum, or a magnetic damping. Spin pumping as a mechanism of damping was originally theoretically proposed by Yaroslav Tserkovnyak and Arne Brataas [55], and was quickly used to explain experimental results [56,57]. For the samples used in this thesis, it is difficult to separate the influence of spin pumping from other damping mechanisms because it requires information of the changing damping with changing magnetic layer thickness. For interfacial magnetic anisotropy, such as for our CoFeB samples, this process has been done [58], but it is difficult to separate the effects of enhanced scattering resulting from the interface from spin pumping. For FePt, FePd, and Co/Pd samples, the effect of varying thickness effect could be distinguished with further research.

2.3.5 Inhomogeneous Broadening

The final form of relaxation that I will discuss here is probably the least understood. Inhomogeneous broadening is the name given to any form of destructive interference caused by a distribution in magnetic properties in the sampled area of the material. This can be understood by considering the sum of damped sinusoids with slightly different frequencies, as shown in Fig. 2.7.

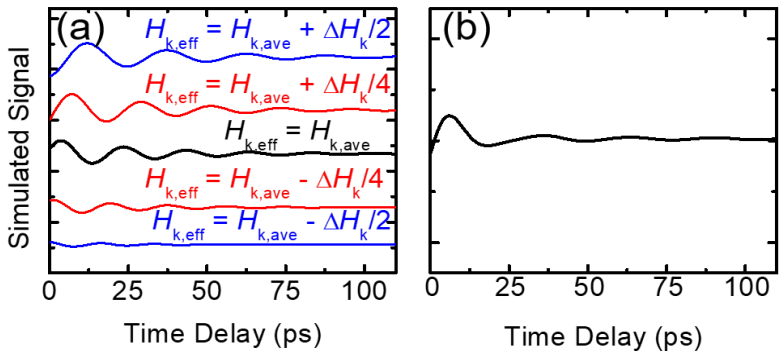

Figure 2.7 A visual representation of inhomogeneous broadening. (a) The simulated macrospin signal for a magnetic system with a value of H_{keff} that follows a Gaussian distribution showing a moderate amount of damping. (b) The sum of all signals showing an enhanced damping effect due to the destructive interference of various modes acting simultaneously.

As shown in this figure, even though all the different signals have the same relaxation rate, the slight difference in frequency impacts the sum drastically. The resulting sum has an apparent damping that is much larger than the input. In this sense, the inhomogeneous broadening is not a real damping, but an apparent one resulting from the measurement of a large population of oscillating systems.

In magnetic thin films, even small defects in the material can cause a noticeable change in magnetic properties. For example, for a magnetic layer grown with sputtering, the thickness of the layer can vary across a small area which will lead to a change in M_s, $H_{k,eff}$, and even α. We can then treat the system as if it were made of many small "domains" with some amount of distribution in magnetic properties (with the average of all domains being the material property determined over the entire macroscopic system).

CHAPTER 3: EXPERIMENTAL TECHNIQUES

This chapter is a discussion of the TR-MOKE method including a description of the TR-MOKE setup in the MNTTL at the University of Minnesota. Parts of this chapter were originally published as a book chapter:

1. Lattery, D., Zhu, J., Huang, D., and Wang, X.J., "Ultrafast Thermal and Magnetic Characterization of Materials Enabled by the Time-Resolved Magneto-Optical Kerr Effect", invited IOP Book Chapter in Nanoscale Energy Transport: Emerging Phenomena, Methods and Applications (2020), pp. 9-1 to 9-30.

3.1 TR-MOKE

The magneto-optical Kerr effect (MOKE) allows for direct optical measurements of the magnetic state of a material. To reveal the correlation between the optical response and the magnetism of the material, this section will discuss the physical foundation of MOKE measurements, the relationship between TR-MOKE signals and the thermal and magnetic transport properties of thin-film samples, and the typical optical setup of TR-MOKE in the pump-probe configuration.

3.1.1 The Physical Foundation

The magneto-optical Kerr effect, as first described by John Kerr [59], is a process that alters the polarization state of light reflected by a magnetic material. Fundamentally, MOKE stems from the different interactions of left and right-circularly polarized light within a magnetized material. Linearly polarized light can be represented as the sum of equal proportions of left and right-circularly polarized light, and each type of circular polarization will experience a different phase shift and absorption when interacting with a magnetic material. The result of this process is the transformation from a linear polarization to an elliptical polarization upon the reflection of light (or transmission of light, for the analogous Faraday effect), as shown by Figure 3.1.

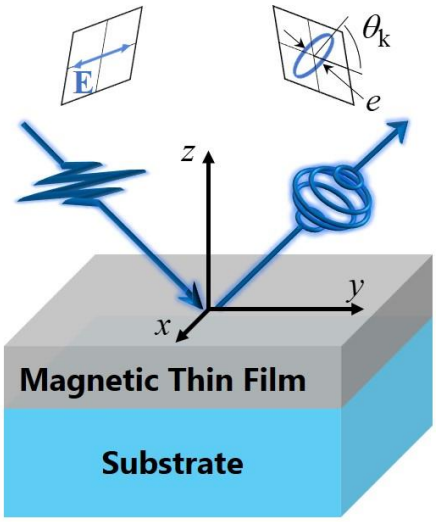

Figure 3.1. An illustration of the complex polarization rotation of reflected light from a magnetic material known as the Magneto-optical Kerr effect (MOKE). The rotation of the polarization, from a linear polarization to an elliptical polarization, is denoted by the Kerr angle (θ_k). The ellipticity is denoted by *e*.

The rotation of linearly polarized light can be described by the response of an electric field vector to the dielectric tensor $\bar{\varepsilon}$, which is given by:

$$\bar{\varepsilon} = \begin{pmatrix} \varepsilon_{xx} & \varepsilon_{xy} & \varepsilon_{xz} \\ -\varepsilon_{xy} & \varepsilon_{yy} & \varepsilon_{yz} \\ -\varepsilon_{xz} & -\varepsilon_{yz} & \varepsilon_{zz} \end{pmatrix}. \qquad 3.1$$

For an isotropic, non-magnetic material, the diagonal components of this tensor are equal ($\varepsilon_{xx} = \varepsilon_{yy} = \varepsilon_{zz}$), and the off-diagonal components are 0. For isotropic magnetic materials, however, the off-diagonal terms are related to the magnetization vector (**M**) through

$$\bar{\varepsilon} = \varepsilon_{xx} \begin{pmatrix} 1 & -iQm_z & Qm_y \\ iQm_z & 1 & -iQm_x \\ -iQm_y & iQm_x & 1 \end{pmatrix} \qquad 3.2$$

where Q is the magneto-optical constant and $m_i = M_i / \|\mathbf{M}\|$ [60-62]. These nonzero off-diagonal terms cause different polarization changes to the opposing circular polarizations. This leads to a complex rotation angle of the polarization, given by $\tilde{\theta} = \theta_k + ie$, where the real part of $\tilde{\theta}$ is the Kerr rotation and the imaginary part is the ellipticity. The variable $\tilde{\theta}$ is also sometimes presented as components of a complex permittivity tensor [63]. The discussion in this chapter will be limited to a discussion of the real component of the Kerr rotation, θ_k, the real rotation of the major axis of polarization upon reflection of linearly polarized light.

At equilibrium, θ_k contains information about the magnetization state in magnetic materials. It is therefore adopted as an alternative method for measuring magnetic hysteresis loops [64], in addition to vibrating sample magnetometry (VSM), alternating gradient magnetometry (AGM), and superconducting quantum interference device (SQUID) measurements. The MOKE response has proven to be powerful for measuring the magnetic properties of nanomaterials, including ferromagnetic monolayers [65]. MOKE microscopy has also been utilized to sense domains in magnetic materials, owing to the large contrast resulting from the opposite Kerr rotation of antiparallel magnetization between domains [66,67]. These optical studies well demonstrate the use of MOKE for investigating magnetostatics (i.e., the magnetization of the sample is not changing in time). In the following sections, I will focus on transient magnetization dynamics induced by ultrafast laser pulses.

3.1.2 Ultrafast Demagnetization Induced by Laser Heating

The application of time-resolved Kerr rotations for ultrafast metrology began as a method to determine the non-equilibrium processes initiated by ultrafast laser excitation in ferromagnetic nickel [68]. Through MOKE, the magnetization within the sample can be measured, providing a window into the temperatures of various energy carriers, including electrons, phonons, and

magnons (wavelike variations in the magnetization). Due to the limitation of using lasers with pulse durations on the order of tens of picoseconds, early TR-MOKE measurements of ferromagnetic materials were unable to directly show these temperatures of carrier populations out of equilibrium with each other (the non-equilibrium regime) [69]. With the new application of femtosecond laser pulses (~60 fs), Beaurepaire *et al*. were able to capture a sub-picosecond reduction in magnetization (demagnetization) resulting from the laser induced heating [70]. After several picoseconds to tens of picoseconds following laser excitation, the energy carriers approach thermal equilibrium, and the energy transfer will then be dominated by thermal transport *via* heat conduction. The temperature decay in the sample system can then be described by heat diffusion, which depends on the thermal conductivity (Λ), volumetric heat capacity (C), and the interfacial conductance (G) of the multi-layers and interfaces within the sample. The discussion of extracting these thermal parameters from TR-MOKE signal has been discussed elsewhere [26,27].

3.1.3 Precessional Magnetization Dynamics

In addition to thermal information, this ultrafast demagnetization from laser pulses also initiates magnetization dynamics governed by the LLG equation, specifically magnetization (spin) precession [71,72]. Further research into this all-optical, pump-probe technique showed that the frequency of magnetic precession extracted from TR-MOKE is consistent with frequency-domain FMR results [24]. The working principle for spin precession measured with TR-MOKE consists generally of three distinct regions, as illustrated in Fig. 3.2 [24,73]. Initially, the magnetization **M** is in equilibrium and is parallel to the effective field, which is the minimum energy direction for the magnetization. Then, the pump beam deposits energy into the magnetic material, heating it up, and inducing thermal demagnetization. Because of the heating, the material's saturation magnetization and magnetic anisotropy both decrease, resulting in a change in $\mathbf{H}_{\text{eff}}$. Next, as the magnetic material cools down, M_s and magnetic anisotropy begin to recover to their initial values,

restoring the minimum energy direction back to the original equilibrium direction. At this point, **M** does not align with $\mathbf{H}_{eff}$, resulting in a torque that acts on **M**. This torque causes damped precessional motion around the equilibrium direction, as described by the LLG equation (Eq. 2.7). After some mathematical manipulation, Eq. 2.8 will provide the theoretical foundation to analyze TR-MOKE measurement data for extracting both the spin precession frequency (f) and damping parameter (α), which is discussed in Chapters 4 and 5 and Appendix B.

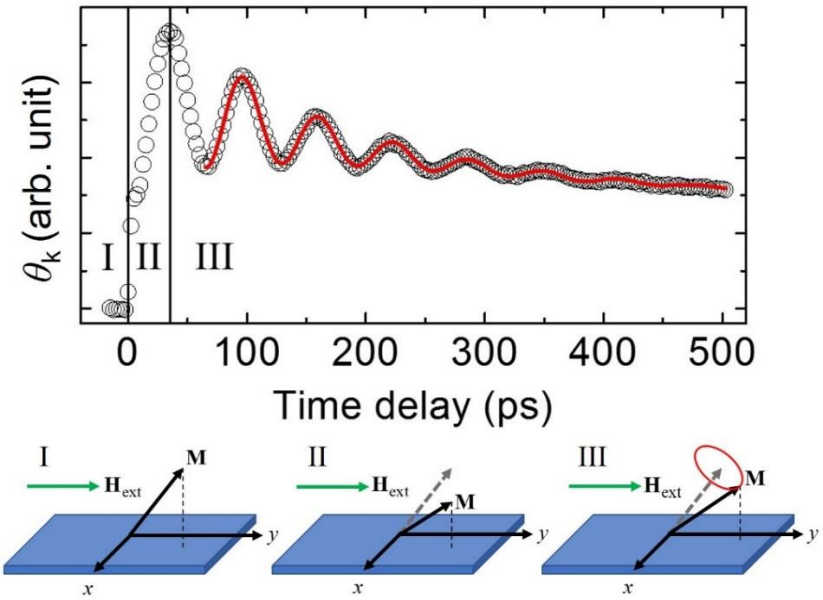

Figure 3.2. The typical signal of magnetic precession from polar TR-MOKE (open symbols). In region I, the system is in equilibrium with the magnetization (**M**) canted by an external field ($\mathbf{H}_{ext}$) to be along $\mathbf{H}_{eff}$. Following the laser pulse heating, both the saturation magnetization and magnetic anisotropy will decrease, which results in a change in the minimum energy direction in region II. After some amount of time, the M_s will recover, but the angle between **M** and $\mathbf{H}_{eff}$ will result in precession (region III). The solid line indicates the fit of the data to a decaying sinusoid with a thermal background. In regions I and III, $\mathbf{H}_{eff}$ is pointing along the equilibrium direction as denoted by the gray dashed line.

3.1.4 Optical Setup of Time-Resolved Magneto-Optical Kerr Effect

The TR-MOKE metrology belongs to the ultrafast pump-probe technique that uses a femtosecond laser to first pump energy into a material, and then to probe the material response. The major difference between the TR-MOKE and the more common time-domain thermoreflectance (TDTR) techniques is the type of signals collected by the probe beam. In TR-

MOKE measurements, the polarization state of the probe beam reflected from the sample is monitored [74]; while in TDTR measurements, the reflectivity from the sample surface is collected. For a small temperature rise, both TR-MOKE and TDTR signals can be treated as linearly proportional to the temperature variation of the sample.

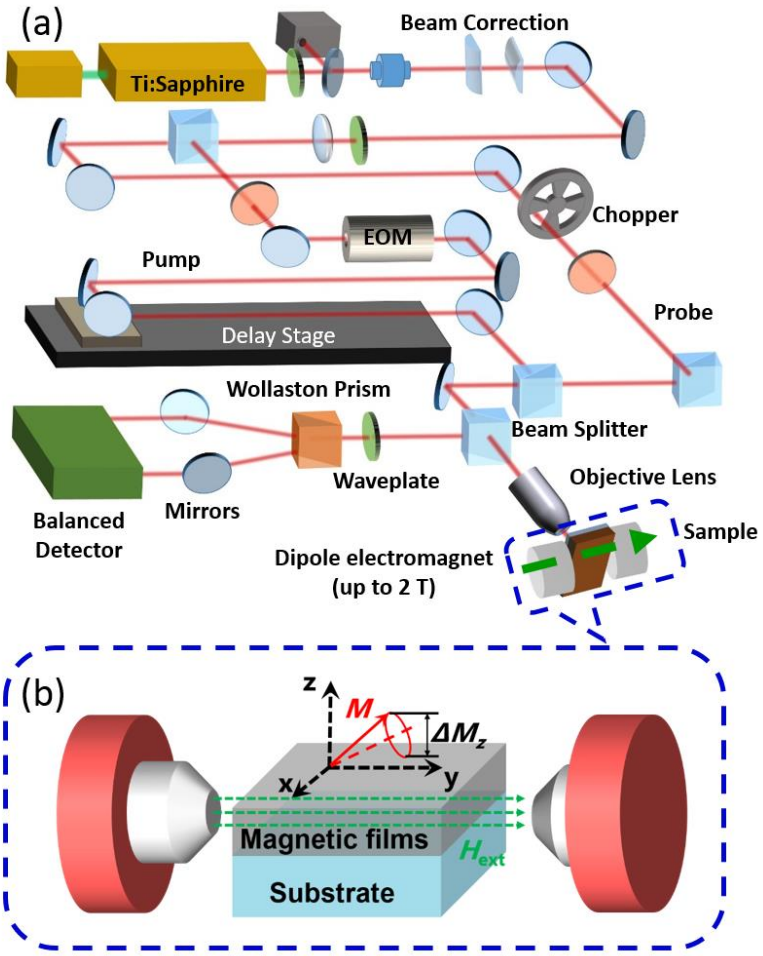

Figure 3.3. (a) Schematic layout of the TR-MOKE experimental setup depicting the major optical components for measuring the magnetization precession. (b) A magnified view of the sample measurement configuration with respect to the external magnetic field (H_{ext}).

Figure 3.3 depicts the optical layout of an example TR-MOKE setup at the University of Minnesota, Twin Cities [73], which is upgraded from the basic two-tint time-domain thermoreflectance setup [75]. In TR-MOKE, a mode-locked Ti:Sapphire laser generates a train of pulses (typically ~ 100 fs in duration) at a repetition rate of 80 MHz (12.5 ns between pulses). An isolator placed right after the laser output prevents the back reflection of light into the laser cavity. The beam shape is corrected by a pair of cylindrical lenses to produce a circular beam spot (preferred for in-plane thermal transport measurements) [76]. A polarizing beam splitter separates the laser into pump and probe beams with orthogonal polarizations. The pump beam is modulated with an electro-optical modulator (EOM) synchronized to a function generator, typically operated at a tunable frequency in the range of 0.1 to 20 MHz. The probe beam is modulated by a mechanical chopper (~200 Hz). The optical path of the pump beam can be adjusted by a delay stage, which produces a time separation of up to 4 ns between pump heating and probe sensing. The diffraction-limited beam spot size ($1/e^2$ radius) at the sample surface ranges from one to a few tens of microns, depending on the magnification of the objective lens. A set of optical filters are exploited to create a spectral separation between pump and probe to suppress pump light that might otherwise leak into the detector. An electromagnet is placed near the sample to provide external magnetic fields (H_{ext}) for the sample.

For the experiments in this thesis, the pump beam has a $1/e^2$ beam diameter of 12 μm (10× objective lens) and is modulated at 9 MHz with the EOM. An electromagnet produced external magnetic fields up to 2 T (it has since been updated to achieve fields up to 3 T). A Hall-probe sensor placed directly behind the sample measures the magnitude of the applied field (H_{ext}). A custom-built rotational stage allows for the control of the applied field direction, as defined by the angle between the sample surface normal and the applied field direction (θ_H). The uncertainty in angular alignment of θ_H is estimated to be approximately ±1°.

To facilitate TR-MOKE measurements, a Wollaston prism in conjunction with a balanced detector (photodiode) is used to capture the Kerr rotation angle of the probe beam reflected from the sample. Caution should be exercised to carefully balance the photodiode prior to conducting a measurement, to suppress non-MOKE signals. Additional steps such as differential measurements can also be taken to reduce the non-MOKE components received by an imperfectly balanced detector [26,27]. The output signal from the balanced detector is sent to a radio-frequency (RF) lock-in amplifier and then to a computer for signal processing with a digital audio-frequency (AF) lock-in. This double-modulation and double lock-in technique allows for the detection of low-level Kerr rotation signals.

3.2 TDTR Measurement of Acoustic Strain Waves

Measurements of TDTR for the purpose of extracting thermal transport properties is one of the main research directions of the MNTTL at the University of Minnesota. Since the beginning of the lab, it has produced a large amount of quality publications using the TDTR method to measure thermal properties [73,77-84]. Because my primary research was a new field within the lab, I did not make use of this technique for thermal applications. Instead, I utilized this technique for understanding ultrafast strains, or picosecond acoustics [85-88]. While a more in-depth explanation is available in many of these papers, I will try to briefly discuss how this mechanism allows us to understand material properties such as the speed of sound or the film thickness of thin films.

The temperature rise due to the pump laser pulse leads to thermal expansion and thus creates a strain. The resulting strain wave normal mode acts through the film stack and leads to a strain wavelength equal to twice the thickness of the film (or a half wavelength corresponding to the film thickness).

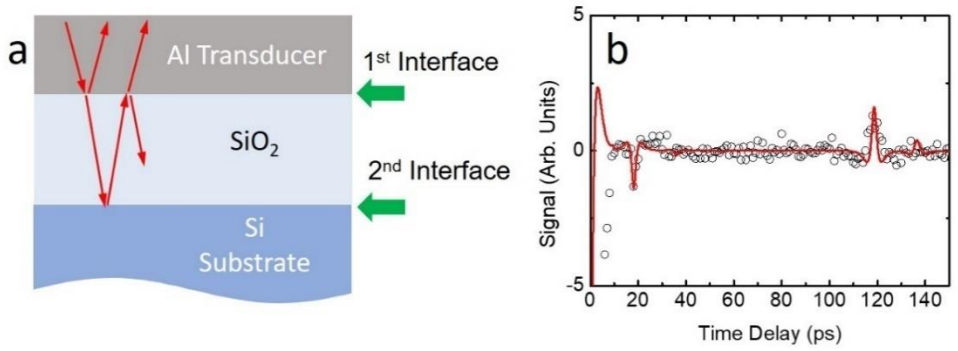

Figure 3.4. An illustration of the picosecond acoustics in ultrafast measurements. (a) The path of the acoustic waves in a reference sample of Al (53 nm)/SiO_2 (300 nm)/Si (substrate). The acoustic waves reflect at the interfaces and will create an optical signal when they return to the top interface. (b) TDTR data (open symbols) with the background subtracted showing the acoustic signal and simulation results (solid line) [85,89].

To understand the resulting optical signal, we typically estimate the time response by considering a strain impulse on the top surface at initial heating and use the echo time to determine either the speed of sound (with a known thickness) or the thickness (with a known speed of sound). An illustration of the strain propagation in a multilayer system is shown in Fig. 3.4a. From raw TDTR data on a reference sample (Fig. 3.4b) it can be seen that there will be sudden peaks and valleys in the reflectivity of materials that correspond to the round-trip acoustic echo from this material. With the help of code developed by Maris et al. or some back of the end of the envelope calculations, the thickness of the transducer layer in this sample can be determined. Whether the signal is a peak or a valley depends on the acoustic impedance ($Z = \rho v$ where ρ is the density and v is the speed of sound) of the materials in the stack [86,89].

For some magnetic materials, there is a connection between the magnetization in the material and an internal strain. These “magnetoelastic” effects will cause a strain when the magnetization is moved or a field is applied (magnetostriction), or the inverse effect, where a change in magnetization is caused by an applied strain (inverse magnetostriction, or the Villari effect). Because of the ultrafast laser heating in TDTR and TR-MOKE measurements, the impact of the picosecond acoustics in materials with large magnetoelastic effects should be apparent in the

magnetization. To capture this, I needed to use both TDTR (to capture pure acoustics) and TR-MOKE (to capture magnetization) to confirm the effect. These measurements are discussed in greater detail in Chapter 6.

3.3 Vibrating Sample Magnetometry

Both of the measurements discussed in the previous sections have focused on ultrafast measurements to determine material properties, but it also to understand the response of the material at longer time scales. Vibrating Sample Magnetometry (VSM) allows for measurements of the "static" response of magnetization along a specific direction within an external field or temperature.

The working mechanism of VSM measurements is that a changing magnetic flux induces an electrical voltage (Faraday's Law of Induction). For ferromagnetic samples, the aligned magnetization of the material will lead to a stray magnetic field originating from the sample. In stasis, this stray field does not cause any electrical response, but by quickly oscillating the sample within a "search coil", the magnetic flux from this stray field is varying in time and thus creating an electrical response. Because the induced voltage amplitude depends on the strength of the stray field (which in turn is related to the strength of the magnetic moment), the magnetization in a given environment is able to be measured. In this way, by physically vibrating the sample and recording the oscillating electrical response, the magnetic moment in various fields and temperature can be measured.

For the VSM measurements in this thesis, a Physical Property Measurement System (PPMS) from Quantum Design with a VSM attachment was used. This system uses a superconducting magnetic to achieve external magnetic fields of up to 9 Tesla and a sample temperature of up to 1000 K. With the assistance of a lock-in amplification system, the PPMS is able to measure the magnetic moments of even thin films on the order of nanometers thick.

3.3.1 Magnetic Hysteresis Curves (M-H Loops)

For the purposes of describing a magnetic material's ability to maintain the magnetization along a specific direction, the effective anisotropy field $H_{k,eff}$ is typically used. In this section, I will discuss why this property is important and how it can be determined from VSM measurements.

Nearly 50 years ago, Stoner and Wohlfarth created a model that describes the static magnetization state of a single magnetic domain in the presence of an external field [28]. They introduced the concept of energy minimization to determine the direction of an external field (i.e., take the derivative of the energy with respect to the direction of magnetization and minimize). This allows us to predict the direction of magnetization in a given instance, and, more importantly for our purposes, allows us to describe an energy surface that also determines the dynamics. Building on Eq. 2.4, the energy can be described in terms of important vectors of a material with perpendicular magnetic anisotropy (K_u):

$$F = F_0 + F_Z + F_K + F_D = F_0 - \mathbf{M}\cdot\mathbf{H}_{ext} - K_u\left(\mathbf{m}\cdot\hat{z}\right)^2 + 2\pi\left(\mathbf{M}\cdot\hat{z}\right)^2 \qquad 3.3$$

where F_0 is an offset, F_Z is the Zeeman energy, F_K is the anisotropy energy, and F_D is the demagnetization energy. There are already a few assumptions made in this equation: 1) the magnetic properties are uniform and don't vary in space; 2) there is only uniaxial anisotropy in the system; 3) this is assumed to be approximated by an infinite flat plate where the *z*-axis is the out-of-plane direction; and 4) the amplitude of **M** is a constant value of M_s, only the direction changes. Eq. 3.3 can be simplified further by defining everything with its angle from the *z*-axis.

$$F = F_0 - M_s H_{ext}\cos\left(\theta - \theta_H\right) - \left[K_u - 2\pi M_s^2\right]\cos^2\left(\theta\right). \qquad 3.4$$

Minimizing Eq. 3.4 will provide the direction of magnetization (θ) that is the equilibrium state of the magnetic system even with an external field at applied at some angle from the *z*-axis (θ_H).

In order to show the difference between two directions (and thus illustrate anisotropy), it is common to measure the magnetization in two orthogonal directions. The typically chosen directions are out-of-plane ($\theta_H = 0$ and M/M_s along the z-axis is measured) and in-plane ($\theta_H = \pi/2$ and M/M_s along the x-axis or y-axis is measured). The resulting measurement is called a M-H loop or magnetic hysteresis loop and will look like Fig. 3.5.

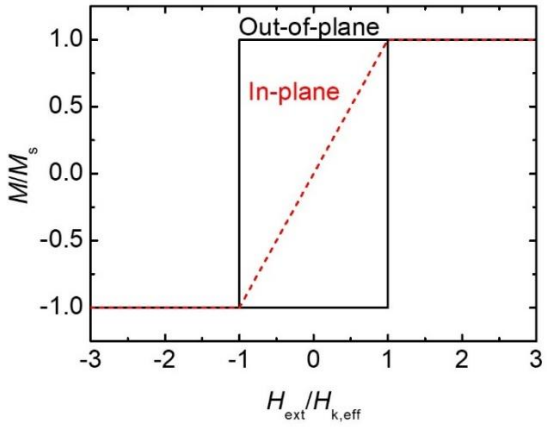

Figure 3.5. An example M-H or magnetic hysteresis plot that shows the fraction of magnetization along either the in-plane (red) or out-of-plane (black) direction for a given external field (H_{ext}) along that direction for a single-domain sample with perpendicular magnetic anisotropy.

From Fig. 3.5, it is clear why these figures are called hysteresis loops from the out-of-plane result. When $H_{ext} < H_{k,eff}$, there are two local energy minima (and in fact where $H_{ext} = 0$, the local minima are of equal energy), but the magnetization will only exist in one minima. Upon increasing the field, this remains true until $H_{ext} > H_{k,eff}$ when the energy barrier between the two local minima disappears and they merge into one global minimum. Further analysis of the out-of-plane results show that the magnetization is "saturated" ($M/M_s = 1$) when no external field is applied. This is typically referred to as an "easy axis" because it is easy to magnetize the sample along this direction. Conversely, none of the magnetization is in-plane in this state and it requires at least $H_{ext} = H_{k,eff}$ for the magnetization to saturate along the in-plane direction, so it is called the "hard axis".

Due to the complex and multi-domain nature of real samples, an example of these box-like and linear behaviors shown in Fig. 3.5 are rare. Instead, the amount of field it takes to change the direction of magnetization in the out-of-plane direction is called the coercivity (H_c) and is always less than $H_{k,eff}$. This means that out-of-plane measurements are typically not useful for determining $H_{k,eff}$ and instead, the in-plane measurement is used to determine $H_{k,eff}$ by determining what field the magnetization saturates in that direction.

3.3.2 Temperature Dependent Magnetization (Curie Temperature)

As discussed briefly in section 3.1, TR-MOKE measurements excite the magnetization by heating up the magnetic system. Recently, this heating process has become more important to the research that will continue to be conducted in the MNTTL. Whereas the standard hysteresis measurements are done in a constant temperature and a changing field, these measurements are done by applying a constant field and a changing temperature. The measurement process is the same as standard VSM, but the holders are specialized due to the high temperatures achieved during the measurement.

The decrease of magnetic moment in ferromagnetic materials was originally described by Pierre Curie. He found that by heating up a magnetic material the magnetism would go from ordered to disordered before disappearing at a temperature that depended on the material. This "Curie Temperature" (T_C) is now crucial for applications like HAMR. Above this temperature, the thermal fluctuations overcome the ferromagnetic order and the materials become paramagnetic. Since then, there have been multiple theories that attempt to describe the thermal demagnetization in different temperature regions below this critical temperature. In the low temperature limit, the existence of magnons leads to Bloch's "$T^{3/2}$" Law [90]. In the intermediate temperature regime, the mean field theory is used in conjunction with the Brillouin function in Eq. 3.5 (or Langevin function in the limit of large j shown by Eq. 3.6, which is the assumed form for this thesis) [90].

$$B_j(x) = \frac{2j+1}{2j}\coth\left(\frac{2j+1}{2j}x\right) - \frac{1}{2j}\coth\left(\frac{x}{2j}\right), \quad 3.5$$

$$L(x) = \coth(x) - \frac{1}{x}. \quad 3.6$$

The magnetization as a function of temperature can then be found by the transcendental equation that utilizes the Boltzmann constant (k_B) and the atomic moment (μ).

$$m(T) = \frac{M_s(T)}{M_s|_{T=0}} = L\left(\frac{3mk_BT_C + \mu H_{eff}}{k_BT}\right). \quad 3.6$$

These two models provide some estimation of magnetic properties in specific regions, but they vary greatly over the entire temperature region (as shown in Fig. 3.6). There are a variety of other methods to predict this temperature dependence that take into account atomic structure and thermal fluctuations (such as Monte Carlo based methods using the Ising model [91]). While it may be useful to apply these theories to provide a physical background to a magnetic measurement, it is often useful to measure the real spontaneous magnetization as a function of temperature to truly understand the temperature dependence. In this thesis, I will make use of the mean field theory to understand temperature dependence, but future works should use fittings of real measurements as inputs into understanding TR-MOKE signal.

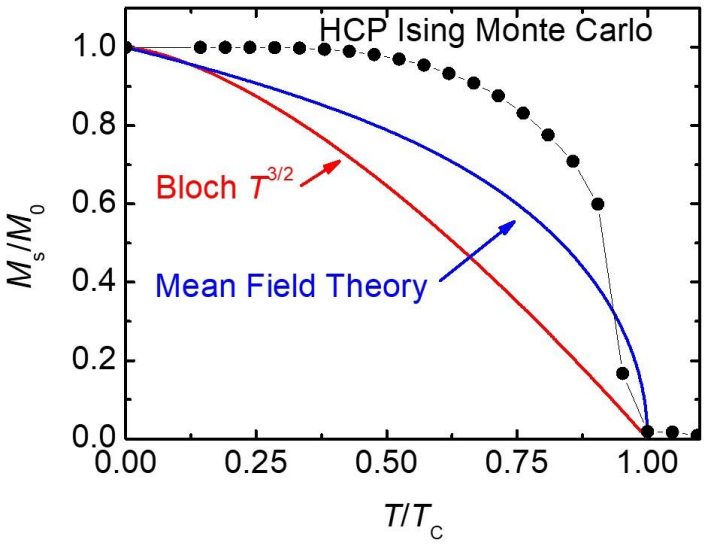

Figure 3.6. A plot of the spontaneous magnetization (normalized to the magnetization at 0 K, M_0) as a function of temperature (normalized to T_C). Three different simulated models are depicted: an Ising Model using Monte Carlo simulation methods of a hexagonally close-packed system, the Bloch $T^{3/2}$ law, and the mean field theory. Each of these models has a useful region, but none accurately describe the temperature over the entire temperature range.

CHAPTER 4: ANGULAR DEPENDENCE OF EXTERNAL FIELD FOR TR-MOKE MEASUREMENTS OF MAGNETIZATION DYNAMICS

This chapter is a discussion of the optimizing the TR-MOKE signal for magnetic measurements. Samples were made by Delin Zhang (postdoc in Prof. Jian-Ping Wang's group) and the development of the background theory was developed with the help of Prof. Crowell. All simulations, measurements, and figures were conducted by me.

- Reproduced from [Lattery, D. M., Zhu, J., Zhang, D., Wang, J.-P., Crowell, P. A., and Wang, X.J., "Quantitative analysis and optimization of magnetization precession initiated by ultrafast optical pulses", *Appl. Phys. Lett*. **113**, p. 162405 (2018).], with the permission of AIP Publishing.

Spintronic devices consisting of materials with large PMA are promising for the advancement of computer memory, data storage, and spintronics. Due to the time scale of magnetic switching in these devices (~ 1 ns) [17,92,93], it is crucial to understand magnetization dynamics at such short time scales. To understand magnetization dynamics requires knowledge of the magnetic anisotropy and the Gilbert damping (α), as defined in the LLG equation (Eq. 2.7). While anisotropy can be determined through magnetostatic measurements (such as VSM), extracting α requires measurements that can capture the dynamic magnetization at time scales faster than magnetic switching. To date, the most common method to determine α is frequency-domain measurements of FMR [32,94]. By measuring the resonance frequency and linewidth as a function of applied field, FMR probes both the magnetic anisotropy and Gilbert damping [20,56,95-97]. As spintronic applications favor materials with large PMA, the all-optical TR-MOKE has become relied on more. TR-MOKE is essentially a time-domain FMR technique that can be readily integrated with large external fields to capture high resonance frequencies using optical excitation. Technically, TR-MOKE is limited only by the sampling frequency (~1 THz) and available external fields. This technique allows materials with large PMA ($>10^6$ erg/cm^3) to be measured [45,48,98,99].

There are a number of studies reporting TR-MOKE measurements of the Gilbert damping in PMA thin films (e.g., films with large magnetocrystalline anisotropy such as $L1_0$ FePd, or films

with interfacial anisotropy including CoFeB) [45,48,100-102]. While these studies utilized similar polar MOKE measurement techniques, there exists large variations in the choice of both the amplitude range and the angle (θ_H with respect to the sample surface normal *z*, see Fig. 4.1) of the external field (H_{ext}). For example, some literature studies utilized in-plane external fields because of its well-understood frequency dependence [103], while others applied H_{ext} at a chosen angle away from the in-plane in order to reduce the impact of inhomogeneous broadening likely caused by a distribution of magnetic anisotropy throughout the sample [104]. Additionally, it has been experimentally observed that the process of applying H_{ext} at some angle between 0 and 90° from the surface normal is beneficial to increase the TR-MOKE signal amplitude [102,103]. Nevertheless, a systematic study that explores the angular dependence of the TR-MOKE measurement signal is still lacking. In this chapter, I will first address this issue by discussing the mechanisms behind the θ_H dependence of the TR-MOKE signal and then predicting the optimal angle of θ_H for conducting TR-MOKE measurements with the improved signal-to-noise (SNR) ratio. The theoretically predicted optimal TR-MOKE operational conditions are further validated by direct experimental studies of a representative sample consisting of a tungsten-seeded CoFeB thin film with large PMA.

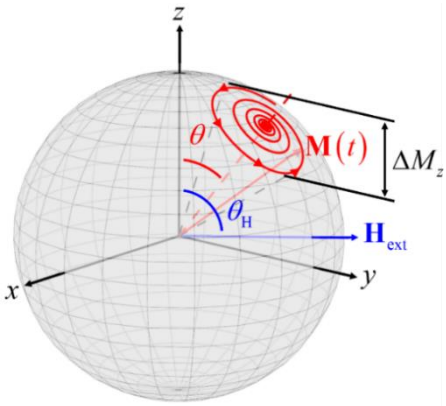

Figure 4.1. A three-dimensional representation of the magnetization vector (**M**) precessing around the equilibrium direction (θ) displayed on the surface of a sphere of radius M_s. The equilibrium direction is controlled by the magnitude and direction (θ_H) of the external magnetic field vector ($\mathbf{H}_{ext}$). The change in the *z*-component of magnetization (ΔM_z) is proportional to the TR-MOKE signal.

4.1 Macrospin Simulations with the Landau-Lifshitz-Gilbert Equation

As discussed briefly in Chapter 2, simulations in this work utilize a finite difference approach to solve the LLG equation (Eq. 2.7 and reproduced here as Eq. 4.1) with an explicit solution for the magnetization vector (**M**) as a function of time, following a forward Euler method:

$$\frac{d\mathbf{M}}{dt} = -\gamma\left(\mathbf{M}\times\mathbf{H}_{\text{eff}}\right) + \frac{\alpha}{M_{\text{s}}}\left(\mathbf{M}\times\frac{d\mathbf{M}}{dt}\right), \qquad 0.1$$

where **M** is the magnetization vector with a magnitude of M_s (the saturation magnetization), γ is the gyromagnetic ratio, $\mathbf{H}_{\text{eff}}$ is the effective magnetic field, and α is the Gilbert damping parameter. The vector $\mathbf{H}_{\text{eff}}$ is determined by taking the gradient of the magnetic free energy density (F) with respect to the magnetization direction ($\mathbf{H}_{\text{eff}} = -\nabla_{\mathbf{M}} F$). The scalar quantity F is the summation of contributions from the Zeeman energy (resulting from the external magnetic field, $\mathbf{H}_{\text{ext}}$), perpendicular uniaxial magnetic anisotropy (K_u), and the demagnetizing field.

While Eq. 4.1 is often used to describe magneto-dynamics, it is not conducive to numerical solutions of this ordinary differential equation. To simplify the development procedures of computational algorithms, it is preferable to utilize the Landau-Lifshitz equation (Eq. 2.8 and reproduced here as Eq. 4.2) [105]:

$$\frac{d\mathbf{M}}{dt} = -\frac{\gamma}{1+\alpha^2}\left[\left(\mathbf{M}\times\mathbf{H}_{\text{eff}}\right) + \frac{\alpha}{M_{\text{s}}}\left(\mathbf{M}\times\left(\mathbf{M}\times\mathbf{H}_{\text{eff}}\right)\right)\right]. \qquad 0.2$$

In equilibrium, **M** is parallel to $\mathbf{H}_{\text{eff}}$, and thus the magnetization does not precess. Once the magnetization is slightly tilted away from the equilibrium direction (θ), it will begin to precess around the equilibrium direction, and finally damp towards equilibrium at a rate determined by the magnitude of α (shown in Fig. 4.1). For the purposes of this work, we use the macrospin approximation, in which all of the parameters in Eq. 4.1 are independent of position. This means that the explicit dependence of any parameters on position (inhomogeneous broadening) and

coupling of excitations at different wave-vectors (two-magnon scattering) are ignored. This approximation is justified at high frequencies, at which α is considered to be an intrinsic parameter.

We emphasize that in interpreting our experiments, we assume that the Gilbert damping constant α is independent of the orientation of the applied field, and hence the magnetization. This assumption ignores contributions from two-magnon scattering and inhomogeneous broadening (discussed more in sections 2.3.2 and 2.3.5 respectively). In principle, both contributions can be made small relative to the intrinsic Gilbert damping by going to sufficiently high applied field. Just as important, the two-magnon contribution at high fields depends only weakly on angle for field orientations that are nearly in plane [106]. For this reason, we expect the observations of this paper to apply even in samples with significant two-magnon scattering.

For TR-MOKE measurements, a "pump" laser pulse increases the temperature at an ultrafast time scale (~400 fs determined from the pump pulse duration), which causes a thermal demagnetization (a decrease in M_s resulting from the increase of temperature) [24,73]. This thermal demagnetization temporarily shifts the equilibrium direction initiating magnetization precession, which is continued even when M_s has recovered to its original state. Here, the demagnetization process is treated as a step decrease in M_s that lasts for 2.5 ps before an instant recovery to its initial value. All signal analysis discussed in this work follows the recovery of M_s.

For polar MOKE measurements, the Kerr rotation is proportional to the projected magnetization in the *z*-direction (M_z, the through-plane magnetization) [62]. The evolution of M_z in time during precession will appear as a decaying sinusoid as captured by TR-MOKE measurements, i.e., $M_z(t) \propto \sin(2\pi ft + \varphi)\exp(-t/\tau)$ with f, φ, and τ being the angular resonance frequency, the phase term, and the relaxation time of spin precession, respectively. The amplitude of the precession will greatly depend on the magnitude and angle of the external applied field, which is directly related to the SNR of TR-MOKE signals.

By analyzing the precession as a function of the field (H_{ext}) and angle (θ_H), the precession amplitude (ΔM_z) can be extracted. Figure 4.2a shows the predicted ΔM_z as a function of the time delay between pump excitation and probe sensing, which can be treated as a direct simulation of TR-MOKE signals. Figure 4.2b depicts the θ_H-dependent ΔM_z normalized to the maximum ΔM_z for $\theta_H = 90°$ for two representative regions of magnetic field, $H_{ext} > H_{k,eff}$ and $H_{ext} < H_{k,eff}$. Here $H_{k,eff}$ denotes the effective anisotropy field of the sample that is related to K_u through $H_{k,eff} = 2K_u/M_s - 4\pi M_s$ and can be readily determined from VSM measurements. Tracking this signal amplitude as a function of θ_H, reveals that the precession (and thus the signal) will be maximized for a certain θ_H as shown in Fig. 4.2b. Maximizing the oscillation implies that it will be beneficial to maximize the "magnetic torque" term ($\mathbf{M} \times \mathbf{H}_{eff}$, which prefers a large angle between M and H_{eff}), but it is also important to include that TR-MOKE measures the projection of the magnetization along the z-direction (which prefers $\theta = 90°$). Consequently, the value of $\theta_{H,MAX}$ requires weighing inputs from both the magnetic torque and the z-direction projection of magnetization.

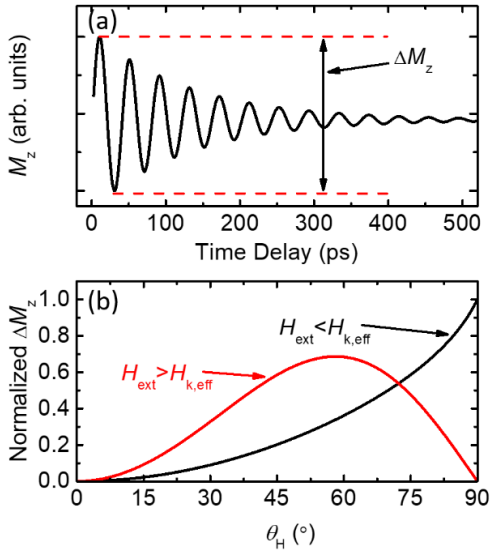

Figure 4.2. (a) The time-dependent magnetization vector predicted by the LLG simulation (Eq. 4.2) for specific conditions, which represents the TR-MOKE signal from measurements (with thermal background removed). The difference between the maximum and minimum of the z-component of magnetization in time (ΔM_z) provides information about the strength of the TR-MOKE signal. (b) Normalized ΔM_z as a function of θ_H for two cases of $H_{k,eff} < H_{ext}$ (black) and $H_{k,eff} > H_{ext}$ (red). Both plots are normalized to the maximum z-component of magnetization of the $H_{k,eff} < H_{ext}$ case.

Depending on the field ratio ($H_{ext}/H_{k,eff}$), the angular dependence of magnitude will drastically change. For $H_{ext}<H_{k,eff}$, the magnetization will be in equilibrium between the perpendicular direction and the in-plane direction ($0 \leq \theta \leq 90°$). Maximizing the magnetic torque and projection in the z-direction in these cases will cause H_{ext} applied in-plane ($\theta_H = 90°$) to be the optimal setup [shown by the black line in Fig. 4.2b]. Once H_{ext} exceeds $H_{k,eff}$, the Stoner-Wohlfarth minimum energy model predicts that the magnetization will approach the direction of external field, but never perfectly align with H_{ext} (except for the extreme cases of $\theta_H = 0$ or 90°) [29]. When $\theta_H = 0°$ or 90°, these two directions will excite no magnetic torque and therefore no magnetic precession will occur, as indicated by the amplitude minima at these extreme cases. For the intermediate range of θ_H in between 0 and 90°, the two effects for optimizing signal (maximizing torque and maximizing projection) will compete, leading to an amplitude maximum at an angle that depends on the field ratio of $H_{ext}/H_{k,eff}$. The dependence of the M_z amplitude on θ_H can be readily obtained by dividing ΔM_z in Fig. 4.2 by sin θ with θ being the equilibrium angle.

Figure 4.3 shows a contour plot of the dependence of the normalized ΔM_z representing the spin precession amplitude as a function of both H_{ext} and θ_H. The highest amplitude of precession will occur near $H_{k,eff}$ when the field is applied in the film plane. If the external field is greater than $H_{k,eff}$, it is beneficial to conduct the measurement at an angle that is out of the film plane. To better illustrate this trend, the dotted red line in Fig. 4.3 indicates the angle of maximum signal ($\theta_{H,MAX}$) at specified field ratios. Based on these results, measurement conditions can be optimized to maximize the precession signal based on the field ratio. For example, if the maximum strength of the magnetic field is $2H_{k,eff}$, then it would be beneficial to set $\theta_H > 70°$. Furthermore, measurements conducted at a constant H_{ext} but with varying magnetic field angles should not necessarily choose the highest possible H_{ext} to achieve the optimal SNR.

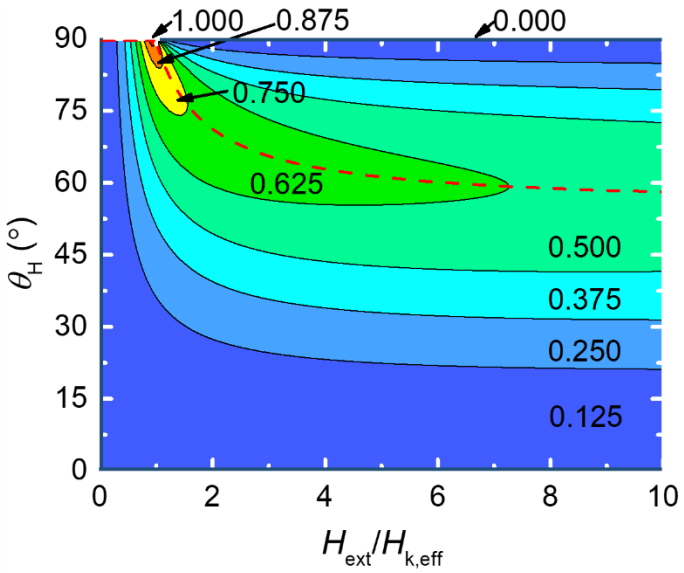

Figure 4.3. A contour plot of the normalized ΔM_z signal as a function of the field ratio ($H_{ext}/H_{k,eff}$) and θ_H where a value of "1" indicates the maximum possible signal. The dotted red line corresponds to $\theta_{H,MAX}$ where the signal is maximized for a specific field ratio.

To further assist in the design of TR-MOKE measurements with optimal SNR, we note that there is a simple means to estimate the amplitude of the TR-MOKE signal based on the ansatz that the magnetization during the pulse is modified by an amount ΔM_s, so that the effective field during the pulse is:

$$\mathbf{H}_{\text{eff}}^{'} = \mathbf{H}_{\text{eff}} + 4\pi\Delta M_s \cos(\theta)\hat{z}, \tag{0.3}$$

which accounts for the demagnetizing field due to the non-equilibrium magnetization. We make the simplifying assumption that this field is constant during the pulse and that $\Delta M_s \propto M_s$, so that the angular displacement of the magnetization during the pulse is proportional to the torque:

$$\gamma\mathbf{M} \times \mathbf{H}_{\text{eff}}^{'} = \gamma M_s 4\pi\Delta M_s \cos(\theta)\sin(\theta)\hat{\varphi}, \tag{0.4}$$

where $\hat{\varphi}$ is a unit vector in the *x*-*y* plane of Fig. 1. After the pulse, the magnetization precesses about the equilibrium effective field on the trajectory shown in Fig. 4.1, and the amplitude $|\Delta M_z|$ of the modulation of the z-component of the magnetization is then proportional to sin θ, so that

$$|\Delta M_z| \propto M_s \cos(\theta)\sin^2(\theta). \quad 0.5$$

We recall that θ is the angle of the equilibrium effective field relative to the z-axis in Fig. 1. It is possible to express θ in terms of the angle θ_H minimizing the free energy:

$$F = -M_s H_{ext} \cos(\theta_H - \theta) - \frac{1}{2} M_s H_{k,eff} \cos^2(\theta), \quad 0.6$$

with respect to θ, yielding the compact expression:

$$\theta_k \propto \frac{\Delta M_z}{M_s} \propto \sin(\theta - \theta_H)\sin(\theta), \quad 0.7$$

for the amplitude θ_k of the TR-MOKE signal. It is then easy to calculate the angle $\theta_{H,MAX}$ at which θ_k is maximized for each value of H_{ext}. This defines the contour shown as the dashed red line in Fig. 4.3. The result is shown in Fig. 4.4, in which a comparison is made to the full simulation.

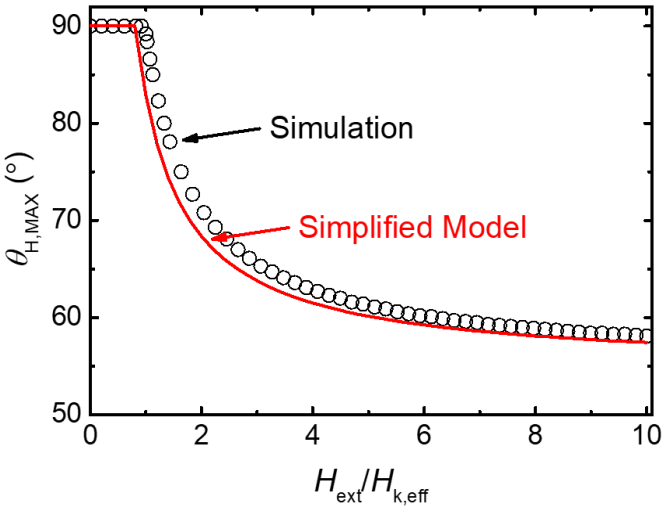

Figure 4.4. The trend of $\theta_{H,MAX}$ as a function of the field ratio. The open circles indicate results from the LLG simulation discussed previously, while the red curve is the simplified model from Eq. 4.7.

4.2 Experimental Validation of Macrospin Simulation Amplitude

To verify the model prediction for the maximum TR-MOKE signal amplitude, we conducted a series of TR-MOKE measurements on a W/CoFeB/MgO thin-film sample with PMA. The CoFeB sample was post-annealed at 300 °C and has an $H_{k,eff}$ of 6.1 kOe as determined from VSM measurements. A schematic of the sample stack is shown as an inset of Fig. 4.5c. More detailed information regarding the sample preparation, and structural and magnetic property characterization can be found in Chapter 5. During measurements, we considered four different amplitudes of H_{ext} (4, 6, 8, and 10 kOe) to show the θ_H dependence of TR-MOKE signals covering both the low- and high-field ratio regimes. To avoid blocking the laser with the magnetic poles, the range of θ_H was confined from 80° to 90° with a 2° interval.

For ease of comparison, we subtracted the thermal background from the raw TR-MOKE measurement data to obtain the pure precession signal, which oscillates sinusoidally at a decaying rate related to the Gilbert damping. As shown in Fig. 4.5a, this involves fitting the data to the equation $\theta_k(t) = A + B\exp(-t/C) + D\sin(2\pi ft + \varphi)\exp(-t/\tau)$ and subtracting the thermal background, as denoted by the decaying exponential $A + B\exp(-t/C)$. The amplitude is then calculated using the same method as shown in Fig. 4.2a. Figures 4.5b-e summarize the comparison of the normalized oscillation amplitudes from both measurements (red symbols) and model prediction (black lines) for all four values of H_{ext}. The data and theoretical curves are normalized to the highest amplitude for a given H_{ext}.

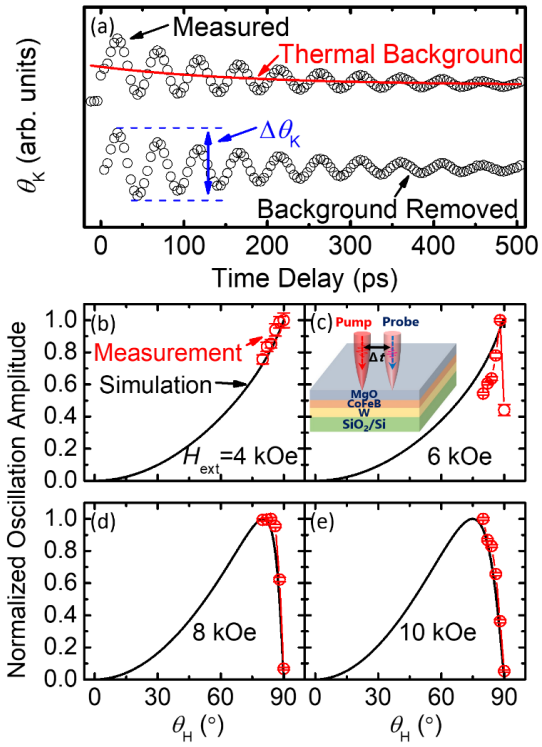

Figure 4.5. (a) TR-MOKE signal (θ_H = 80° and H_{ext} = 10 kOe) containing both the precessional signal and a thermal background. With the removal of thermal background, the oscillation amplitude can then be calculated. (b - e) Normalized TR-MOKE oscillation amplitudes for a representative PMA thin-film sample of W/CoFeB/MgO at external fields of 4, 6, 8, and 10 kOe. The open red circles show the measurement data (a line between points is provided to guide the eye) while the black curves indicate the results from the LLG simulations for a material with $H_{k,eff}$ = 6.1 kOe.

Comparisons between the trends of predicted simulations and measurement results show excellent agreement. As expected, the signal amplitude increases monotonically with increasing angle for $H_{ext} < H_{k,eff}$ and has an angle of maximum signal for $H_{ext} > H_{k,eff}$. These measurements can even capture the predicted peak of amplitude at nearly the same θ_H for fields near $H_{k,eff}$. For the 6 kOe measurements, there is a slight deviation in the amount of decay in signal strength for decreasing θ_H (simulations predict a slower decrease). This is most likely due to the inhomogeneity resulting from a nonuniform distribution of the values of $H_{k,eff}$ in the sample, which leads to a deviation from theory near $H_{k,eff}$. While the θ_H in the setup used in this experiment was limited, these results verify the excellent agreement between simulation and measurement.

4.3 Conclusion

In conclusion, we have developed a numerical approach to simulate the dynamic response of magnetization to a thermally-induced demagnetization process. This approach identifies the optimal angle of external field for the maximum magnetization precession signal in TR-MOKE measurements by balancing the projection of the dynamic magnetization and the magnetic torque. To verify the theoretical prediction, we have conducted TR-MOKE measurements on a W/CoFeB/MgO sample with perpendicular magnetic anisotropy for multiple external fields and field angles. The measurement results demonstrate that the dependence of the TR-MOKE signal magnitude on the external field can be well captured by the theoretical prediction. Our study provides a better understanding on how the external field influence the magnetization precession signals obtained in TR-MOKE measurements, and thus facilitates the design and optimization of measurement conditions for maximizing SNR and improving accuracy.

CHAPTER 5: PERPENDICULARLY MAGNETIZED W-SEEDED COBALT-IRON-BORON THIN FILMS

This chapter is a discussion of the annealing temperature dependence of W/CoFeB/MgO film stacks. Sample fabrication and hysteresis loops were completed by Delin Zhang (co-first author, postdoc in Prof. Jian-Ping Wang's group) and x-ray measurements were completed by Xudong Hang (PhD student in Prof. Jian-Ping Wang's group). I completed the data analysis to extract the anisotropy, dead layer, and intrinsic saturation magnetization ($M_{s,0}$), as well as all TR-MOKE measurements and analysis. This chapter has been adapted from previously published work:

- Lattery, D. M., Zhang, D., Zhu, J., Hang, X., Wang, J.-P., and Wang, X.J., "Low Gilbert Damping Constant in Perpendicularly Magnetized W/CoFeB/MgO Films with High Thermal Stability", *Sci. Rep*. **8**, p. 13395 (2018).

Since the first demonstration of perpendicular magnetic tunnel junctions with PMA Ta/CoFeB/MgO stacks [107], interfacial PMA materials have been extensively studied as promising candidates for ultra-high-density and low-power consumption spintronic devices, including STT-MRAM [108,109], electrical-field induced magnetization switching [110-112], and spin-orbit torque devices [8,113,114]. An interfacial PMA stack typically consists of a thin ferromagnetic layer (e.g., CoFeB) sandwiched between a heavy metal layer (e.g., Ta) and an oxide layer (e.g., MgO). The heavy metal layer interface with the ferromagnetic layer is responsible for the spin Hall effect, which is favorable for SOT and skyrmion devices [115,116]. The critical switching current (J_{c0}) should be minimized to decrease the power consumption of perpendicular STT-MRAM and SOT devices. Reducing J_{c0} requires the exploration of new materials with low Gilbert damping constant (α) and large spin Hall angle (θ_{SHE}). Meanwhile, a large effective anisotropy (K_{eff}) is also favorable to maintain thermal stability [117,118].

In addition, spintronic devices need to sustain operation reliability for processing temperatures as high as 400 °C for their integration with existing CMOS fabrication technologies, providing the standard back-end-of-line process compatibility [119]. Based on this requirement, the magnetic properties of a PMA material should be thermally stable at annealing temperatures (T_{ann}) up to

400 °C. Unfortunately, Ta/CoFeB/MgO PMA films commonly used in spintronic devices cannot survive with T_{ann} higher than 350 °C, due to Ta diffusion or CoFeB oxidation at the interfaces [120-122]. The diffusion of Ta atoms can act as scattering sites to increase the spin-flip probability [38] and lead to a higher Gilbert Damping constant (α), a measure of the energy dissipation [123].

Modifying the composition of thin-film stacks can prevent heavy metal diffusion, which is beneficial to both lowering α and improving thermal stability [124]. Along this line, new interfacial PMA stacks have been developed, such as Mo/CoFeB/MgO, to circumvent the limitation on device processing temperatures. While Mo/CoFeB/MgO films can indeed exhibit PMA at temperatures higher than 400 °C, they cannot be used for SOT devices due to the weak spin Hall effect of the Mo layer [125,126]. Recently, W/CoFeB/MgO PMA thin films have been proposed because of their PMA property at high post-annealing temperature [127], and the large (negative) spin Hall angle of the W layer ($\theta_{SHE} \approx$ -0.30) [128], which is twice that of a Ta layer ($\theta_{SHE} \approx$ -0.12 ~ -0.15) [8,129]. While there have been a few scattered studies demonstrating the promise of fabricating SOT devices using the W/CoFeB/MgO stacks, special attention has been given to their PMA properties and functionalities as SOT devices [130,131], or the damping of in-plane W/CoFeB stacks [132]. A systematic investigation is lacking on the effect of T_{ann} on α of W/CoFeB/MgO PMA thin films with perpendicular anisotropy, as well as the physical mechanisms that alter α after post-annealing.

5.1 Sample Preparation and Magnetic Characterization

In this work, we grow a series of W(7)/$Co_{20}Fe_{60}B_{20}$(1.2)/MgO(2)/Ta(3) thin films on Si/SiO_2(300) substrates (thickness in nanometers) with a magnetron sputtering system (vacuum <5×10^{-8} Torr). These films are post-annealed at varying temperatures (T_{ann} = 250 - 350 °C for 1 hour, 400 °C for 30 minutes) within a high-vacuum furnace (<1×10^{-6} Torr). After post-annealing, the magnetic properties and damping constants of these films are systematically investigated as a

function of T_{ann}. For comparison, a reference sample of Ta(7)/$Co_{20}Fe_{60}B_{20}$(1.2)/MgO(2)/Ta(3) is also prepared to examine the effect of seeding layer to the damping constant of these PMA films. The effective saturation magnetization (M_s) and anisotropy of these films are measured with the Vibrating Sample Magnetometer (VSM) module of a Physical Property Measurement System. Figure 5.1 plots the magnetic hysteresis loops and associated magnetic properties extracted from VSM measurements.

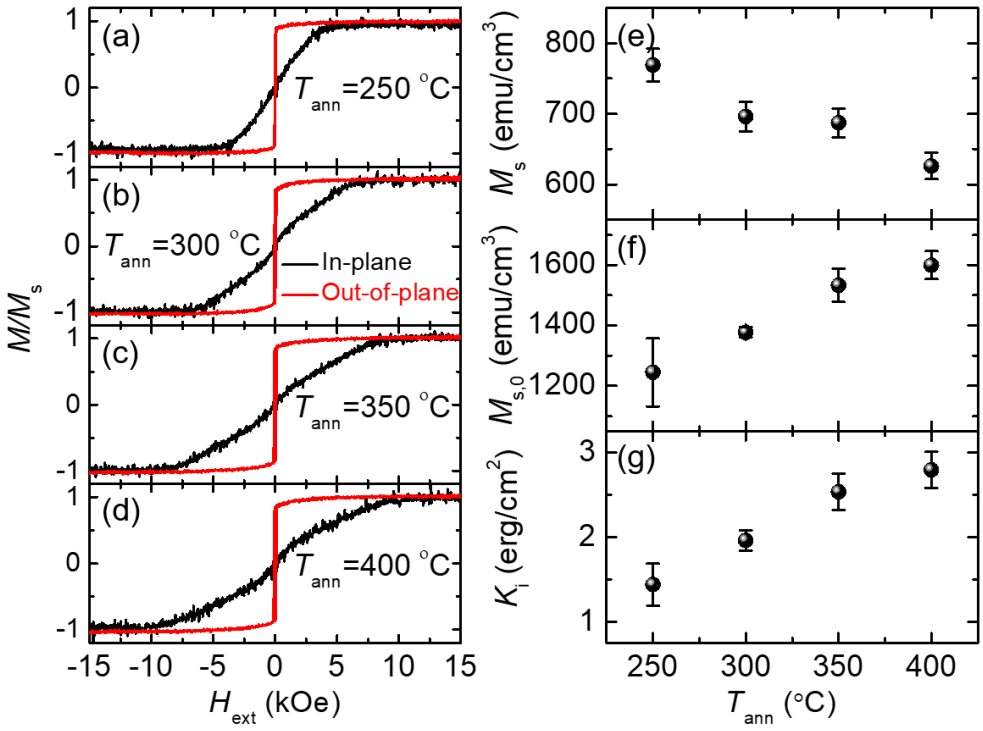

Figure 5.1. Room temperature magnetic hysteresis loops of W/CoFeB/MgO PMA thin films post-annealed at (a) 250 °C, (b) 300 °C, (c) 350 °C, and (d) 400 °C. Black and red curves denote external magnetic field (H_{ext}) applied along and perpendicular to the film plane, respectively. (e - g) Plots of the effective saturation magnetization (M_s), the intrinsic saturation magnetization (i.e., excluding the effect of the dead layer, $M_{s,0}$), and the interfacial anisotropy (K_i) as functions of T_{ann}.

The determination of the interfacial anisotropy (K_i) requires the effective anisotropy field ($H_{k,eff}$) and the intrinsic saturation magnetization ($M_{s,0}$) as input parameters, predetermined from the magnetic hysteresis measurements with a VSM. $M_{s,0}$ is obtained by finding the slope of the

areal saturation magnetization ($M_s \times t$) as a function of thickness (Fig. 5.3). The uncertainty of $M_{s,0}$ is treated as the standard error of the slope from fitting. To determine $H_{k,eff}$, we perform a linear fitting of the normalized magnetization (M/M_s) in the negative H_{ext} range. Only data in the intermediate range of H_{ext} are used to avoid multi-domain effects at low fields and saturation effects at high fields. Extrapolating this linear fit to the point where $M/M_s = -1$ provides $H_{k,eff}$. This process is depicted as the blue lines in Fig. 5.2.

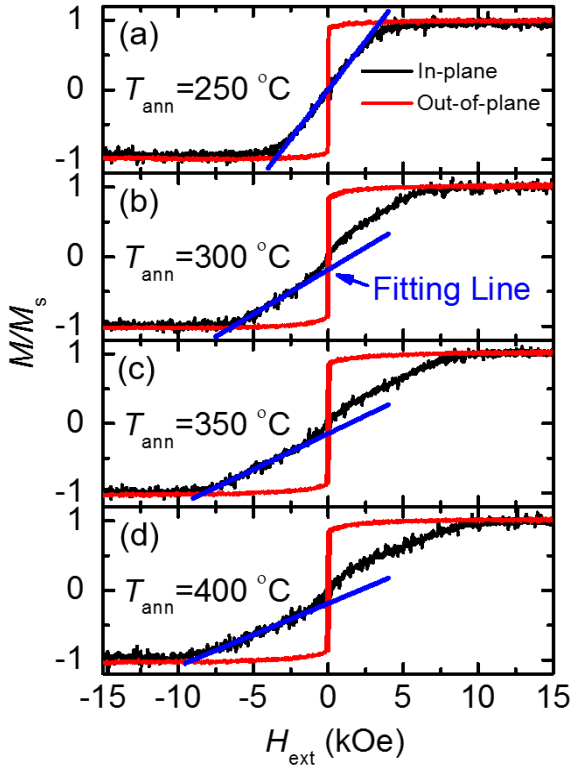

Figure 5.2. The fitting procedure to extract $H_{k,eff}$ from VSM data. (a - d) represent the series of samples annealed at 250, 300, 350, and 400 °C respectively. Uncertainties in the $H_{k,eff}$ values come from fitting error and measurement uncertainty, and are ~10%.

Once $H_{k,eff}$ and M_s are determined, the effective anisotropy (K_{eff}) can be calculated. This term incorporates the crystalline, interfacial, and shape anisotropy sources as shown in Eqs. 5.1 and 5.2 [133,134].

$$K_{\text{eff}} = \frac{1}{2} H_{\text{k,eff}} M_{\text{s,0}} \quad 0.1$$

$$K_{\text{eff}} = K_{\text{u}} + \frac{K_{\text{i}}}{t} - 2\pi M_{\text{s,0}}^2 \quad 0.2$$

Here we adopt the standard that the interfacial anisotropy is predominantly due to the CoFeB/MgO interface, such that the factor of 2 is excluded from the interfacial anisotropy term [135]. For ultrathin CoFeB films (~1 - 2.5 nm in this work), the bulk crystalline anisotropy (K_u) is negligible. This leads to K_{eff} being dominated by K_i, which is effective over the total thickness of the CoFeB layer (t), and the shape (demagnetization) energy (Eq. 5.2). The values of K_i for all samples range from 1.4 to 2.8 erg cm^{-2}, which is slightly higher than previously reported values for annealed W/CoFeB/MgO films (1.6 to 2.0 erg cm^{-2} for T_{ann} between 300 and 400 °C) [133]. However, these values of K_i are derived based on the total film thickness including the dead layer. Calculation of K_i with the reduced thickness (excluding the dead-layer effect) would result in values of K_i from 1.5 to 1.6 erg cm^{-2} in the same temperature range, which are in better agreement with the results in Ref. [133].

With the increase of T_{ann}, M_s for the W/CoFeB/MgO films decreases from ~780 to ~630 emu cm^{-3} (Fig. 5.1e). We attribute the decrease of M_s at high T_{ann} to the growth of a dead layer at the CoFeB interfaces, which becomes prominent at higher T_{ann}. To quantitatively determine the thickness of the dead layer as T_{ann} increases, we prepare four sets of PMA stacks of W(7)/CoFeB(t)/MgO(2)/Ta(3). One set contains five stacks with varying thicknesses for the CoFeB layer (t = 1.2, 1.5, 1.8, 2.2, and 2.5 nm) and is post-annealed at a fixed T_{ann}. Four T_{ann} of 250, 300, 350, and 400 °C are used for four sets of the PMA stacks, respectively. The annealing conditions are the same as those for the W(7)/CoFeB(1.2)/MgO(2)/Ta(3) samples discussed previously. We measure the magnetic hysteresis loops of these samples using VSM and plot their saturation magnetization area product ($M_s \times t$) as a function of film thickness (t) in Fig. 5.3. Linear

extrapolation of the $M_s \times t$ data provides the dead-layer thickness, at which the magnetization reduces to zero as illustrated by the *x*-axis intercept in Fig. 5.3. The slope of the linear fit also provides intrinsic saturation magnetization ($M_{s,0}$), which corresponds to the saturation magnetization after the removal of the dead-layer effect. The values of M_{s0} (Fig. 5.1f) show an increasing trend with T_{ann} from ~1300 to ~1600 emu cm^{-3}, which agrees well with previous measurement results for W/CoFeB/MgO films [133].

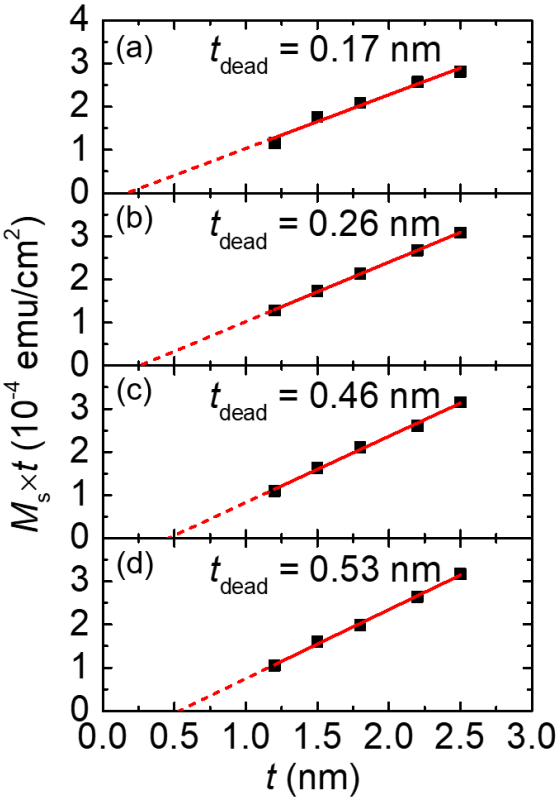

Figure 5.3. The dead-layer extraction results. (a - d) represent the series of samples annealed at 250, 300, 350, and 400 °C respectively. The t_{dead} value is the extrapolated *x*-axis intercept from the linear fitting of the thickness-dependent saturation magnetization area product ($M_s \times t$).

5.2 Characterization of crystalline structure and interfaces

X-ray diffraction (XRD) was carried out on a Siemens D5005 diffractometer with Cu-Kα radiation. Since no discernible CoFeB peaks could be identified on the 1.2-nm thick CoFeB films [136], we further fabricated thicker CoFeB films (20 nm in thickness) following a stack structure of Si/SiO_2 sub./MgO(2)/CoFeB(20 nm)/Ta(3) from bottom to top. These thicker films were annealed at 250, 300, 350, and 400 °C, respectively. The out-of-plane θ-2θ XRD patterns are plotted in Fig. 5.4.

Due to the challenges in XRD analysis of CoFeB thin films, the CoFeB (110) peak is indiscernible in Fig. 5.4 for films annealed at low T_{ann}. For films annealed at 400 °C, the CoFeB (110) peak can be weakly observed, indicating improved crystallinity. In addition, the CoFeB (200) peak can be clearly observed when T_{ann} is 350 °C or higher, as a direct demonstration of the crystalline CoFeB formation. Both peaks indicate that with the increase in T_{ann}, the CoFeB layer becomes more ordered.

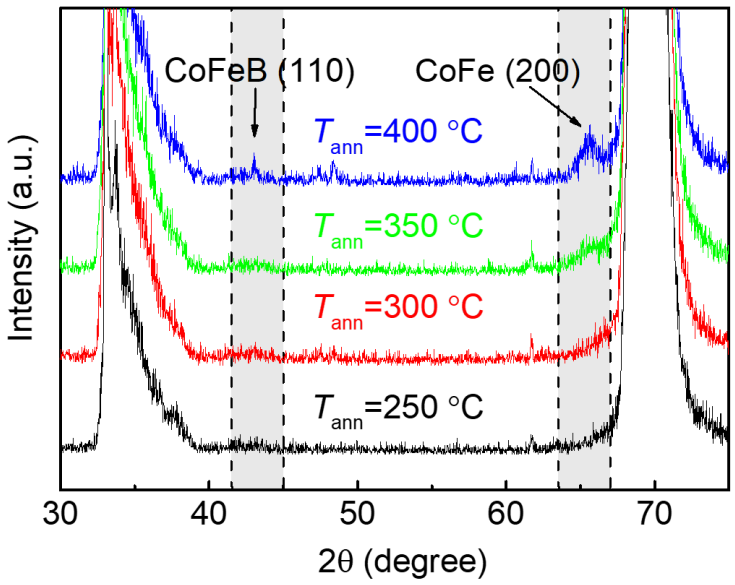

Figure 5.4. X-ray diffraction θ-2θ scan taken with the scattering vector along the film normal of the CoFeB samples post-annealed at temperatures from 250 to 400 °C.

To determine the interfacial roughness of the W/CFB/MgO thin films, an approximate value of the interfacial roughness was obtained by fitting X-ray reflectivity (XRR) data of the thin films [137]. XRR measurements were carried out on a PANalytical X'Pert high-resolution diffractometer with Cu-Kα radiation. We utilized the GenX software package to fit XRR curves, which provides the information of X-ray scattering length density (SLD) [138]. Despite many possible solutions for the XRR whole curve fitting, these results should reflect the true sample structure, as suggested by the good agreement between the fit and the measured data in Fig. 5.5. The interfacial roughness values at both interfaces of the CoFeB PMA layer are listed in Fig. 5.5 (the value in blue is for the CoFeB/MgO interface and the value in red is for the W/CoFeB interface). The XRR data indicate a slight decrease in the roughness of both interfaces with the increase of the post-annealing temperature; however, such reduction in roughness approaches the XRR limit.

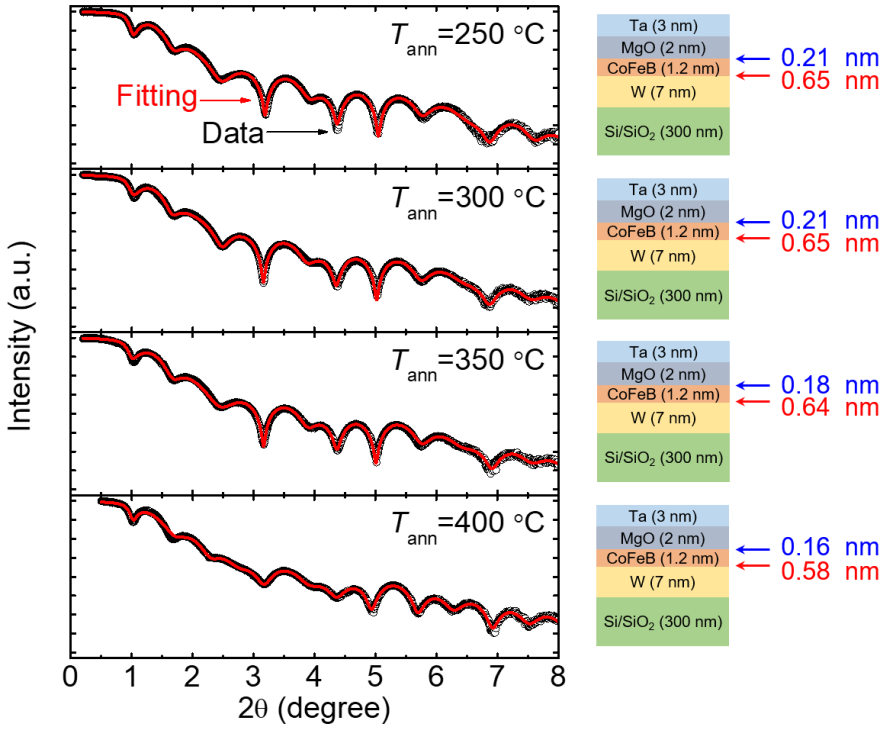

Figure 5.5. XRR data of the W/CFB/MgO samples post-annealed at T_{ann} = 250, 300, 350, and 400 °C on a log scale. Black circles are the measured data while the red line indicates the GenX fit. Extracted interfacial roughness for the MgO/CoFeB and CoFeB/W interfaces are provided for each T_{ann}.

Since the decrease in the interfacial roughness is within the XRR limit, we conclude that the interfacial roughness does not make significant contribution to the changes in damping when T_{ann} increases. On the other hand, the W diffusion becomes more active at higher T_{ann}, which tends to increase the damping constant due to its large spin-orbit coupling [47]. The W diffusion dominates when T_{ann} is higher than 350 ^{o}C, leading to the increase in damping.

5.3 TR-MOKE Measurements

The magnetization dynamics of these PMA thin films are determined using the all-optical Time-Resolved Magneto-Optical Kerr Effect (TR-MOKE) method [24,73,98,102,139,140]. This pump-probe method utilizes ultra-short laser pulses to thermally demagnetize the sample and probe the resulting Kerr rotation angle. In the polar-MOKE configuration, θ_k is proportional to the change of the out-of-plane component of magnetization (ΔM_z in Fig. 5.6a) [62]. A description of the setup at the University of Minnesota is provided in Chapter 3. Figure 3.3 shows the setup with the inclusion of the electromagnet system. The pump and probe fluences are set at ~0.3 and 0.1 mJ/cm^2, respectively. This relatively low fluence prevents sample damage, and prohibits the decrease of anisotropy and increase in inhomogeneity due to excessive heating [104].

The TR-MOKE signal is fitted to the equation $\theta_K = A + Be^{-t/C} + D\sin(2\pi ft + \varphi)e^{-t/\tau}$, where A, B, and C are the offset, amplitude, and exponential decaying constant of the thermal background, respectively. D denotes the amplitude of oscillations, f is the resonance frequency, φ is a phase shift (related to the demagnetization process), and t is the relaxation time of magnetization precession. Directly from TR-MOKE measurements, an effective damping constant (α_{eff}) can be extracted based on the relationship $\alpha_{eff} = 1/(2\pi ft)$. However, as discussed in Section 2.3, α_{eff} is not an intrinsic material property; rather, it depends on measurement conditions, such as the applied field direction (θ_H in Fig. 5.6a), the magnitude of the applied field (H_{ext}), and inhomogeneities of the sample (e.g. local variation in the magnetic properties of the sample) [58,141].

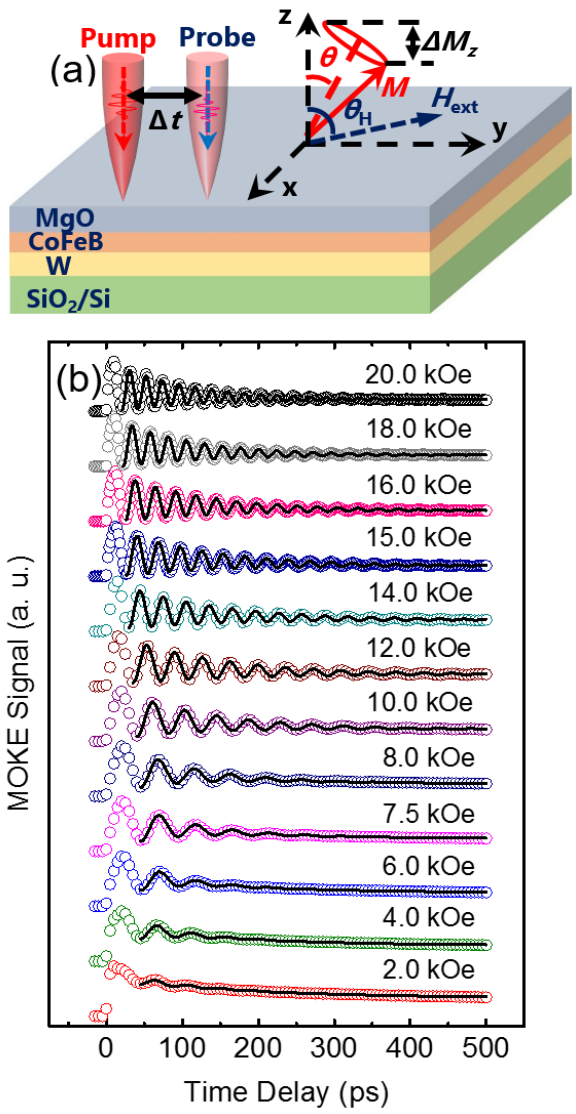

Figure 5.6. (a) Definition of the parameters and angles used in TR-MOKE experiments. The red circle indicates the magnetization precession. θ is the equilibrium direction of the magnetization. θ_k is measured by the probe beam at a given time delay (Δt). (b) The TR-MOKE data (open symbols) and model fitting of θ_k (black curves) for the 400 °C sample at 76°, for varying H_{ext} from 2.0 to 20 kOe.

To obtain the Gilbert damping constant, the inhomogeneous contribution needs to be removed from α_{eff}, such that the remaining value of damping is an intrinsic material property and independent of the measurement conditions. To determine the inhomogeneous broadening in the sample, the effective anisotropy field ($H_{k,eff} = 2K_{eff} / M_s$) needs to be pre-determined from either (1) the magnetic hysteresis loops; or (2) the fitting results of f vs. H_{ext} obtained from TR-MOKE. The

resonance frequency, f, can be related to H_{ext} through the Smit-Suhl approach by identifying the second derivatives of the total magnetic free energy, which combines a Zeeman energy, an anisotropy energy, and a demagnetization energy [20,142,143]. For a perpendicularly magnetized thin film, f is defined by Eqs. 5.3-5.6.

$$f = \frac{\gamma}{2\pi}\sqrt{H_1 H_2}\,, \tag{0.3}$$

$$H_1 = H_{ext}\cos(\theta - \theta_H) + H_{k,eff}\cos^2(\theta)\,, \tag{0.4}$$

$$H_2 = H_{ext}\cos(\theta - \theta_H) + H_{k,eff}\cos(2\theta)\,, \tag{0.5}$$

$$2H_{ext}\sin(\theta_H - \theta) = H_{k,eff}\sin(2\theta)\,. \tag{0.6}$$

This set of equations permits calculation of f with the material gyromagnetic ratio (g), H_{ext}, θ_H, $H_{k,eff}$, and the angle between the equilibrium magnetization direction and the surface normal (θ, determined by Eq. 5.6). The measured values of f as a function of H_{ext} can be fitted to Eq. 5.3 by treating g and $H_{k,eff}$ as fitting parameters. To minimize the fitting errors resulting from the inhomogeneous broadening effect that is pronounced at the low fields, we use measured frequencies at high fields (H_{ext} > 10 kOe) to determine $H_{k,eff}$.

With a known value of $H_{k,eff}$, the Gilbert damping constant of the sample can be determined through a fitting of the inverse relaxation time ($1/\tau$) to Eq. 5.7. The two terms of Eq. 5.7 account for, respectively, contributions from the intrinsic Gilbert damping of the materials (first term) and inhomogeneous broadening (second term) [58]:

$$\frac{1}{\tau} = \frac{1}{2}\alpha\gamma(H_1 + H_2) + \frac{1}{2}\left|\frac{d\omega}{dH_{k,eff}}\right|\Delta H_{k,eff}\,, \tag{0.7}$$

where H_1 and H_2 are related to the curvature of the magnetic free energy surface as defined by Eqs. 5.4 and 5.5 [143,144]. The second term on the right side of Eq. 5.7 captures the inhomogeneous effect by attributing it to a spatial variation in the magnetic properties ($\Delta H_{k,eff}$), analogous to the linewidth broadening effect in Ferromagnetic Resonance measurements [94]. The

magnitude of $d\omega / dH_{k,eff}$ can be calculated once the relationship of ω vs. H_{ext} is determined with a numerical method. Both α and $\Delta H_{k,eff}$ (the inhomogeneous term related to the amount of spatial variation in $H_{k,eff}$) are determined *via* the fitting of the measured $1/\tau$ based on Eq. 5.7. In this way, we can uniquely extract the field-independent α, as an intrinsic material property, from the effective damping (α_{eff}), which is directly obtained from TR-MOKE and dependent on H_{ext}.

It should be noted here that the inhomogeneous broadening of the magnetization precession is presumably due to the multi-domain structure of the materials, which becomes negligible in the high-field regime ($H_{ext} >> H_{k,eff}$) as the magnetization direction of multiple magnetic domains becomes uniform. This is also reflected by the fact that the derivative in the second term of Eq. 5.7 approaches zero for the high-field regime [103].

5.4 Angular Dependence of Precessional Resonance Frequency

To gain some insight into the impact of applied field direction (θ_H) on the resonance frequency (f), we conduct numerical simulations of the field dependent resonance frequency for a representative sample with $\gamma = 1.76\times10^{11}$ rad s^{-1} T^{-1}, $H_{k,eff} = 2.5$ kOe, and $\theta_H = 90°$, 89°, and 80°. The results of f vs. H_{ext} calculated with Eqs. 5.3-5.6 are presented in Fig. 5.7. The difference in f between $\theta_H = 90°$ and $\theta_H = 89°$ is pronounced when the external fields are close to $H_{k,eff}$, but almost negligible elsewhere. For $\theta_H = 90°$, f approaches 0 GHz at $H_{ext} = H_{k,eff}$ as the magnetization theoretically saturates along the direction of H_{ext}. For any other value of θ_H, f experiences a non-zero minimum at $H_{ext} \approx H_{k,eff}$, and this minimum feature of f becomes less apparent when θ_H deviates from 90°. This is demonstrated by the blue curve in Fig. 5.7 for $\theta_H = 80°$, which shows a very shallow and small dip feature of f when H_{ext} is close to $H_{k,eff}$. For high branch data at $H_{ext} >> H_{k,eff}$, the slope of f as a function of H_{ext} will always converge to the same value ($\gamma/2\pi$), regardless of θ_H.

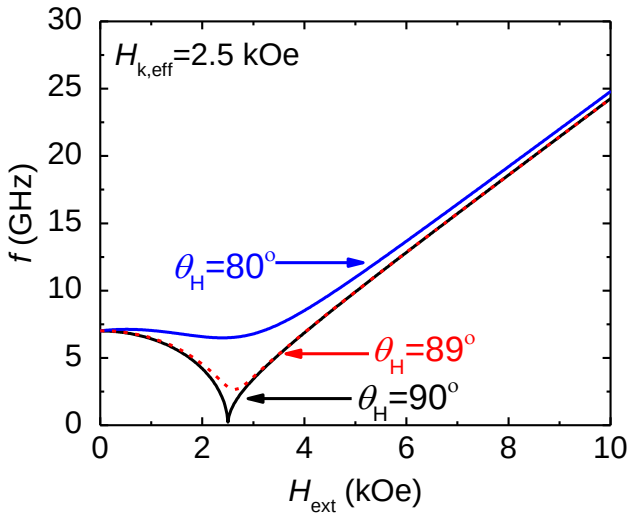

Figure 5.7. Numerical modeling of f vs. H_{ext} based on Eqs. 5.3-5.6 for a representative sample with $\gamma = 1.76\times10^{11}$ rad s^{-1} T^{-1} and $H_{k,eff} = 2.5$ kOe, predicted at $\theta_H = 90°$, 89°, and 80°.

5.5 Uncertainty Analysis

The error bars for K_i in Fig. 5.1g are determined by propagating errors from $H_{k,eff}$, $M_{s,0}$, and the dead layer, all of which have been determined through VSM measurements. We also include an error in the deposited thickness of CoFeB, which is less than 5%. A root sum of squares of errors propagated from various terms in the anisotropy (such as the $M_{s,0}$ and measured $H_{k,eff}$ in Eqs. 5.1 and 5.2) is utilized to determine the overall error of K_i.

Reported uncertainties in f and τ are from the standard error in fitting of the raw TR-MOKE signal (see Fig. 5.6). The standard error of f is typically negligible and therefore is not shown. The standard errors of individual points of τ (and thus $1/\tau$) depend on the number of oscillations and the signal fluctuation in TR-MOKE measurements, which are typically small as determined from mathematic fitting (Figs. 5.9b and 5.9d). The model prediction of $1/\tau$ (and thus α_{eff}) has larger discrepancies with measured values near $H_{k,eff}$ where α_{eff} is large (as shown by the predicted α_{eff} in Fig. 5.8), which prompts our primary focus on high-field data ($H_{ext} > H_{k,eff}$) to determine α from the fitting of $1/\tau$.

To estimate the uncertainty of $H_{k,eff}$ from TR-MOKE, both the standard error from fitting f vs. H_{ext} and the error propagated from the H_{ext} uncertainty are included. The uncertainty of H_{ext} is determined by the instrument resolution of the Hall sensor. Differentiating $H_{k,eff}$ with respect to H_{ext} (Eq. 5.3), the error propagation from H_{ext} can be approximated. At high fields and $\theta_H = 90^o$, a 500 Oe uncertainty of H_{ext} results in <25% uncertainty of $H_{k,eff}$.

$$\frac{\partial H_{k,eff}}{\partial H_{ext}} = 1 + \frac{1}{H_{ext}^2}\left(\frac{2\pi f}{\gamma}\right)^2 \qquad 0.1$$

The uncertainty of α also primarily comes from two sources: the standard error from the fitting of $1/\tau$ to measured data ($\Delta\alpha_{SE}$) and the error propagated from $H_{k,eff}$. The best fit for the reported $H_{k,eff}$ for the 250 ºC W/CoFeB/MgO sample is shown as the black line in Fig. 5.8. The red and blue dashed lines in Fig. 5.8 portray the fit of $1/\tau$ when $H_{k,eff}$ is adjusted to the upper (blue) and lower (red) limits of its error bar. As mentioned previously, we focus on the high-field data ($H_{ext} \geq 10$ kOe) to prompt the accuracy in determining α. The fittings converge when $H_{ext} \sim 10$ kOe, which indicates that our choice of fitting the data of $H_{ext} \geq 10$ kOe should provide an accurate value of α. The fittings result in α_{high} and α_{low}, which correspond to α determined at the upper and lower limits of $H_{k,eff}$, respectively. The final reported uncertainty in damping ($\Delta\alpha$) is then calculated with Eq. 5.9, which ranges from 20 to 25%.

$$\Delta\alpha = \sqrt{\left(\frac{\alpha_{high} - \alpha_{low}}{2}\right)^2 + \left(\Delta\alpha_{SE}\right)^2} \qquad 0.2$$

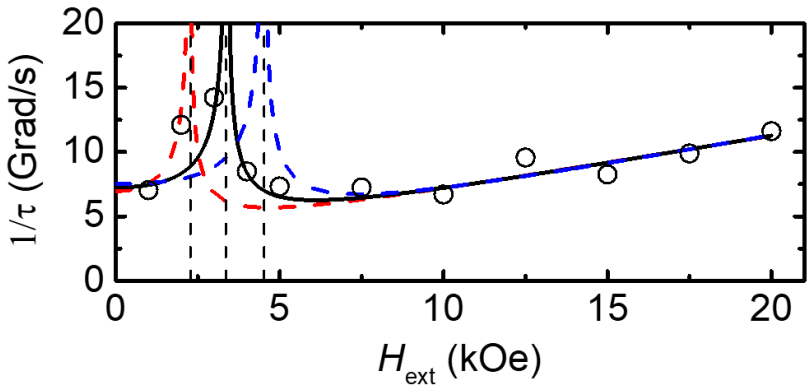

Figure 5.8. Depiction of the fitting process of $1/\tau$ to determine α and $\Delta\alpha$. The black line indicates the best fit to the measured values of $1/\tau$. The red and blue dotted lines show the fitting of $1/\tau$ when the uncertainty in $H_{k,eff}$ is included.

5.6 Results and Discussion

The measurement method is validated by measuring the T_{ann} = 400 °C at multiple angles (θ_H) of the external magnetic field direction. By repeating this measurement at varying θ_H, we can show that α is an intrinsic material property, independent of θ_H. Figure 5.9a plots the resonance frequencies derived from TR-MOKE and model fittings for the 400 °C sample at two field directions (θ_H = 76° and 89°). For the data acquired at θ_H = 89°, a minimum f occurs at $H_{ext} \approx H_{k,eff}$. This corresponds to the smallest amplitude of magnetization precession, when the equilibrium direction of the magnetization is aligned with the applied field direction at the magnitude of $H_{k,eff}$ [143]. The dip at this local minimum diminishes when θ_H decreases, as reflected by the comparison between the red (θ_H = 89°) and blue (θ_H = 76°) lines in Fig. 5.9. With the $H_{k,eff}$ extracted from the fitting of frequency data with θ_H = 89°, we generate the plot of theoretically predicted f vs. H_{ext} (θ_H = 76° theory, blue line in Fig. 5.9a), which agrees well with experimental data (open squares in Fig. 5.9a).

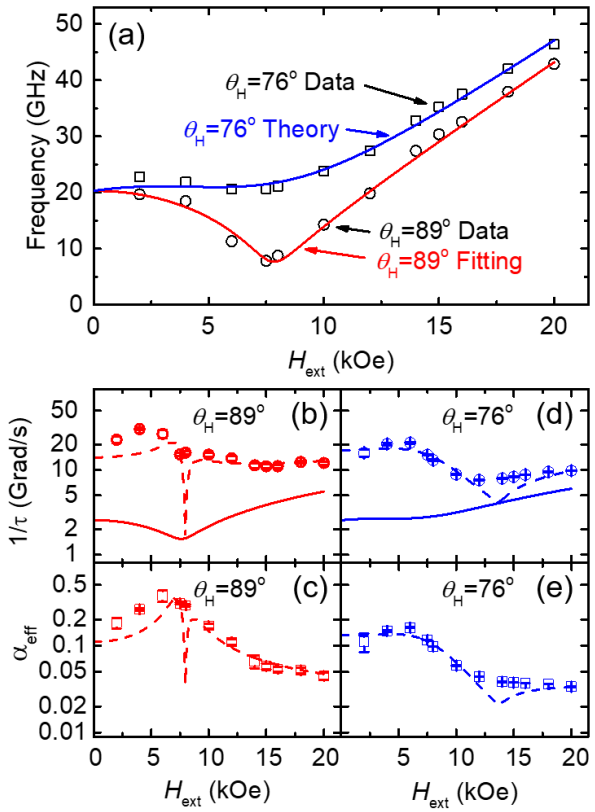

Figure 5.9. (a) Measured f vs. H_{ext} results for the 400 °C sample at θ_H = 89° (open circles) and θ_H = 76° (open squares) and corresponding modeling at θ_H = 89° (red line) and θ_H = 76° (blue line). (b) The measured inverse of relaxation time ($1/\tau$) at θ_H = 89° (open symbols) and the fitting of $1/\tau$ based on Eq. 5.7 (dotted line). For reference, the first term of $1/\tau$ in Eq. 5.7 is also plotted (solid line), which accounts for the contribution from the Gilbert damping only. (c) α_{eff} as a function of H_{ext} for θ_H = 89° (red circles). The dotted line shows the predicted α_{eff} using the α extracted from the fitting of $1/\tau$. (d) and (e) depict similar plots of $1/\tau$ and α_{eff} for θ_H = 76°.

The inverse relaxation time ($1/\tau$) should also have a minimum value near $H_{k,eff}$ for θ_H = 89° if the damping was purely from Gilbert damping (as shown by the solid lines in Figs. 5.9b and 5.9d); however, the measured data do not follow this trend. Adding the inhomogeneous term (dotted lines in Figs. 5.9b and 5.9d) more accurately describes the field dependence of the measured $1/\tau$ (open symbols in Figs. 5.9b and 5.9d). It should be noted that the dip of the predicted $1/t$ occurs when the frequency derivative term in Eq. 5.5 approaches zero; however, this is not captured by the measurement. Figures 5.9c and 5.9e depict the field-dependent effective damping (α_{eff}) calculated using the Gilbert damping (α) extracted from fitting the measured $1/\tau$.

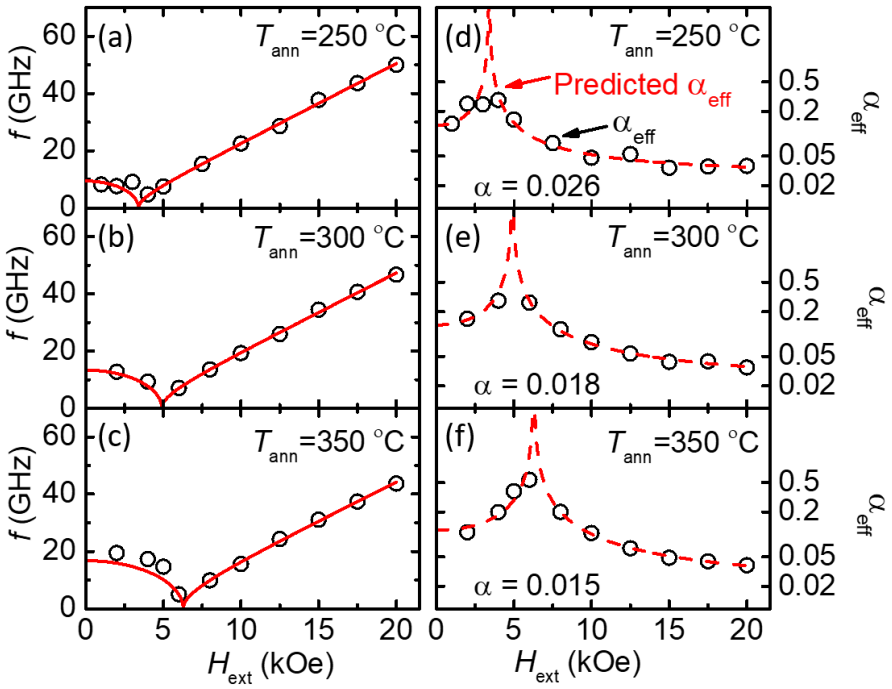

Figure 5.10. Results for f (a - c) and α_{eff} (d - f), on a log scale, for individual samples (excluding the 400 °C sample, which is discussed in Fig. 5.9). The fitting for f is shown as a solid red line. The dashed line in (d - f) indicates the predicted α_{eff} from the values of α extracted from fitting $1/\tau$. All three samples are measured at $\theta_H = 90°$.

With the knowledge that the value of α extracted with this method is the intrinsic material property, we repeat this data reduction technique for the annealed W/CoFeB/MgO samples discussed in Fig. 5.1. The symbols in Fig. 5.10 represent the resonance frequencies and damping constants (both effective damping and Gilbert damping) for all samples measured at $\theta_H \approx 90°$. The fittings for the resonance frequency based on Eq. 5.3 (red lines) are also shown to demonstrate the good agreement between our TR-MOKE measurement and theoretical prediction. The uncertainties of f, τ, and $H_{k,eff}$ are calculated from the least-squares fitting uncertainty and the uncertainty of measuring H_{ext} with the Hall sensor.

The summary of the anisotropy and damping measured via TR-MOKE is shown in Fig. 5.11. Figure 5.11a plots $H_{k,eff}$ obtained from VSM (black open circles) and TR-MOKE (blue open squares), both of which exhibit a monotonic increasing trend as T_{ann} becomes higher. Discrepancies

in $H_{k,eff}$ from these two methods can be attributed to the difference in the size of the probing region, which is highly localized in TR-MOKE but sample-averaged in VSM. Since $H_{k,eff}$ determined from TR-MOKE is obtained from fitting the measured frequency for a localized region, we expect these values more consistently describe the magnetization precession than those obtained from VSM. The increase in $H_{k,eff}$ with T_{ann} has previously be partially attributed to the crystallization of the CoFeB layer [58]. For temperatures higher than 350 °C, this increasing trend of $H_{k,eff}$ begins to lessen, presumably due to the diffusion of W atoms into the CoFeB layer, which is more pronounced at higher T_{ann}. The W diffusion process is also responsible for the decrease in M_s of the CoFeB layer as T_{ann} increases (Fig. 5.1e). Subsequently, the decrease in M_s leads to a further-reduced demagnetizing energy and thus a larger $H_{k,eff}$.

Similar observation of M_s has been reported in literature for Ta/CoFeB/MgO PMA structures and attributed to the growth of a dead layer at the heavy metal/CoFeB interface[145]. Figure 5.11b summarizes t_{dead} as a function of T_{ann} with t_{dead} increasing from 0.17 to 0.53 nm as T_{ann} changes from 250 to 400 ^{o}C, as discussed in Section 5.1.

Figure 5.11c depicts the dependence of α on T_{ann}, which first decreases with T_{ann}, reaches a minimum of 0.015 at 350 °C, and then increases as T_{ann} rises to 400 °C. Similar trends have been observed for Ta/CoFeB/MgO previously (minimum α at T_{ann} = 300 °C) [58]. We speculate that this dependence of damping on T_{ann} is due to two competing effects: (1) the increase in crystallization in the CoFeB layer with T_{ann} which reduces the damping, and (2) the growth of a dead layer, which results from the diffusion of W and B atoms and is prominent at higher T_{ann}.

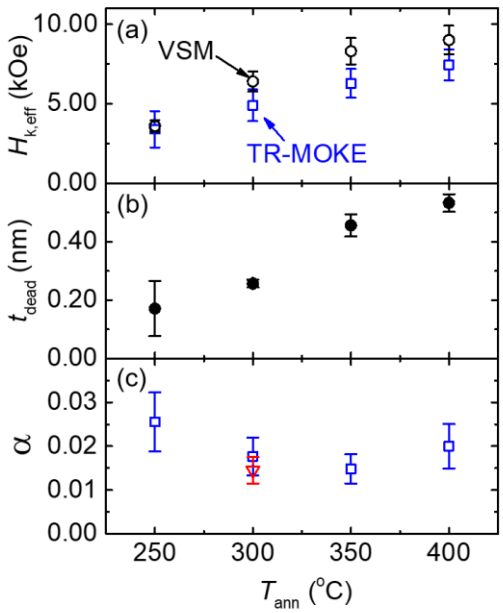

Figure 5.11. Summary of the magnetic properties of W-seeded CoFeB as a function of T_{ann}. (a) The dependence of $H_{k,eff}$ on T_{ann} obtained from both the VSM (black open circles) and TR-MOKE fitting (blue open squares). (b) The dependence of dead-layer thickness on T_{ann}. Error bars are from standard error from a linear fit. (c) Damping constants as a function of T_{ann}. The minimum damping constant of $\alpha = 0.015$ occurs at 350 °C. The values for the all samples are obtained from measurements at $\theta_H \approx 90°$. For comparison, α of the reference Ta/CoFeB/MgO PMA sample annealed at 300 °C is also shown as a red triangle.

As the amorphous as-deposited CoFeB film begins to form ordered phases at elevated temperatures, the number of scattering sites in the film tend to decrease [45,146]. The increase in crystallinity of the W/CoFeB/MgO film with T_{ann} is demonstrated by the XRD analysis detailed in Section 5.2. At T_{ann} = 400 °C, the dead-layer formation leads to a larger damping presumably due to an increase in scattering sites (diffused W atoms) that contribute to spin-flip events, as described by the Elliott-Yafet relaxation mechanisms [38]. Additionally, W atoms can increase the spin-orbit coupling and thus the damping as the inter-diffusion increases with T_{ann} [147]. The observation that our W-seeded samples still sustain excellent PMA properties at T_{ann} = 400 °C confirms their enhanced thermal stability, compared with Ta/CoFeB/MgO stacks which fail at T_{ann} = 350 °C or higher.

While the damping constants are comparable for the W/CoFeB/MgO and Ta/CoFeB/MgO films annealed at 300 °C, our work focuses on the enhanced thermal stability of W-seeded CoFeB PMA films that can maintain a relatively low damping constant (0.020 at 400 °C). Such an advantage enables W-seeded CoFeB layers to be viable and promising alternatives to Ta/CoFeB/MgO, which is currently widely used in spintronic devices.

CHAPTER 6: COUPLING BETWEEN MAGNETIZATION DYNAMICS AND PICOSECOND ACOUSTICS

This chapter is a discussion of the coupling between spin and strain as measured by the TR-MOKE method. This chapter contains portions of two previous publications. The discussion of magnetostriction and magnetism from the IOP Book Chapter was written by me. TDTR and TR-MOKE measurements were conducted by me, samples were made by Delin Zhang (postdoc in Prof. Jian-Ping Wang's group), simulations were conducted by Tao Qu (postdoc in Prof. Randall Victora's group), previous TDTR and TR-MOKE measurements on samples not discussed here were done by Jie Zhu (former postdoc in Xiaojia Wang's group).

1. Lattery, D., Zhu, J., Huang, D., and Wang, X.J., "Ultrafast Thermal and Magnetic Characterization of Materials Enabled by the Time-Resolved Magneto-Optical Kerr Effect", invited IOP Book Chapter in Nanoscale Energy Transport: Emerging Phenomena, Methods and Applications (2020), pp. 9-1 to 9-30.
2. Zhang, D.L., Zhu, J., Qu, T., Lattery, D. M., Victora, R. H., Wang, X.J., Wang, J.-P., "High frequency magneto-acoustic resonance through strain-spin coupling in perpendicular multilayers", Science Advances (In Revision).

Magnetostriction is a well-known phenomenon in which the magnetization within a magnetic material causes a structural deformation and can even launch acoustic strains [148]. The inverse effect is also important, especially in pump-probe measurements that create longitudinal strain waves *via* thermal expansion after optical excitation [86,88]. This strain will create picosecond acoustic signals in TDTR measurements that can be used to determine the thickness of thin films. Through the inverse magnetostriction effect, strain waves can also influence magnetization dynamics, as shown in the study of ferromagnetic Ni films by Kim *et al.* [149]. Further research has also shown how this effect can be achieved by using materials with large magnetostriction, such as Galfenol (an alloy of Fe and Ga) [150], or controlling the strain in the material through the use of acoustic Bragg mirrors [151]. This has directly led to the exploration of innovative approaches and new physics to couple the energy transfer between the magnetic system (magnons) and the lattice (phonons), renewing the interesting in both the scientific and technological communities [152,153]. Among the abundant physical phenomena [154-157] arising from the magnon-phonon coupling, strain-assisted magneto-acoustic resonance in ferromagnetic materials

provides an energetically efficient path for rapid switching of spin states, which is required for applications in advanced spin memory, logic, and other spintronic devices [158-160].

Exploring innovative approaches and new physics to manipulate the magnetization of ferromagnetic materials via femtosecond laser pulses has recently received renewed interests in both scientific and technological communities in areas such as all-optical switching [152,153,161]. Simultaneously, the experimental utilization of femtosecond lasers to manipulate the magnetic properties of materials with perpendicular magnetic anisotropy (PMA) through the coupling between strain and spin has become a promising area for developing ultralow-energy spin memory and logic devices [158-160,162,163]. Utilizing the coupling between strain and magnetization can potentially offer a unique non-thermal approach to excite magnetization precession for realizing high-speed and low-energy switching in spintronics.

To this point, the main efforts have been devoted to strain generated from piezoelectric materials *via* electrical methods [164-167]. It was first discovered by Beaurepaire *et al*. in 1996 that femtosecond laser pulses can modify the magnetization of ferromagnetic materials through thermally induced demagnetization [70]. This ultrafast optical approach provides a powerful tool for capturing the energy-carrier interactions between electrons, spins, and phonons in the femtosecond time regime [168-173]. At the same time, acoustic strain waves (ASWs) can be launched by femtosecond laser pulses through thermal expansion [149-151,158,174-178]. Upon femtosecond laser pulse excitation, ASWs directly act through the entire FM film via the inverse magnetostriction effect (or Villari effect), and thus can readily couple with the spins to modify the magnetic anisotropy and, subsequently, magnetization of a FM material. Thus, by simultaneously generating strain and spin within the ferromagnetic layer, the ultrafast optical approach provides a powerful tool to initiate the coupling between phonons and magnons. The femtosecond time scale of the laser pulse is smaller than the relaxation time scales of phonons and magnons, which allows the capture of the magnon-phonon coupling processes in the time domain, such as strain-assisted

large-angle magnetization precession [158]. In contrast, efforts have also been devoted to launching strain electrically by using piezoelectric materials [164,166,167], which induce a Surface Acoustic Wave (SAW) in the substrate beneath the FM layer. In such experiments, the SAW propagates to the FM layer and modifies its FM properties by changing the lattice spacing, leading to a different phonon propagation direction.

Motivated by this potential, many experimental and theoretical studies have reported the magnetization dynamics of ferromagnetic thin films under optically generated ASWs. The materials studied so far have not been applicable to spintronic applications due to low magnetic moment, low anisotropy, or low Curie temperature, such as dilute semiconductor materials [174-178] and metallic FM materials (e.g., Terfenol-D ($(Tb_xDy_{1-x})Fe_2$) [158], Galfenol [150,151], Bi-YIG [179] and Ni [149]). As a matter of fact, direct experimental demonstration of the coupling between ASWs and spins in technologically relevant PMA materials remains elusive, despite the fundamental importance of the physical mechanisms of magnetic resonance. $[Co/Pd]_n$ multilayers possess high PMA at room temperature, holding great potential for various technological applications [180-184]. Furthermore, $[Co/Pd]_n$ multilayers have a relatively large magnetostriction coefficient λ ($\sim -1\times10^{-4}$) [185,186], holding great potential for various technological applications [180-184]. This could serve as an ideal platform for investigating the magnon-phonon coupling.

Here we experimentally report an extremely-high frequency (EHF) magneto-acoustic resonance up to 60 GHz in the PMA $[Co/Pd]_n$ multilayers, originating from strong magnon-phonon coupling following excitation by femtosecond laser pulses. The resonance shows an enhanced wave envelope in the time domain, an anti-crossing in frequency domain, and significant mixing of both magnons and phonons as predicted by a coupled model. Such an observation is also demonstrated by both ultrafast measurement signals and micromagnetic simulation. These observations all indicate that a hybridized quasiparticle comprised of both magnon and phonon exists in perpendicular magnetic multilayers, whereby the energy transfers among magnon and phonon

systems efficiently. This allows the acoustic wave to substantially influence the magnetization at an ultrafast picosecond scale. Thus, our work paves a potential pathway to enable an EHF magnetic-acoustic resonance through the strain-spin coupling and suggest a possibility of ultrahigh-speed strain-assisted magnetization switching in a technologically relevant magnetic system.

6.1 Sample Information

All samples with the stack of $[Co(x)/Pd(y)]_n/Co(x)/Ta(3)$ (x = 0.30~0.70 nm; y = 0.70~1.80 nm), from the bottom to top, are deposited on Si/SiO_2(300 nm) substrate at room temperature using a six-target Shamrock magnetron sputtering system with ultra-high vacuum (base pressure $<5.0 \times 10^{-8}$ Torr). The $[Co(0.8\ nm)/Pd(1.8\ nm)]_{11}$ multilayer is seeded with Ta(5 nm)/Pd(5 nm) bilayer, the others are seeded with Ta(3 nm)/Pd(3 nm) bilayer. All layers are sputtered with D.C. power sources and element targets under an Argon working pressure of 2.0 mTorr. The magnetic properties of all samples are characterized using a PPMS with the VSM module.

Figure 6.1a illustrates the TR-MOKE and TDTR measurement configuration together with a schematic of the sample stack. The thermoreflectance signals collected in TDTR measurements are proportional to the intensity change in the reflectivity of the probe beam, which contain information of both temperature and acoustics [73,86]. Thus, the TDTR signals measured here represent the strain waves in the sample. The strain wave frequency is for the lowest-frequency mode of the standing strain waves confined within the thin-film sample stack, whose half wavelength corresponds to the thickness of the entire sample stack (including the capping and seed layers). Therefore, by changing the sample thickness, the strain frequency can be tuned (discussed more in Section 6.4). In this study, we select the $[Co(0.8\ nm)/Pd(1.5\ nm)]_{11}$ multilayered structure as the model system deposited on a SiO_2 (300 nm)/Si substrate and is capped with a 3-nm Ta layer. It has perpendicular anisotropy with an effective field of $H_{k,eff} \sim 6.5$ kOe and magnetic anisotropy of $K_u \sim 4.4$ Merg/cc, as shown in Fig. 6.1b.

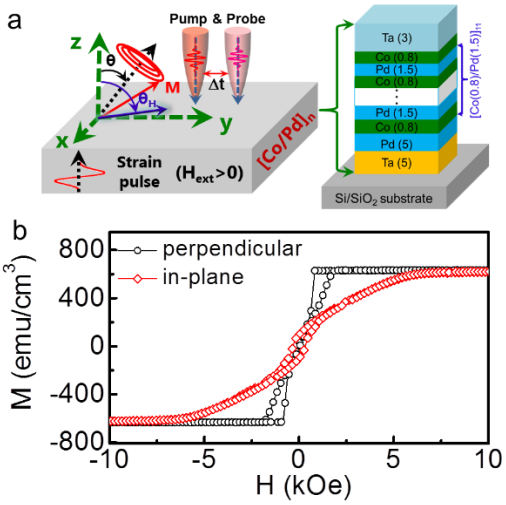

Figure 6.1 (a) Illustration of the ultrafast time-resolved magneto-optical Kerr effect (TR-MOKE) measurements (left) on the $[Co/Pd]_n$ multilayer with numbers in parentheses denoting layer thicknesses in nanometres (right). In TR-MOKE measurement, in the absence of an external magnetic field H_{ext}, the magnetostrictive effect can be measured, in which the acoustic strain wave induces the magnetization oscillation. The magnetization of $[Co/Pd]_n$ multilayer is tilted to the angle (θ) when $H_{ext} > 0$ is applied with the angle ($\theta_H = 80°$). The TR-MOKE signals will include the signal from spin precession and acoustic strain wave. By fitting the data, we can separate them and identify their coupling. The figure in the right plane of the top shows the $[Co/Pd]_n$ multilayered structure used in our work. (b) The magnetic hysteresis loops of the $[Co(0.8\ nm)/Pd(1.5\ nm)]_{11}$ multilayer with a magnetic anisotropy field $H_{k,eff}$ ~6.5 kOe.

6.2 Ultrafast Measurement Results

For a typical polar TR-MOKE measurement, a damped oscillation feature is expected in the signals due to the spin precession initiated by the rapid temperature rise from pump excitation, when an external magnetic field ($\mathbf{H}_{ext}$) is applied. However, the TR-MOKE signals usually do not show magnetization oscillations in the absence of H_{ext}, since the equilibrium axis of the spin precession will be aligned with the surface normal direction of the perpendicular magnetic film. When the sample has a large λ, acoustic waves can tilt the magnetization and therefore create a detectable change in M_z and will be captured as magnetization oscillations in the signal as well. Thus, the magnetization oscillation features captured by TR-MOKE contains both the spin precession and acoustic wave information [174]. Therefore, the signals from TR-MOKE measurements contain information of two behaviors, as the superposition of two frequencies in M_z:

loosely categorized as the field-dependent one corresponding to the typical ferromagnetic resonance resulting from coherent spin precession (spin-like), and the field-independent one caused by a time-dependent modulation of magnetic properties through strain (strain-like).

This atypical secondary frequency could be from non-MOKE components in TR-MOKE signal, whose contribution are usually found to be negligible in determining the frequencies and relaxation times of spin precession. We can understand the impact of these non-MOKE components on our signal by subtracting the TR-MOKE signals obtained with two opposite magnetic directions. To show that this non-MOKE component contributes negligibly to the magnetization precession and acoustic waves, we conduct measurements on the $[Co/Pd]_n$ multilayer, at a field when both modes are visible ($H_{ext} \approx 21$ kOe). By magnetizing the sample with a positive field, the sample magnetization of sample will be in the positive *y*-*z* plane (see the definition of coordinates in Figure 6.1a). The corresponding TR-MOKE signal is set to be positive and labeled as M^+. When the field direction is reversed, the sample magnetization is along the opposite direction (the negative *y*-*z* plane). The resulting TR-MOKE signal is set to be negative and labeled as M^-. The subtraction of these two measurements ($M^+ - M^-$) can remove the non-MOKE components [27,187].

Figure 6.2a shows the raw TR-MOKE signals of M^+, M^-, and the subtracted signal of $M^+ - M^-$ for the Co/Pd multilayer near the point where both the ASW and FMR frequencies match (the magneto-acoustic resonance point). The fact that both the strain-like mode and spin-like mode are maintained in the subtracted signal of $M^+ - M^-$ (and nearly double the amplitudes) shows that both modes are resulting from the MOKE response of the sample magnetization. The resonance frequencies and relaxation times of the strain-like mode and spin-like mode, extracted from the raw TR-MOKE signals of M^+, M^-, and the subtracted signal of $M^+ - M^-$, are depicted in Figs. 6.2b and 6.2c, respectively. The differences in the values analyzed using these three sets of TR-MOKE signals are less than 1% for the resonance frequency and less than 5% for the relaxation time,

suggesting a negligible contribution from the non-MOKE components in TR-MOKE signals. Thus, for future data analysis, we choose to show only the M^+ signals.

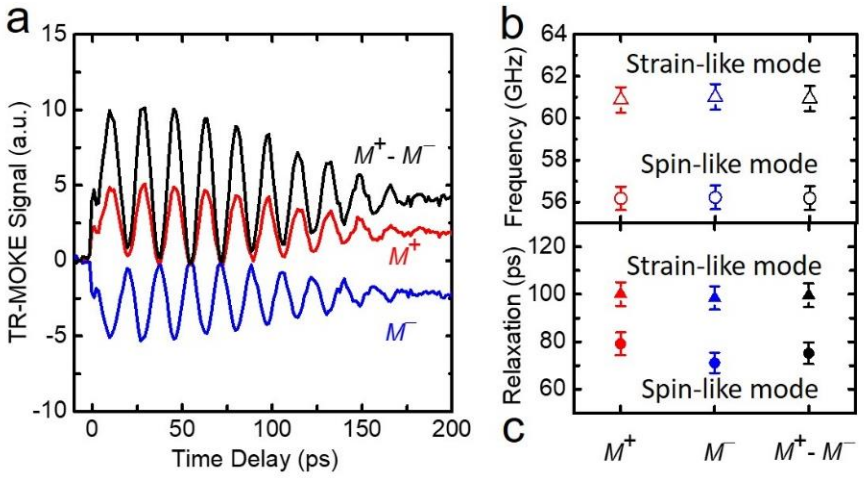

Figure 6.2. (a) The TR-MOKE signals of the Co/Pd multilayer near magneto-acoustic resonance. M^+ indicates the signal with a field of ~21 kOe applied at $\theta_H \sim 80°$ and M^- indicates the signal with the magnetization in the opposite direction ($\theta_H \sim 260°$). $M^+ - M^-$ is the subtraction of both signals (to subtract non-MOKE components). (b, c) the extracted spin-like and strain-like frequencies and relaxation times from the three different signals. Error bars are <1% for the frequency and <5% for the relaxation time, respectively.

The TR-MOKE results of $[Co(0.8\ nm)/Pd(1.5\ nm)]_{11}$ with the range of H_{ext} from 10 kOe to 29 kOe are plotted in Fig. 6.3a. Interestingly, we find that for 18 kOe < H_{ext} < 24 kOe, TR-MOKE signals show the amplitude of precessional oscillations of M_z increase instead of the usual decrease in the first 60 ps following the pump excitation. However, when H_{ext} is smaller than 16 kOe or larger than 25 kOe, the TR-MOKE signals in Fig. 6.3a appear as the damped oscillations (standard in TR-MOKE measurements of magnetization precession). Within the first several picoseconds, different energy carriers such as magnons, phonons, and electrons induced by the ultrafast laser pulse are out of equilibrium with each other. As the main goal of this work is to analyse the magnetic precession that is in the equilibrium regime, we purposefully start the fitting from 10 ps to avoid any possible non-equilibrium effects (indicated by the fitting lines in Fig. 6.3a).

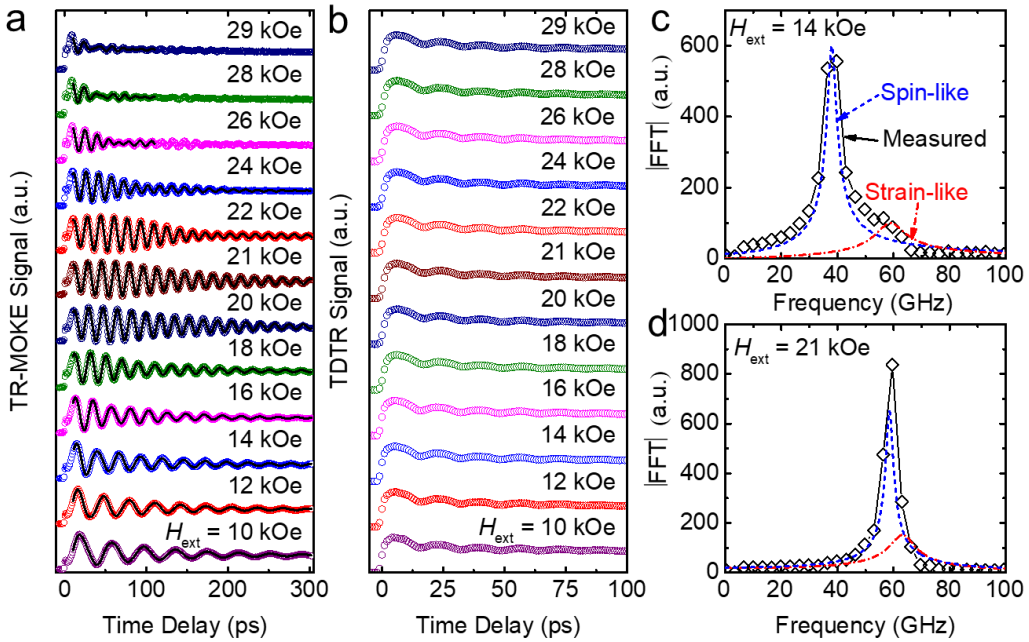

Figure 6.3. (a) the experimental and fitting TR-MOKE signals and (b) the experimental TDTR signals as a function of H_{ext} (10 to 29 kOe). It is clearly seen that TDTR signals do not change in the whole region of H_{ext} while TR-MOKE signals show different oscillation patterns with external fields. For H_{ext} < 18 kOe or > 24 kOe, magnetization precession presents the damped oscillation, while for 18 kOe < H_{ext} < 24 kOe, magnetization shows the resonance phenomenon. (c, d) Fourier transform of the TR-MOKE signal with H_{ext} = 14 kOe and 21 kOe, respectively, from which two peaks (spin-like and strain-like) can be found. For H_{ext} = 14 kOe, the two peaks are separate, however, the two peaks are overlapping when H_{ext} = 21 kOe.

From the TDTR data in Fig. 6.3b, we can find that the acoustic strains prevail in the first 60 ps, suggesting the magneto-acoustic resonance increases the energy transferred from ASWs to spin precession within the first 60 ps. As this injected energy overcomes the dissipated energy, the amplitude of spin precession is enhanced, in contrary to the monotonic decaying trend of a typical damped feature of spin precession at other fields. After 60 ps, the injected energy by the strain is insufficient to equilibrate the dissipated energy due to the damping, thus not capable to maintain the high energy state (resonance state). The spin oscillation amplitude decreases, and the typical damped feature appears. This phenomenon indicates that during this first 60-ps time regime, the magnetostrictive field generated by ASWs couples with spins and further enhances the spin precession.

Two TR-MOKE signals, one in resonance (H_{ext} = 21 kOe) and the other one out of magnet-acoustic resonance (H_{ext} = 14 kOe), are chosen to study the coupling between spin precession and ASWs, We find that the frequency of the signal without the magneto-acoustic resonance shows two separated peaks, ~38 GHz for spin precession and ~60 GHz for ASWs, as shown in Fig. 6.3c. However, for the signal with the magneto-acoustic resonance, two frequency peaks are overlapping at ~60 GHz, as plotted in Fig. 6.3d. This suggests that the magneto-acoustic resonance originates from the coupling between strain and spin. To further understand the magnetization dynamics and magnetic resonance resulting from the coupling between strain and spin, the TR-MOKE and TDTR signals of the $[Co(0.8\ nm)/Pd(1.5\ nm)]_{11}$ sample are analyzed in the time domain using Eq. 6.1:

$$V_{in} = A + B\exp(-t/C) + D_1 \sin(2\pi f_1 t + \varphi_1) e^{(-t/\tau_1)} + D_2 \sin(2\pi f_2 t + \varphi_2) e^{(-t/\tau_2)} \ , \qquad 6.1$$

where A, B, and C are related to the thermal background and D, f, φ and τ are the amplitude, frequency, phase offset, and relaxation time respectively. The TDTR data only show one frequency corresponding to the picosecond acoustics (strain) in the system, which is independent of the external field. Fitting the TR-MOKE data shows two distinct frequencies over most of the range: a frequency that depends on H_{ext} following a Kittel dispersion ("spin-like"), and a frequency that is independent of H_{ext} that matches the frequency of the strain captured by TDTR ("strain-like"). Figure 6.3a plots the frequencies of spin precession of the Co/Pd multilayer, which are fitted from the TR-MOKE signal as a function of H_{ext} based on Eq. 6.1. There are 2 modes, the low frequency mode being labeled Mode 1 (open black circles), and the high frequency mode being labeled Mode 2 (open red diamonds).

Because of the weak coupling of these two modes, a gap between the frequency modes opens (as it should for a simple coupled harmonic oscillator). Further information about the coupling between acoustic and magnetic modes has been proposed [188], but a more complete theory for has been proposed by my collaborator Dr. Tao Qu. It introduces coupling coefficient κ of

~(16.5 GHz)^2 that is determined by the magnetostriction coefficient (b_2), magnetic properties and the external field angle (Eq. 6.2) . The frequencies of Modes 1 and 2 display an anti-crossing with a frequency gap Δf, deviating from the original ω_M ($\approx\omega_1$) or ω_{ph} ($\approx\omega_2$).

$$\kappa = \gamma^2 \left(H_{ext} + 2H_{k,eff} \sin^2 \theta_H \right) \frac{\sin(2\theta_H)}{2} \frac{3}{4} \frac{b_2}{M_s} \tag{6.2}$$

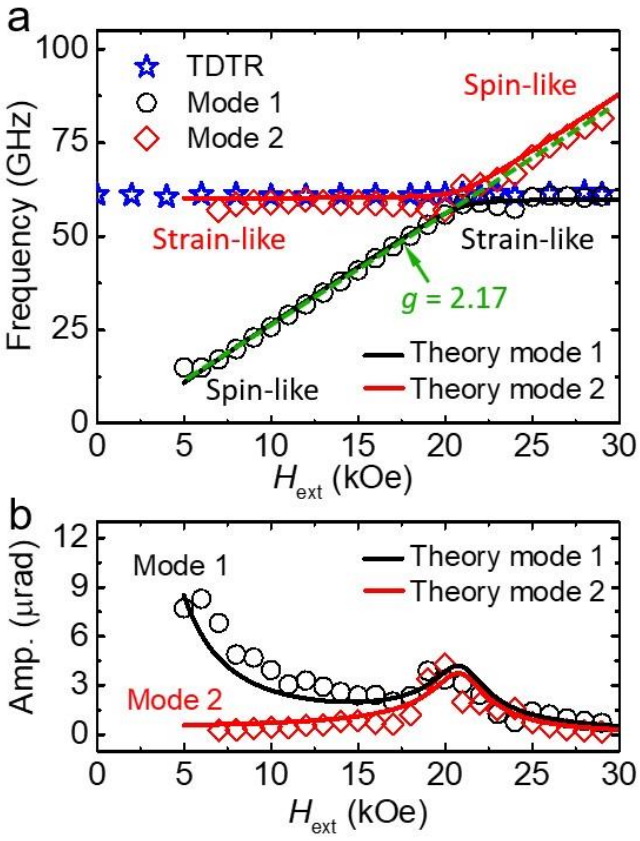

Figure 6.4. (a) The frequency measured in the [Co(0.8 nm)/Pd(1.5 nm)]$_{11}$ multilayer as a function of H_{ext}. Two frequencies of spin precession (Mode 1, open black circles and Mode 2, open red diamonds) are derived by fitting the experimental data of TR-MOKE. The figure also includes the frequency of acoustic waves measured from TDTR (blue stars). The anti-crossing point of Mode 1 and Mode 2 occurs at the resonance field ($H_{ext} \approx 21$ kOe), where the frequencies of Modes 1 and 2 split and open a gap. We assign the strain-like behavior as the field-independent frequencies that are nearly identical to the acoustic wave frequencies from TDTR. The frequency of the spin-like behavior increases linearly with H_{ext}. (b) The individual M_z amplitudes of Modes 1 and 2 as a function of H_{ext} for the [Co(0.8 nm)/Pd(1.5 nm)]$_{11}$ multilayer. There exists an apparent amplification of both modes due to the coupling near the anti-crossing point.

To quantitatively predict the gap Δf, Dr. Qu calculated the two frequencies of Modes 1 and 2 at the resonance point (defined as $\omega_M = \omega_{ph}$ at $H_{ext} \approx 21$ kOe), which gives $\omega_1 = \omega_{ph} - \left(\kappa / 2\omega_{ph}\right)$ and $\omega_2 = \omega_{ph} + \left(\kappa / 2\omega_{ph}\right)$. This yields $\Delta f = 4.6$ GHz, which is consistent with experimental data using no fitting parameters, as shown in Fig. 6.4a. The hybridization regime is defined as the external field at which $\left|\omega_M - \omega_{ph}\right|$ approximates κ / ω_{ph}, leading to a range of 19.7 kOe < H_{ext} < 22.1 kOe. Their amplitudes are comparable and enhanced, compared to those with weak coupling.

6.3 Tuning the Magneto-Acoustic Resonance Point

The coupling between ASWs and spin precession happens when the frequencies of the two modes approach each other. The strain-spin coupling frequency can be tailored *via* tuning either of the two frequencies or both together. Increasing the total thickness of the perpendicular magnetic film will increase the round-trip time of a strain wave package traveling between the top and bottom surface, thus the oscillation frequency of the standing strain wave is decreased. In order to change the dependence between the spin precession frequency and external field, the magnetic anisotropy must be manipulated. In $[Co/Pd]_n$ multilayers, the PMA is dominant and can be tuned by changing the thickness of the Co layers. Therefore, the sample's resonant frequency of strain-spin coupling can be tuned by carefully designing its structure. To test this idea, we have varied the thicknesses and anisotropies of $[Co/Pd]_n$ multilayer structures. The structural parameters and magnetic properties of 5 samples are listed in Table 6.1.

First, we have tested the resonant phenomenon repeatability of samples prepared with the same structure. The reference sample (Sample 2) in Table 6.1 is made with the exact same structure and anisotropy as the primary sample investigated in previous sections (Sample 1), and the same TR-MOKE and TDTR data are obtained under the same conditions. Following this verification, we keep the magnetic anisotropy of the samples (Samples 3, 4 and 5) similar to that of the original sample in the main text, but purely decrease the strain frequency by increasing the thickness of the

total stack. For Samples 3 and 4, only the number of repeating layers (n) are increased, while for Sample 5, the thickness of the Pd layers is also increased.

Table 6.1. Structure and material properties of Si(sub.)/SiO_2(300)/Ta(5)/Pd(5)/[Co(x)/Pd(y)]$_n$/Co(x)/Ta(3)

Name	**Co Thickness (x) [nm]**	**Pd Thickness (y) [nm]**	**# of Repeating Bilayers (n)**	**Thickness of FM [nm]**	**$H_{k,eff}$ [kOe]**
Sample 1 (original)	0.8	1.5	11	25.3	6.2
Sample 2 (control)	0.8	1.5	11	25.3	6.2
Sample 3 (thin)	0.8	1.5	17	39.1	7.0
Sample 4 (medium)	0.8	1.5	24	55.2	8.7
Sample 5 (thick)	0.8	1.8	28	72.8	8.5

The magnetic hysteresis (M-H) loops measured with VSM are plotted in Fig. 6.5. With increased sample thickness, the anisotropy field ($H_{k,eff}$) increases as listed in Table 6.1. Then, TDTR and TR-MOKE measurements (as described in the manuscript) for all the samples are carried out and the obtained frequencies are shown in Fig. 6.6. We can see that as the samples become thicker, the resonance field and frequency are both reduced. The lowest resonance frequency is approximately 27 GHz, obtained from the thickest sample, which is smaller than half of the value from the primary sample in the main text (~ 60 GHz). This suggests the possibility of tuning both the magneto-acoustic resonant frequency and resonant field for the strain-spin coupling through designing the multilayer structure and optimizing the material properties.

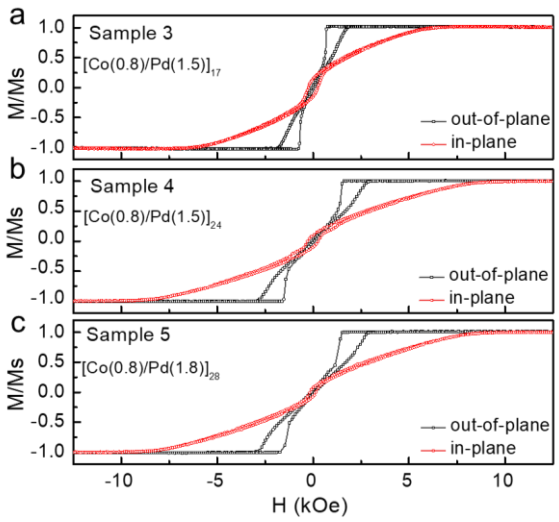

Figure 6.5: The magnetic hysteresis loops for Sample 3, Sample 4, and Sample 5, respectively. The summary of magnetic properties determined from these measurements is shown in Table 6.1.

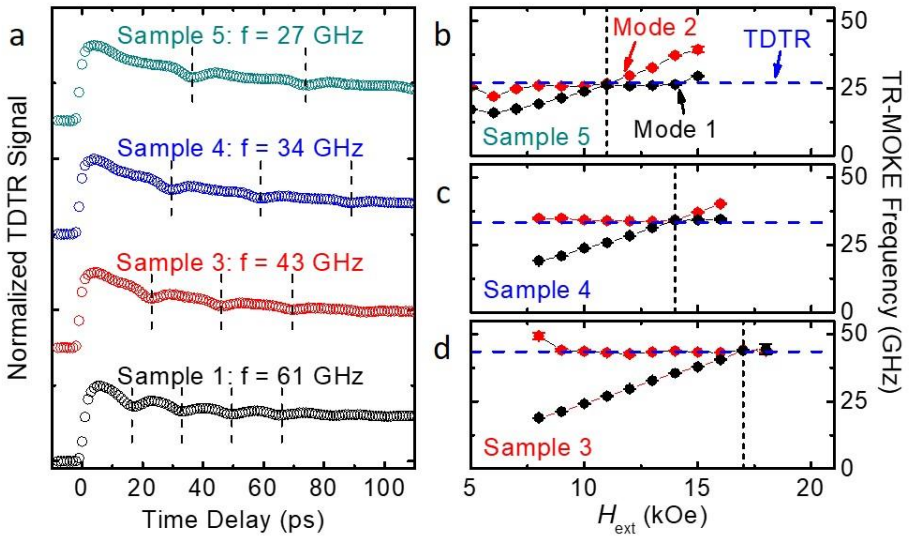

Figure 6.6: The experiment signals and fitting results of TDTR and TR-MOKE measurements. (a) the normalized TDTR signals of the sample in main text (Sample 1) and the three new samples (Samples 3-5), containing picosecond acoustic information resulting from the longitudinal acoustic strains. (b - d) comparisons between the spin precession frequencies from TR-MOKE signals and the strain-wave frequencies from TDTR signals on Sample 5 (thick), Sample 4 (medium), and Sample 3 (thin), respectively. The resonant point of the two curves can be found in all the 3 plots and it can be clearly seen that the magneto-acoustic resonant frequency (anti-crossing region) of the thickest sample is the lowest and reduced to ~27 GHz, which is less than half of the value measured from the sample in main text. The external field of the resonance point is also largely reduced to ~11 kOe for the thickest sample, compared to 21 kOe for the sample in previous sections.

6.4 Understanding Magneto-Acoustic Resonance with Microspin Simulations

To find material and system properties capable of exhibiting a magneto-acoustic resonance, and to provide physical insights into the experimental results, a micromagnetic simulation based on the LLG equation was employed by Dr. Tao Qu and Professor Randall Victora. In order to simulate the coupling between ASWs and spin precession, we introduce a time and special-dependent (position in 3D space indicated by the vector, **r**) magnetostrictive energy term $F_{me}(\mathbf{r},\mathrm{t})$ as a source of the ASWs in the free energy density for the [Co/Pd]$_n$ multilayer systems.

$$\begin{aligned} F_{me}(\mathbf{r},\mathrm{t}) &= \mathrm{b}_1(m_{x'}(\mathbf{r},\mathrm{t})^2 e_{x'x'} + m_{y'}(\mathbf{r},\mathrm{t})^2 e_{y'y'} + m_{z'}(\mathbf{r},\mathrm{t})^2 e_{z'z'}) \\ &+ \mathrm{b}_2(m_{x'}(\mathbf{r},\mathrm{t})m_{y'}(\mathbf{r},\mathrm{t})e_{x'y'} + m_{x'}(\mathbf{r},\mathrm{t})m_{z'}(\mathbf{r},\mathrm{t})e_{x'z'} + m_{y'}(\mathbf{r},\mathrm{t})m_{z'}(\mathbf{r},\mathrm{t})e_{y'z'}) \end{aligned} \quad 6.3$$

The magnetostriction coefficients $b_1 = -16\times10^7$ erg/cm^3 and $b_2 = 26\times10^7$ erg/cm^3 are assumed to match face-centered-cubic Co [90]. The directions x', y', z' represent the crystallographic Cartesian coordinates, in which, the z' axis is along the <001> crystallographic orientation with respect to the coordinate origin for a better description of the magnetostriction effect. The other coordinate we use is the thin film coordinate, represented by x, y, z such that the z-axis is perpendicular to the thin film, corresponding to the crystallographic <111> orientation, for better descriptions of other energy terms in the following section. We only consider the uniformly applied strain tensor $\ddot{e}$ that the whole film is under compression/expansion simultaneously, as measured in the TDTR and TR-MOKE technique. Thus, the spatial dependence of the strain tensor is not involved. In the thin film coordinates, the longitudinal picosecond ASWs are in the perpendicular direction of the thin film, while the transverse ASWs are in the in-plane direction of the thin film. The amplitude of these two acoustic waves obeys the volume conservation.

After obtaining the temporal strain effective perpendicular anisotropy $F_{\mathrm{me}}(\mathbf{r},\mathrm{t})$, the phenomenological expression of the total free energy density

$F(\mathbf{M},\mathbf{r}) = F_{\text{ani}} + F_{\text{me}} + F_{\text{d}} + F_{\text{ex}} + F_{\text{zeeman}}$ for $[\text{Co/Pd}]_n$ multilayers with <111> crystallographic orientation deposited on Si/SiO_2 (300 nm) substrate is:

$$F_{\text{ani}}(\mathbf{r},\text{t}) = K_{\text{u}}(1 - M_z(\mathbf{r})^2), \tag{6.4}$$

$$F_{\text{me}}(\mathbf{r},\text{t}) = \frac{3}{4} b_2 \eta(t) m_Z^2, \tag{6.5}$$

$$F_{\text{d}}(\mathbf{r},\text{t}) = \mathbf{M}(\mathbf{r}) \int \vec{N}(\mathbf{r} - \mathbf{r}') \mathbf{M}(\mathbf{r}') d\mathbf{r}', \tag{6.6}$$

$$F_{\text{ex}}(\mathbf{r},\text{t}) = A(\nabla \mathbf{M}(\mathbf{r}))^2, \tag{6.7}$$

$$F_{\text{zeeman}}(\mathbf{r},\text{t}) = \mathbf{H}_{\text{ext}} \cdot \mathbf{M}(\mathbf{r}), \tag{6.8}$$

where F_{ani}, F_{d}, F_{ex} and F_{zeeman} represent the magnetocrystalline uniaxial anisotropy, magnetostatic energy, exchange energy, and Zeeman energy, respectively. M_{s} and K_{u} can be extracted from the magnetic hysteresis (*M-H*) loops, and A is the exchange constant. $\vec{N}(\mathbf{r} - \mathbf{r}')$ is the magnetostatic tensor. Similar to macrospin simulations, microspin simulations require an effective field, but the microspin time-dependent magnetic field $\mathbf{H}_{\text{eff}}(\mathbf{r},\text{t})$ varies in space and is given by:

$$\mathbf{H}_{\text{eff}}(\mathbf{r},\text{t}) = -\frac{\partial F(\mathbf{r},\text{t})}{\partial \mathbf{M}(\mathbf{r},\text{t})}. \tag{6.9}$$

Finally, the value of Gilbert damping parameter from prediction of $\alpha = 0.02$ is used [189], and γ is the gyromagnetic ratio fitted from TR-MOKE measurement data.

In order to accurately model the magnetization dynamics in the system with micromagnetic simulations, it is important to choose the correct initial condition for the magnetization. This is usually done by choosing an initial condition with a magnetization angle away from equilibrium (an initial cone angle) in the simulation that allows the magnetization to precess. The TR-MOKE

signal can be converted to a precessional cone angle through a straightforward three-step conversion. First, the measured TR-MOKE signal (in μV) is converted to a Kerr angle (in degrees) *via* the detector linear responsivity, based on which, 1 V of TR-MOKE signal in the differential channel of the balanced detector corresponds to 10° of Kerr rotation (θ_k). Next, the change in θ_k with respect to the change in magnetization can be related to the saturation properties *via* $d\theta_k / dM_z \approx \theta_{ks} / M_s$ [187]. Using the literature value of $\theta_{ks} = 0.15°$ for $[Co/Pd]_n$ [187], M_s from VSM measurements, and $d\theta_k$ converted from TR-MOKE signals, we can find dM_z, the change in M_z. Finally, the cone angle is calculated based on the amplitude of dM_z and the equilibrium direction of magnetization (θ). A typical TR-MOKE measurement with a few tens of μV in signal will lead to a cone angle of less than 1°. For this reason, we choose a cone angle of 1° as the initial condition for the magnetization to precess in our the micromagnetic simulations. With this initial cone angle of 1°, we are able to achieve magneto-acoustic resonance with a strain of ~0.1%. This 0.1% amplitude of strain is achievable for ultrafast-laser based dynamic measurements, as a result of thermal expansion launched by laser heating. Considering the relatively small-amplitude strain (0.1%) from optical excitation compared with mechanical strains, we do not anticipate any hysteresis effect to occur in the sample system during TR-MOKE measurements. In addition, we employ volume conservation in simulation, which does not include the hysteresis effect either.

As the energy simulation results show near magneto-acoustic resonance, when the strain amplitude is 0.1% at the beginning 100 ps, the pumped energy dominates and wins over the dissipated energy, exciting the spins to a non-equilibrium state. This energy pumping is efficient, as the excited state is achieved in less than hundreds of picoseconds. For a realistic strain of 0.1% estimated from experimental data, the amplitude of the magnetostrictive anisotropy is 3.9×10^4 erg/cm^3, a significant change in anisotropy when compared with the effective PMA of 9.2×10^5 erg/cm^3. Considering the spin system is essentially a nonlinear system, the magnetostrictive

anisotropy as a driving field can efficiently excite the spins from their equilibrium state and achieve a large oscillation amplitude. The spins precess into a larger oscillation when the energy pumped from strain enhances the system total energy level, overcoming the dissipated energy caused by the damping effect. The theoretical rising time is influenced by the strain amplitude and θ_H.

The simulated rising time in Fig. 6.7b reproduces the TR-MOKE signal in Fig. 6.7a without using fitting parameters for the materials. This confirms the accuracy of our theory. The spins behave damped when the strain decays because the pumped energy, as proportional to the strain, is not sufficient to compensate the dissipated energy. The oscillation amplitude of M_z as a function of H_{ext} shows a peak around the mode-crossing field, and its intensity increases with the increase of the strain, which well matches the experimental results shown in Fig. 6.4b.

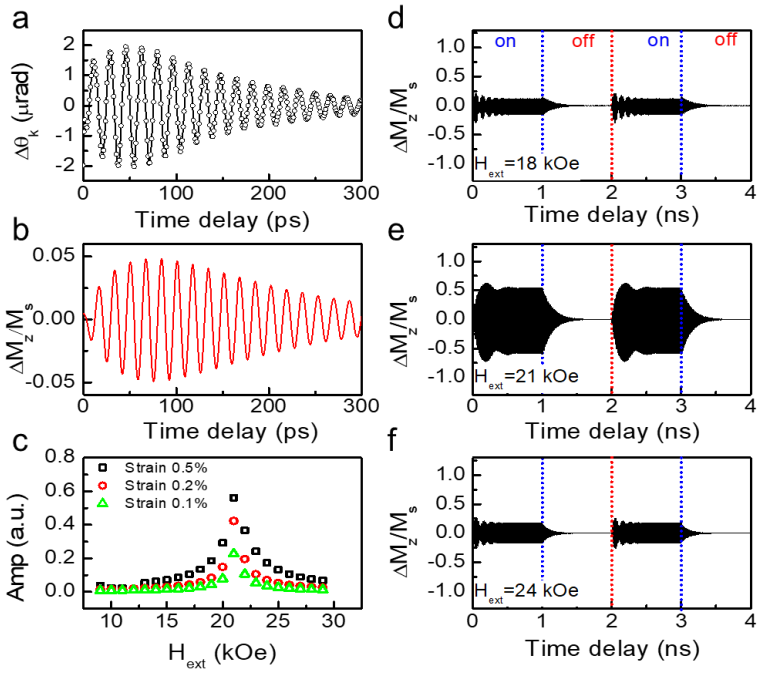

Figure 6.7. (a, b) The experimental and simulated TR-MOKE signal of the $[Co(0.8\ nm)/Pd(1.5\ nm)]_{11}$ multilayer with H_{ext} = 21 kOe, respectively. c) The oscillation amplitude versus H_{ext} for different strain amplitudes (0.1%, 0.2% and 0.5%). The time evolution of the out-of-plane magnetization vs. the time delay when a square strain pulse is applied. The pulse amplitude is 0.5%, the time period is 2.0 ns and the pulse length is 1.0 ns. (d - f) The simulated spin precession coupled with a 0.5% strain pulse under H_{ext} of 18 kOe, 21 kOe and 24 kOe, respectively. When the strain pulse is on, the system gets excited rapidly to an enhanced large angle precession with a rise time of ~100 ps under H_{ext} = 21 kOe not 18 kOe and 24 kOe. When the strain pulse is off, the system at all three H_{ext} values shows relaxation behavior.

To prove ASWs can manipulate the magnetization and further assist the switching in an ultrafast picosecond scale, a strain pulse is applied to the system at three H_{ext} values near the resonance state, as depicted in Figs. 6.7d-f. When the strain pulse is on, the system gets excited rapidly to an enhanced large angle precession with a rise time of ~100 ps. When the strain pulse is off, the system at all three H_{ext} values shows relaxation behaviour and the magnetization is aligned with H_{ext}. This large angle precession caused by the resonance between ASWs and spin precession is maintained steadily for non-decaying strain amplitude. In addition, as the spin dynamics is a nonlinear system, the resonance can happen in a wide field range of several kOe: the required H_{ext} to cause resonance can deviate from H_{ext} that makes the spin precession frequency exactly equal to the strain frequency (Fig. 6.7c). For example, an external magnetic field of H_{ext} = 21 kOe has the maximum precession amplitude, while fields of H_{ext} = 18 kOe or 24 kOe can also excite resonance behavior with relatively smaller precession amplitudes.

6.5 Conclusion

We experimentally detected the ASWs with the response time down to the order of 10 picoseconds in perpendicular magnetic $[Co/Pd]_n$ multilayers *via* a femtosecond laser pulse excitation. Through direct measurements of coherent phonons and magnetization, we observed a 60-GHz magnetic resonance when the frequencies of ASWs and spin precession approach each other. We revealed the physical mechanism of magnetic resonance from the strain-spin interaction from an energy viewpoint. We have shown enhanced energy efficiency by manipulating the spins using the strain. This shows that strain-assisted switching is possible in a perpendicular material. These results could pave a pathway to manipulate the magnetization precession and/or switch the magnetization at an extremely high frequency through strain-spin coupling by optimizing the parameters of multilayer materials.

6.6 Future Project: Harmonics of Strin-Spain Coupling

As part of our study into the thickness dependence of the magneto-acoustic resonance point in these $[Co/Pd]_n$ multilayers, we attempted to understand if TR-MOKE signal could be found far from resonance. We determined the primary strain mode by the interval between pulses (as shown by the dotted lines in Fig. 6.6a), but the FFT of the TDTR signal showed the multiple harmonics that were also in the signal. Figure 6.8 shows the TDTR signal (with and without background) and the FFT of Sample 4. Multiple harmonics are seen in the FFT, especially the second harmonic which has almost the same amplitude as the primary mode.

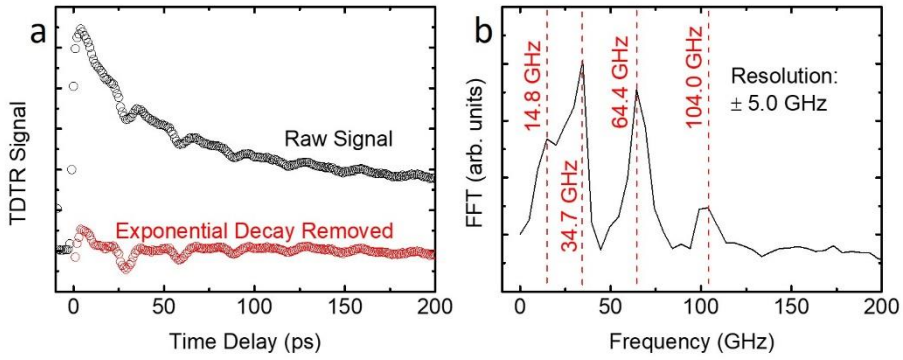

Figure 6.8. TDTR signal showing the picosecond acoustics in Sample 4. (a) the time-domain signal showing the raw TDTR signal as well as a signal where an exponential decay associated with the thermal background has been removed. This allows for an FFT with more noticeable peaks showing the frequencies of the acoustic impulse. (b) the FFT of the TDTR signal showing several peaks. There are two peaks with similar amplitudes: a peak at ~34 GHz associated with the primary strain frequency and another peak at roughly double the frequency, or the 2nd harmonic.

For TR-MOKE measurements, for small values of H_{ext}, the frequencies seen corresponded to the Kittel frequency (spin-like mode) and the primary strain mode (strain-like mode). As the field was increased past this point, it became impossible to fit the signal to a two-frequency model (Eq. 6.1). At H_{ext} = 17 kOe, the FFT of the TR-MOKE data shows that this is due to the prevalence of a third non-negligible frequency mode. This third mode corresponds to the second harmonic in the TDTR signal. The TR-MOKE signal of this field and FFT are shown in Fig. 6.9.

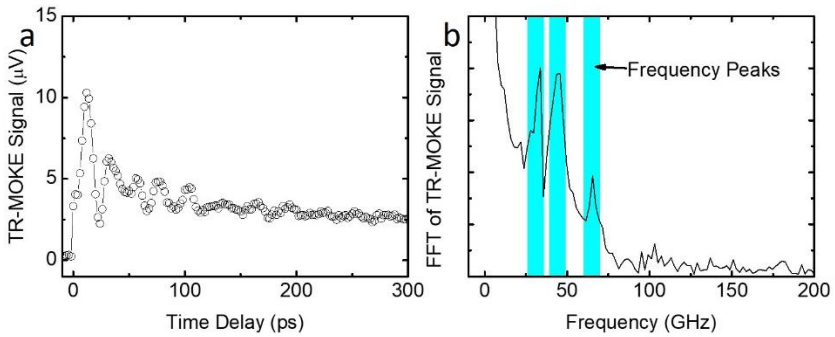

Figure 6.9. TR-MOKE signal showing the spin-strain coupling in Sample 4 at H_{ext} = 17 kOe. (a) the time-domain signal showing the multiple overlapping oscillatory modes. (b) the FFT of the TR-MOKE signal that shows three major peaks in the highlighted regions. The lowest mode is the first harmonic strain mode, the second corresponds to the spin precession, and the third corresponds to the second harmonic.

This point where three modes are present exists in a transition between where the amplitude of the first harmonic becomes negligible compared to the spin-like mode and the second harmonic. At fields above this, when fitting to a two-frequency fit, the strain-like mode becomes the second harmonic. A summary of the frequency fitting is included in Fig. 6.10. Understanding these higher harmonics of strain-spin coupling could provide an efficient method of switching at multiple controllable frequency and field conditions for applications by simply tuning the material stack.

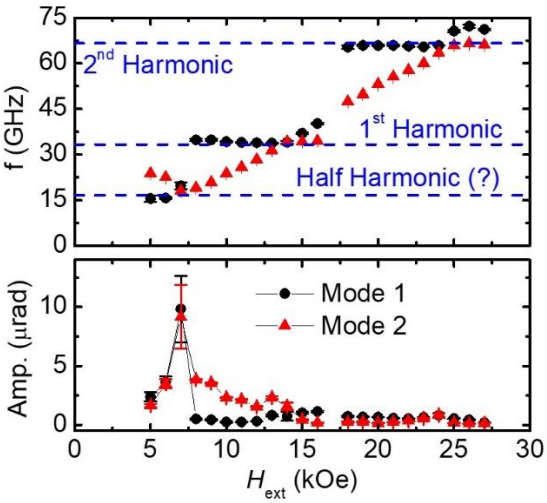

Figure 6.10. Frequency and amplitude fitting from TR-MOKE signals of the multiple frequency modes from Sample 4 of the $[Co/Pd]_n$ multilayers. For fields much lower than $H_{k,eff}$, there appears to be two frequencies corresponding to the spin-like mode and a half harmonic, but it is unclear to us now what is causing this. At 17 kOe there is a transition from one strain-like mode to the second harmonic. The amplitude of the oscillations increases over each magneto-acoustic resonance region.

CHAPTER 7: TEMPERATURE DEPENDENT MAGNETIZATION DYNAMICS IN STT-MRAM MATERIALS

Since the first publication of perpendicular CoFeB magnetic tunnel junctions [107], this material has been the standard for STT-MRAM magnetic layers. This material is easy to grow due to its amorphous nature and has a very low damping in bulk [190,191], but for very thin layers of CoFeB (required for PMA), several issues begin to arise. The low damping that helps to reduce the critical switching current in STT-MRAM begins to rapidly increase as the thickness is reduced due to interfacial effects and spin pumping [55,191]. As an alternative to this material for the next generation of STT-MRAM, $L1_0$-FePd films have recently been shown to be a good alternative because of their low damping and large PMA. As major device components, magnetic tunnel junctions (MTJs) have yet to be proven viable and low in power consumption due to their high switching current resulting from larger damping. Thus, understanding the spin dynamics of PMA materials is critical to engineer and optimize the material properties for better STT-MRAM devices.

The current needed to switch STT-MRAM devices also can have the side-effect of Ohmic heating (the electronic current generates heat due to the resistance of the device). As spintronic devices such as STT-MRAM come closer to widespread adoption, it becomes important to understand some of the additional issues that arise with this excess heat. As shown by studies in HAMR, an increase in temperature can drastically change the magnetic properties of a material [17,192]. For HAMR, this is critical to the function of the device, but in STT-MRAM, a large temperature change will cause a large change in the switching trends. For example, the magnetic damping is predicted to increase rapidly as the temperatures approach the Curie temperature (T_C) of the magnetic material [193,194], which will cause an increase in the critical current. Thus, for STT-RAM applications, it is particularly important to understand the damping mechanism of spin precession as a function of operational temperature.

Although critical, it is non-trivial to establish such an understanding of spin dynamics in PMA materials from direct experimental studies. The major bottleneck stems for the lack of high-fidelity experimental metrology that can directly probe the dynamics of spin precession at elevated temperatures. There have previously been many measurements (both FMR and TR-MOKE) that were conducted at cryogenic temperatures [99,195], which has followed the predicted behavior by Kamberský [43]. Up to this point, the only high-temperature measurement of damping in magnetic materials has been conducted with a chamber FMR (FMR conducted in a resonance chamber with a single frequency) approach, but it was done near the Curie temperature [196]. Here, we aim to measure the trend of damping for a technologically relevant temperature range (up to 150 °C) for two PMA materials of importance: CoFeB and FePd.

7.1 Sample Characterization

For this study, we focus on two material systems. The first is a W-seeded CoFeB stack that was post-annealed at 400 °C, similar to the sample studied previously published and discussed in Chapter 5 [101]. The FePd thin-film sample studied here has a structure of MgO(sub.)/Cr(15 nm)/Ru(4 nm)/FePd(7 nm)/Ta(5 nm) and was provided to us by our collaborators Dr. Delin Zhang and Prof. Jian-Ping Wang and will be discussed more in a future publication. These two material stacks provide a representative sample for two very different magnetic systems. While both of CoFeB and FePd have PMA, this anisotropy comes from two different mechanisms: interfacial anisotropy in the case of CoFeB [145] and magnetocyrstalline anisotropy in the case of $L1_0$ FePd [197]. This leads to two noticeably different behaviors in the VSM data (shown in Fig 7.1) even though the $H_{k,eff}$ for the two materials is comparable (10 kOe and 6.5 kOe from VSM). For CoFeB, the interfacial anisotropy needs a reduced thickness and thus the volume of material is small, so the VSM signal is slightly noisier (especially the in-plane direction) compared to the FePd which has a much larger volume.

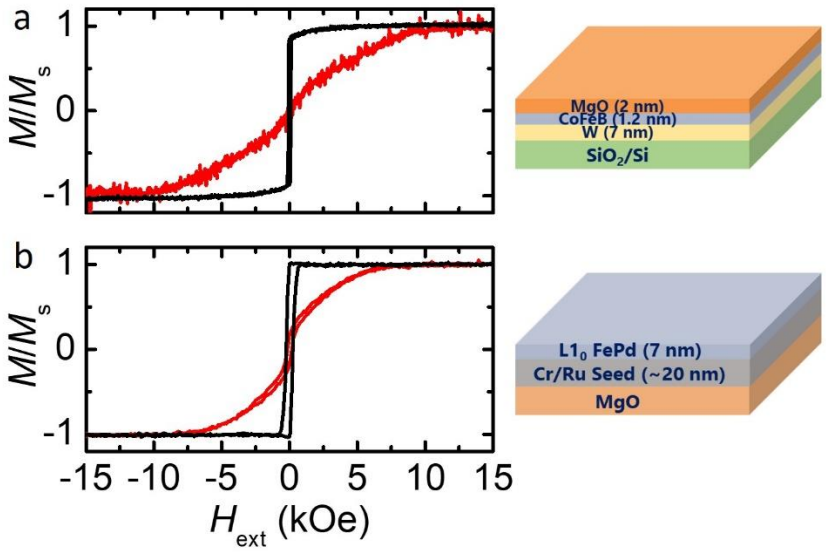

Figure 7.1. VSM and stack diagrams for the two samples studied in this work. (a) The out-of-plane (black curve) and in-plane (red curve) magnetic hysteresis loops for the W/CoFeB/MgO sample post-annealed at 400 °C. (b) The magnetic hysteresis loop for the FePd sample.

While the characterization of the W/CoFeB stack was able to be explained with a first order uniaxial anisotropy, the noticeable in-plane remanence of the FePd sample indicated the possibility of a tilted easy axis of magnetization. We decided to employ a combination of first and second order uniaxial anisotropy ($K_{u,1}$ and $K_{u,2}$ respectively) to try to characterize the hysteresis loop over the entire range. In order to do this, we begin with the assumption that the magnetic free energy of the system is given by the function:

$$F = -\mathbf{M}\cdot\mathbf{H}_{ext} - 2\pi M_s^2\cos^2(\theta) - \left(K_{u,1} + 2K_{u,2}\right)\cos^2(\theta) - K_{u,2}\cos^4(\theta). \qquad (7.1)$$

This free energy will allow for an equilibrium angle as a function of field that has been discussed previously [48,106]:

$$H_{ext}\sin(\theta_H - \theta) - \frac{1}{2}\left(\frac{2K_{u,1}}{M_s} + \frac{4K_{u,2}}{M_s} - 4\pi M_s\right)\sin(2\theta) + \frac{1}{2}\left(\frac{4K_{u,2}}{M_s}\right)\cos^2(\theta)\sin(2\theta) = 0. \quad (7.2)$$

This equilibrium (minimum energy condition) allows for an "easy cone" of magnetization, so called because the low energy state without external field is uniform across azimuthal directions and tilted from the *z*-axis [198,199]. This leads to the magnetization having a remanence in both out-of-plane and in-plane directions, which was a possible explanation for the magnetic state in Figure 7.1b.

7.2 TR-MOKE Experimental Results

To conduct the TR-MOKE measurements at elevated temperatures, we needed to create a home-built heating stage (the first of its kind). This heating stage needed to be able to provide heat to the sample at a controlled temperature, be non-magnetic, and needed to fit between the electromagnetic poles (a space of <10 mm). With the help of both Haidong Ma (visiting scholar in our lab) and Daehyun Kim (undergraduate student in our lab), we settled on a basic design of using a PID controlled heater equipped with a type-E thermocouple (non-magnetic). The heater was attached to an insulated copper rod and the sample was placed on the end of an extended surface with silver paint. Prior to a measurement, the temperature was set, and a steady state temperature was reached and recorded. The measurements were conducted from high fields to low fields for two reasons: 1) to avoid the possibility of the magnet overheating at high fields and 2) to alleviate the impacts of the in-plane hysteresis by ensuring the magnet is saturated. For this setup, we kept the magnetic samples exposed to ambient conditions due to the space limitations. The remaining aspects of this experiment are very similar to those described in Chapters 3 and 5.

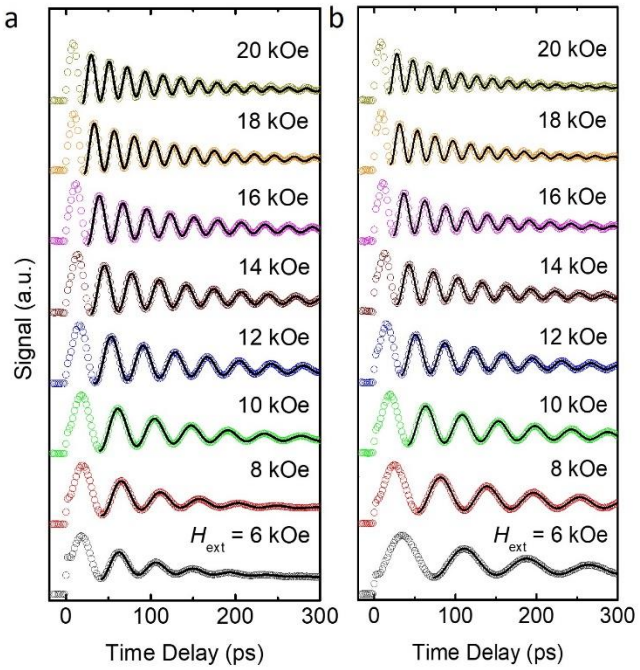

Figure 7.2. Raw TR-MOKE data for the W/CoFeB at (a) 25 °C and (b) 150 °C (open symbols). The signals are provided at multiple fields with θ_H = 82°. The solid lines indicate the fitting of the signal to a decaying sinusoid to extract the frequency and relaxation time.

The raw signal showed clear signs of oscillations even at high fields and high temperatures as indicated by Fig. 7.2. For each temperature, many measurements were necessary to so that a fit of relaxation time and frequency to extract $H_{k,eff}$ and α. A field scan was taken for each temperature (25, 50, 75, 100, 125, and 150 °C). The measurements were conducted from low temperature to high temperature on a single sample in a single continuous measurement.

7.3 Analysis of Temperature-Dependent Properties

After the extraction of the raw data, further analysis was needed in order to extract the temperature dependent properties. The data is fit to a decaying sinusoid:

$$S(t) = A + B\exp(-t/C) + D\sin(2\pi ft + \varphi)\exp(-t/\tau). \tag{7.3}$$

Once the frequency and relaxation time are extracted for a given temperature, the frequency and relaxation rate can be fit. For the frequency fitting, only high-field ($H_{ext} > H_{k,eff}$) data is used and we use equations similar to those described previously to account for the possibility of a 2nd order uniaxial anisotropy ($K_{u,2}$) [48]:

$$f = \frac{\gamma}{2\pi}\sqrt{H_1 H_2}\,, \tag{7.4}$$

$$H_1 = H_{ext}\cos(\theta_H - \theta) + H_{k,1}\cos(2\theta) - \frac{1}{2}H_{k,2}\left(\cos(2\theta) + \cos(4\theta)\right), \tag{7.5}$$

$$H_2 = H_{ext}\cos(\theta_H - \theta) + H_{k,1}\cos^2(\theta) - H_{k,2}\cos^4(\theta), \tag{7.6}$$

$$H_{ext}\sin(\theta_H - \theta) - \frac{1}{2}H_{k,1}\sin(2\theta) + \frac{1}{2}H_{k,2}\cos^2(\theta)\sin(2\theta) = 0\,, \tag{7.7}$$

$$H_{k,1} = \frac{2K_{u,1}}{M_s} - 4\pi M_s + H_{k,2}\,, \tag{7.8}$$

$$H_{k,2} = \frac{4K_{u,2}}{M_s}\,. \tag{7.9}$$

The fitting equation for relaxation rate is also expanded to incorporate an additional form of inhomogeneous broadening (due to a distribution of easy axes in a small angle from the z-axis):

$$\frac{1}{\tau} = \frac{1}{2}\left[\alpha\gamma\left(H_1 + H_2\right) + \frac{\partial\omega}{\partial H_{k,1}}\Delta H_k + \frac{\partial\omega}{\partial\theta_H}\Delta\theta_H\right]. \tag{7.10}$$

The data of frequency and relaxation rate from measurements are fit to equations 7.4 and 7.10 in order to extract 4 key parameters: $H_{k,eff}$, α, $\Delta H_{k,1}$, and $\Delta\theta_H$. A summary of these data is provided in Fig. 7.3. The secondary anisotropy in this case is found to be negligible and is not plotted.

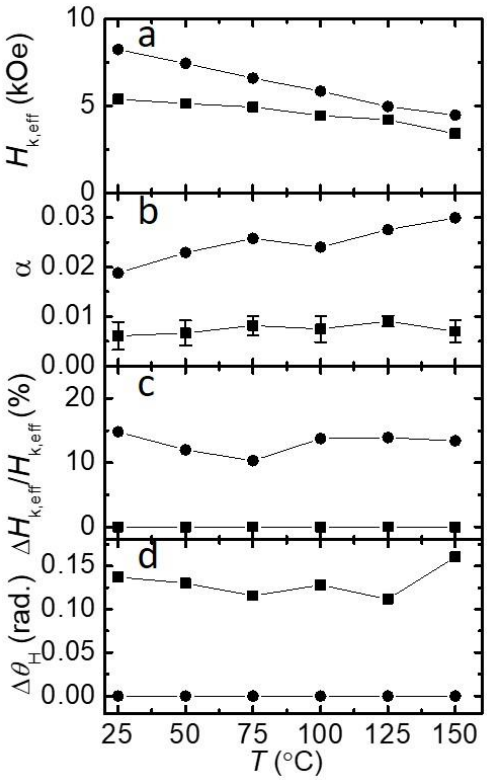

Figure 7.3. Summary of the extracted magnetic properties from TR-MOKE measurements. (a) $H_{k,eff}$, (b) intrinsic damping, (c) inhomogeneous broadening due to a distribution in $H_{k,eff}$, and (d) inhomogeneous broadening due to a distribution of easy axes. The square symbols show the results for FePd and the circles show CoFeB. The FePd contribution in (c) and the CoFeB in (d) are negligible so appear along the *x*-axis.

The results for the two samples show very similar trends with increasing temperatures. As expected, anisotropy should decrease with increasing temperature, but the decrease in anisotropy for the CoFeB sample is much more noticeable (almost 50% over this temperature range). This could be an indication that the Curie temperature is much lower for this material. While the Curie temperature of bulk CoFeB is predicted to be higher than FePd (~1000 K compared to ~750 K) [200,201], for thin film materials, the Curie temperature could be lower due to interdiffusion. This is more in line with the large change we see in anisotropy that is measured for CoFeB here. Because the FePd T_C is large compared to the measurement temperature, the change is small, but it is still almost a 33% change. While a monotonically decreasing trend is apparent, it is unclear without further measurements whether it should be a linearly decreasing trend.

The temperature-dependent damping has the opposite trend. For increasing temperatures, the damping trends to increase, which was expected based on predictions for damping for other materials with high spin-orbit coupling [46]. Again here, the CoFeB shows a more drastic change in damping over this temperature range (~50%) than FePd (~33%). This is another indication that the T_C for this material is much lower than the FePd because the increase in damping should accelerate as the temperatures continue to increase. For the inhomogeneous broadening mechanisms, each material has a dominant for of inhomogeneity and the other is negligible. For CoFeB, the dominant form is the distribution in $H_{k,eff}$, which is most likely due to small thickness differences throughout the sampling area. For FePd, the anisotropy is magnetocyrstalline, so it doesn't depend as much on the thickness, so $H_{k,eff}$ is more uniform, but the cubic ordering of the atoms in the material could result in a preferential direction (a "cubic anisotropy") that will be averaged over many grains and result in a distribution of easy axes. While both cases show that the relative impacts of inhomogeneous broadening do not change with temperature, further research is required to determine if this trend continues to higher temperatures.

7.4 Conclusion

While STT-MRAM products are already being made into products, for widespread adoption, the impact of environmental temperature on operation is crucial to understand. For the two products CoFeB and FePd, these experiments show that the anisotropy and relaxation change dramatically even over a relatively narrow temperature range of room temperature to 150 °C. While the W/CoFeB sample post-annealed at 400 °C has a higher anisotropy than the FePd sample, the damping is larger, and the change of both anisotropy and damping is more drastic over this temperature rise (a decrease in anisotropy of nearly 50% and an increase in damping of almost 50%). This seems to indicate a lower Curie temperature for W/CoFeB material. Further measurements of M_s and $H_{k,eff}$ as a function of temperature with VSM measurements should be able

to reveal the relationship. More temperatures approaching T_C with TR-MOKE would also be of interest for future measurements. Additionally, a better understanding of the inhomogeneous broadening mechanisms with temperature could help with understanding the relaxation in devices at high operating temperatures.

CHAPTER 8: HIGH TEMPERATURE MEASUREMENTS OF IRON-PALLADIUM

Over a decade since the initial concept was widely accepted as the future of recording [17,202], heat-assisted magnetic recording (HAMR) is now on the verge of being released in the commercial space. This technology represents the next generation of magnetic recording and could theoretically reach densities on the order of 4 Tbit/in^2 in the coming years [203,204]. One of the benefits to come from this technology is the increased theoretical understanding of the temperature dependence of magnetization dynamics for various materials. To understand the temperature dependence of magnetic anisotropy and damping, micromagnetic simulations [193,205], stochastic simulations [206], and the Landau-Lifshitz-Bloch (LLB) model [194,207-209] have all been utilized. While temperature dependence of damping in low-temperatures has been shown to agree with theory [195], experimental verification of these models at high temperatures is lacking. In this chapter, TR-MOKE measurements of magnetic properties and magnetization dynamics of FePd thin films will be discussed.

8.1 Initial Characterization Attempts on HAMR Media Materials

The initial motivation for this research was for the direct understanding of high temperature damping in granular FePt samples meant for HAMR media. As such, we attempted to measure a sample provided to us by collaborators at NIMS in Japan. The sample they provided had similar properties to the sample that they had previously published [210,211]. This sample had a room temperature coercivity of several tens of kOe, much higher than the H_{ext} available in our TR-MOKE setup. Because of this, the magnetization would be pointed almost completely out-of-plane even with 23 kOe (the maximum available field at the time) at room temperature resulting in a negligible TR-MOKE signal ($\Delta M_z/M_s \approx 0$). To capture a MOKE signal, we heated the material using a home-built heating stage at temperatures up to 400 °C to reduce the anisotropy and thus create a MOKE signal.

The resulting signal showed very little sign of oscillation but provided us with enough data to prove that we could measure a TR-MOKE signal in these materials and also extract an effective damping. Our first indication that we were measuring a magnetic signal is shown in Fig 8.1a. The TR-MOKE signal measured at or below 370 °C (just below the Curie temperature) showed a very small sign of oscillation (shown by the initial peak at ~10 ps and subsequent valley at ~20 ps). At temperatures above the Curie temperature (indicated by the blue curve fits and blue arrow in Fig. 8.1a), this oscillation goes away. To further show that this is a ferromagnetic resonance feature, we needed to show that the frequency would change with external field. In Fig. 8.1b, the temperature was held constant and H_{ext} was varied. While again the oscillations are weak, a resonance frequency and damping (plotted in Figs. 8.1c and 8.1d respectively) show the correct trend of a material with an $H_{k,eff}$ = 9.9 kOe.

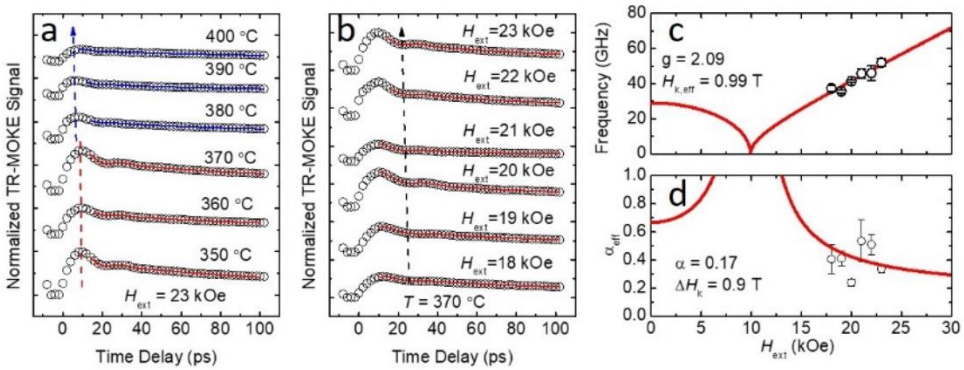

Figure 8.1. TR-MOKE results of an FePt sample from NIMS for (a) constant field changing temperature, (b) constant temperature changing field. The summary of the measurement with constant temperature and changing field is shown in (c) resonance frequency and (d) effective damping.

The lack of oscillations in the measurement results of this sample can be explained by the large effective damping. Not only is the damping high at high temperatures [193], but the effective damping largely increases as well in this patterned media. The inhomogeneous broadening in this media by propagating the variation in the T_C (σT_C) into a variation in the effective anisotropy field ($H_{k,eff}$). Assuming a 3% σT_C, we can estimate the standard deviation in $H_{k,eff}$ at 370 °C to be 0.39 T.

A visualization of this process is shown in Fig. 8.2 and a derivation is expressed as Eq. 8.1. This is a simplification based on the assumption that the anisotropy depends linearly on temperature.

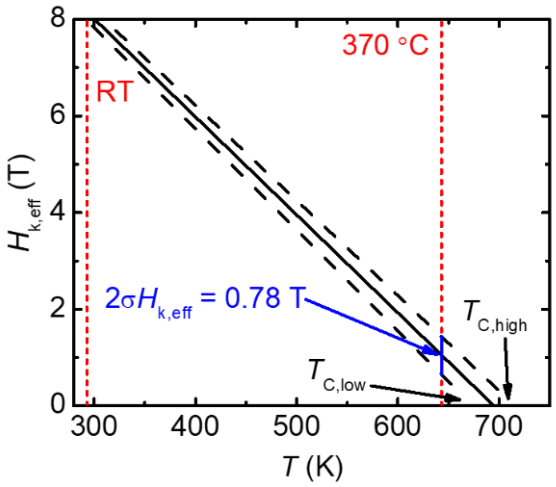

Figure 8.2. The relationship between a variation in T_C and the $H_{k,eff}$. At high temperature (370 °C), a 3% σT_C causes a $\sigma H_{k,eff}$ of ± 0.39 T.

$$\sigma H_{k,eff} = \frac{\partial H_{k,eff}}{\partial T_C} \sigma T_C \qquad 8.1$$

Treating the distribution of $H_{k,eff}$ as a normal distribution with a center determined by the measured resonance frequency of spin precession at 370 °C, the FWHM of the $H_{k,eff}$ distribution can then be propagated into the relaxation time. Due to the distribution in resonance frequencies caused by the variation in $H_{k,eff}$, the measured curve appears to have a higher damping than it would if the anisotropy was uniform. This inhomogeneous broadening is visualized by Fig. 2.7 by a set of weighted precessions (2.7a, found through the LLG equation), which are then summed together to produce the signal we would expect to see from measurements (2.7b). The weighting factor for producing plots 2.7b is determined by calculating the amplitude of a normalized gaussian distribution at the specified distance from the center $H_{k,eff}$ with the variance found previously. By holding the inhomogeneous broadening as a known constant (estimated from the LLG model with

the $H_{k,eff}$ distribution induced from the T_C variation), the damping can then be fit from the measured relaxation time. This results in a damping of 0.17 at 370 °C.

Based on the discoveries from this sample, we attempted to push forward and measure a new FePt sample at a larger temperature range. The properties of a similar sample were previously published [196,212]. For this sample, the goal was not to extract damping (due to the large inhomogeneous broadening), but to see if the temperature dependent anisotropy could be extracted at multiple temperatures. A summary of the results is shown in Fig. 8.4. The frequency as a function of field is shown for three temperatures in 8.3a. Fitting these curves to a Kittel dispersion results in an extracted $H_{k,eff}$. The extracted $H_{k,eff}$ is shown in Fig. 8.3b as filled symbols compared to the open symbols which represent the published data (from AC Susceptibility measurements) [212].

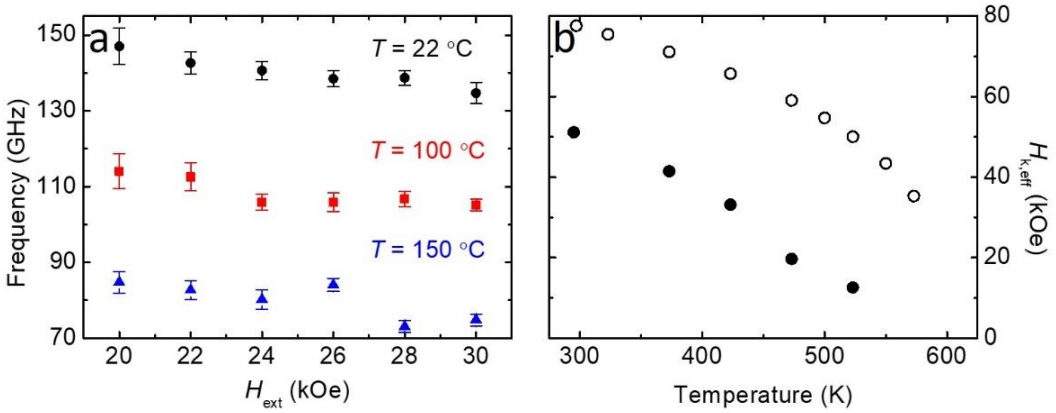

Figure 8.3. Results of an FePt sample measured with TR-MOKE. (a) The fitted frequency from TR-MOKE measurements at several temperatures. (b) The extracted $H_{k,eff}$ from fitting the frequency curves. The filled symbols represent the TR-MOKE values while the open symbols show published values for this sample.

Figure 8.3b shows that the TR-MOKE values for $H_{k,eff}$ are significantly lower than other measurements provide. While the decreasing trend appears to match published data, TR-MOKE shows values that are ~30 kOe less than expected. Because of the working mechanism of TR-MOKE (a pulse of light heats up the sample to begin precession) another way to understand this result is that TR-MOKE data is actually ~200 K higher than published data (e.g., the real

temperature of the 300 K data point is 500 K). This would be due to the thick metallic heat sink layer (deposited underneath the magnetic layer) absorbing heat and thus causing the temperature to be higher than predicted. With a published value of thermal conductivity [213,214], an approximated sample stack (the exact materials and thicknesses were not provided), and laser properties (power P_{laser} and spot size w_0), the steady-state temperature rise can be estimated by [215]:

$$\Delta T_{\text{ssh}} = \frac{P_{\text{laser}}}{2\sqrt{\pi} w_0 \Lambda} \ . \tag{8.2}$$

This steady state temperature rise causes many complications in the accurate measurement of temperature dependent damping. The combination of this temperature rise, the large intrinsic damping, the large inhomogeneous broadening, and the extremely high anisotropy of this sample, we determined that it would be difficult to extract noticeable precessions with our current setup at a large range of temperatures. For our study of temperature dependent magnetization dynamics, we decided to make a sample that had high anisotropy, was not a media sample (lower inhomogeneous broadening), had lower intrinsic damping, had a similar T_C, and was grown directly on a dielectric substrate (to avoid steady-state heating effects).

8.2 FePd Sample Characterization

Due to the high intrinsic damping and the large inhomogeneous broadening, we wanted to study a material with a similar high spin-orbit coupling, high magnetic anisotropy, and $L1_0$ atomic order, so we settled on FePd. The sample chosen for this study was an FePd sample grown directly on an MgO (001) substrate with a modified Molecular Beam Epitaxy (MBE) sputtering system with an ultra-high vacuum ($<3\times10^{-8}$ Torr). The sample stack is MgO(sub.)/FePd(7.5 nm)/Ta(3 nm) and was grown by our collaborators Delin Zhang and Deyuan Lyu in Prof. Jian-Ping Wang's lab. We chose FePd because of the similar $L1_0$ structure to FePt [216], relatively large anisotropy [217],

and its low damping [45,46,48]. We have an additional advantage in that it is a continuous film sample, so the impact of a large inhomogeneous broadening due to the granular structure of our FePt samples can be diminished. The single crystalline MgO substrate should also reduce the impacts of the steady state temperature rise due to its dielectric optical properties and large thermal conductivity [218].

The magnetic properties were characterized with the VSM attachment of a PPMS system. In addition to the standard magnetic hysteresis characterization, we also measured the T_C of this sample by using an oven attachment to the VSM system. This allowed us to measure the magnetic moment as a function of temperature (see Section 3.3.2 for more details). The hysteresis in Fig. 8.4a shows an $H_{k,eff}$ of ~15 kOe at room temperature with a noticeable in-plane remanence, which could be due to some amount of disorder in the magnetic film. The temperature dependent magnetization shows a T_C of approximately 740 K, similar to the measured FePt. We will use this knowledge to better understand the temperature dependent trends of anisotropy and damping from TR-MOKE.

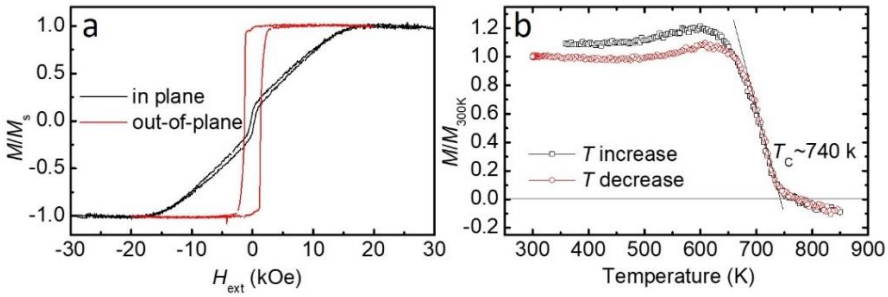

Figure 8.4. Magnetic characterization of the FePd sample. (a) The magnetic hysteresis plot showing the magnetization as a function of in-plane and out-of-plane external field. (b) The temperature dependent magnetization plot showing a Curie temperature of ~740 K.

8.3 Temperature Dependent TR-MOKE Measurements

To characterize the magnetic properties of α and $H_{k,eff}$ as a function of temperature, we use a home-built heating stage that is capable of heating the sample up to the Curie temperature. A description of the heating stage is included in Chapter 7. Just like in the previous chapter, the

measurements were conducted from low temperature to high temperature (to avoid the possibility of sample degradation due to temperature) and high external field to low. The TR-MOKE signal showed clear precession even at high fields and high temperatures as shown by Fig. 8.5a and 8.5b. The extracted frequency as a function of field and temperature is given in Fig. 8.5c at temperatures from near room temperature (299 K) to the highest temperature that provided a clean precessional signal (594 K). For each temperature, the field was brought to 27 kOe and reduced to 3 kOe (the lowest field with a still measurable precession signal at near room temperature). As temperature increases, the anisotropy should decrease which should result in the minimum frequency for each temperature moving to lower fields. In other words, the linear high branch portion should shift up for increasing temperatures and the low branch should down for increasing temperatures.

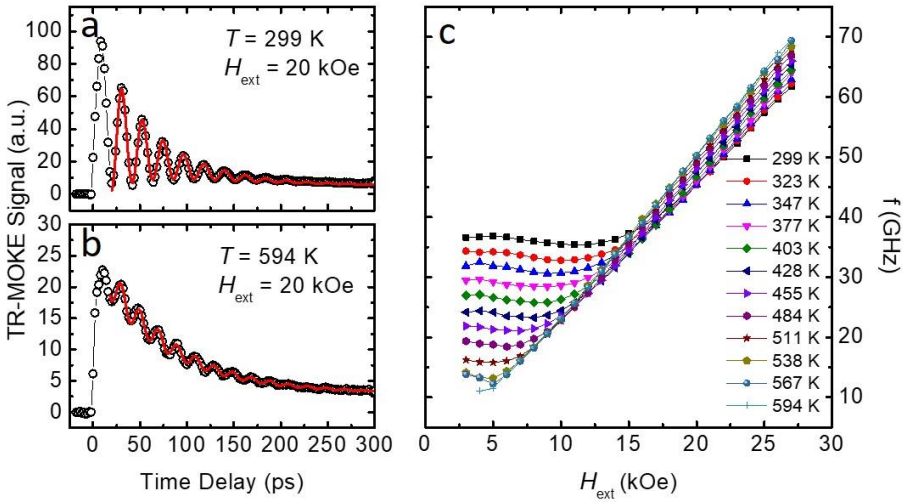

Figure 8.5. TR-MOKE results for the FePd sample. Raw TR-MOKE signal at an external field of 20 kOe and θ_H = 80° at an environmental temperature of (a) 299 K and (b) 594 K. (c) A summary of the frequency extracted from the raw signal as a function of H_{ext} and temperature.

To show the impact that temperature has on anisotropy for this sample, the TR-MOKE frequency data is fit to a Smit-Suhl model to extract the $H_{k,eff}$ as summarized in Fig. 8.6a. As expected, the anisotropy goes down with increasing temperature. The decreasing trend in effective damping appears to go against the predicted trend of increased damping at higher temperatures, but

because this is the effective damping, the impact of inhomogeneous broadening also needs to be considered. This means that the damping will approach the real value as the external field becomes much higher than $H_{k,eff}$. In other words, for a constant field, as the temperature goes up, the effective damping is expected to go down (if the intrinsic damping does not overcome the inhomogeneous relaxation effects).

The trends in $H_{k,eff}$ appears to be consistent until ~525 K. Similarly, the effective damping shows a monotonically decreasing trend with temperature until this point in Fig. 8.6b. This could be due to sample degradation or diffusion due to the prolonged exposure to open atmosphere at high temperatures. Because of the high temperatures, this could also be due to a breakdown in the assumptions made in the LLG equation that this analysis is based on. At this point in time, it becomes critical to research the effects of temperature on magnetization dynamics without assumptions of a constant saturation magnetization.

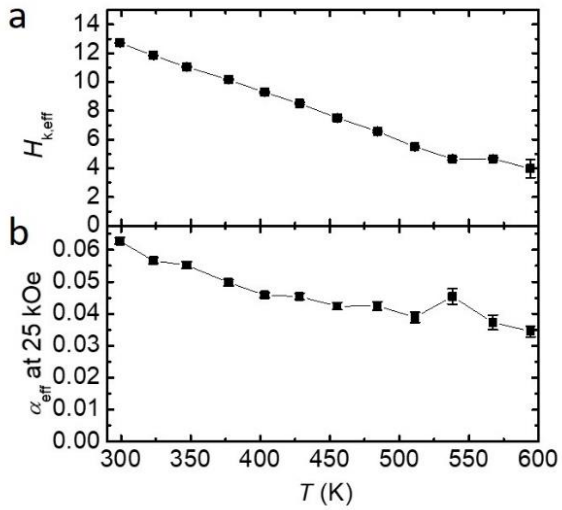

Figure 8.6. Summary of TR-MOKE results for (a) $H_{k,eff}$ and (b) the effective damping at H_{ext} = 25 kOe.

8.4 Landau-Lifshitz-Bloch Equation

The Landau-Lifshitz-Gilbert equation is made with the assumption that the magnetization remains constant throughout the entire dynamic process. The working mechanism behind TR-MOKE requires a temperature rise to initiate magnetization dynamics, so the LLG is an imperfect solution to describe the dynamics. Even so, this equation is often used to describe TR-MOKE dynamics because the temperature rise only causes a small change in M_s during the measurement. This causes the LLG to provide a good tool to analyze data far from T_C, but for this measurement, the temperature is approaching T_C meaning that the change in M_s can no longer assumed to be small. For future measurements of samples approaching T_C, I propose the application of the Landau-Lifshitz-Bloch (LLB) equation for analysis. This equation (Eq. 8.3) incorporates two forms of damping: transverse damping (typical LLB damping, $\alpha_\perp$) and a longitudinal damping (due to a changing M_s, $\alpha_{||}$). While this will complicate the extraction of damping and anisotropy, it will provide more accurate results.

$$\dot{\mathbf{m}} = -\gamma \mathbf{m} \times \mathbf{H}_{\text{eff}} + \frac{\alpha_{||}\gamma}{m^2}\left(\mathbf{m} \cdot \mathbf{H}_{\text{eff}}\right)\mathbf{m} - \frac{\alpha_{\perp}\gamma}{m^2}\mathbf{m} \times \left(\mathbf{m} \times \mathbf{H}_{\text{eff}}\right) \tag{8.3}$$

More information about this equation can be found in Appendix D, but one key result for damping is that it predicts a temperature dependent damping. By assuming that the temperature change during the measurement is small, the result transverse (or LLG) damping should be given by:

$$\alpha_{\text{meas}} = \frac{M_0}{M_s}\left(1 - \frac{T}{3T_C}\right)\alpha_0 , \tag{8.4}$$

where the subscript “0” indicates the values at 0 K. This seems to indicate that the temperature dependent damping should be able to be predicted by temperature if the magnetization and initial

damping are known. This is at least a first order confirmation of the trends expected in measurements.

If the assumption of a small temperature change is not made, the LLB equation requires numerical simulation. For a test of this equation, the LLB prediction is compared to measured TR-MOKE values for a CoFeB sample. As shown by Figure 8.7, the agreement between the two is very good to the point where the LLB simulation even correctly predicts the thermal background even without an accurate measurement of the thermal conductivity. The main difference is in the relaxation. The LLB simulation is macrospin and cannot account for the relaxation caused by inhomogeneous broadening. Based on these high-level applications of the LLB, this model should be used to understand temperature dependent magnetization for further studies.

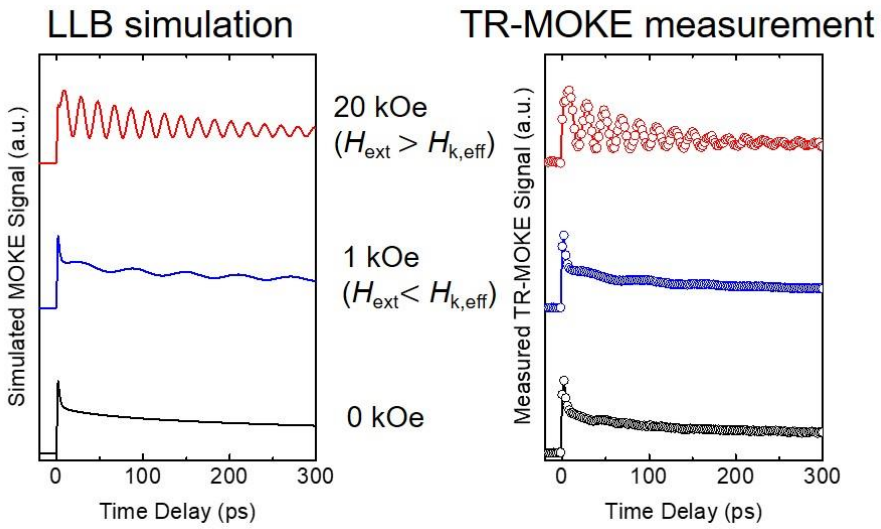

Figure 8.7. Comparison of LLB simulation to TR-MOKE measurements for a CoFeB sample at room temperature. The values used for the LLB simulation are $K_{u,0}$ = 10 Merg/cc, $M_{s,0}$ = 1000 emu/cc θ_H = 78°, α_0 = 0.016, T_C = 600 K, and ΔT = 50 K using mean field theory, the anisotropy dependence published by Myrasov et al. [219], and the temperature profile predicted by Cahill [215].

8.5 Conclusion

Through this study, we have shown the first study of a large range of magnetization dynamics as a function of temperature approaching the Curie temperature. Through initial measurements on HAMR media samples with granular structures, we found that the large anisotropy and inhomogeneous broadening led to a complex data reduction. The heat absorbing layers in one sample also led to a large temperature rise in TR-MOKE measurements. To get around this, we study a FePd sample grown directly on single crystalline MgO. It was found that, for this FePd sample, the $H_{k,eff}$ has an almost linear decrease with increasing temperatures. This leads to a series of frequency plots that shift to lower frequencies at lower fields and higher frequencies at higher fields. We also find that this leads to a decreasing trend in effective damping for increasing temperatures. As the project continues to develop, further research will have to look into data reduction using the LLB equation to better understand the influence of the TR-MOKE pump heating on high-temperature measurements.

CHAPTER 9: PRELIMINARY STUDY OF ANTIFERROMAGNETIC COUPLING IN SYNTHETIC ANTIFERROMAGNETS (SAF) FILMS

The critical switching current in STT-MRAM is dependent on many magnetic properties, such as the damping (as previously discussed). Decreasing the damping, anisotropy, and saturation magnetization are all helpful to reduce the critical switching current. This means that by using a ferromagnetic free layer with a low M_s, the critical switching current can be greatly reduced. Along this line, free layers made with synthetic antiferromagnets (SAF) films theoretically should have a very small critical switching current [220-222]. Our collaborators have already shown the viability of devices made with SAF free layers [222], and others have shown the dynamics in similar antiferromagnetically-coupled stacks [223,224], but little is known about the damping process in these devices. Recently, we have attempted to measure the magnetization dynamics of a SAF structure, and we can see two simultaneous precessional modes corresponding to the coupled magnetic system.

The concept of a coupled system of two or more magnetic volumes was originally used to predict the resonance behavior of nearby domains. Building from this theory, discussions of ferromagnetic resonance in coupled films have focused primarily on the frequency of in-plane films or a system of a perpendicular film coupled to a film with no anisotropy. These coupled systems add additional complexity to extracting damping from resonance data. Our focus here will be on perpendicular-SAF structures which should be able to be easily integrated into existing perpendicular STT-RAM structures. Because the damping in STT-RAM is also crucial in determining the critical switching current, we would need to expand existing ferromagnetic resonance models to also provide a value of the relaxation rate of the two modes (and thus the damping in both films) simultaneously.

9.1 Sample Deposition and Magnetic Characterization

The sample of interest in this chapter is similar to the SAF free layer that has been published by Zhang et. al [222]. The sample is made via molecular beam epitaxy (MBE) of the SAF structure (FePd and Ru layers) followed by a sputtering of the top Ta layer for an overall structure of MgO(sub.)/Cr(15 nm)/Pt(3 nm)/FePd(3 nm)/Ru (1.1 nm)/FePd(3 nm)/Ta (5 nm). The two FePd magnetic layers are antiferromagnetically coupled through the Ruderman-Kittel-Kasuya-Yosida (RKKY) effect where the coupling oscillates between negative coupling (antiferromagnetic, the two magnetizations prefer to be anti-parallel) and positive coupling (ferromagnetic, the magnetizations prefer to be parallel) [225-227]. The thin layer of Ru (a material that fascillitates RKKY coupling) should lead to a strong negative coupling [228]. Through this antiferromagnetic coupling, the net magnetization of the two layers should cancel without an external field in an ideal situation. This can be tested through a VSM measurement, which is summarized in Fig. 9.1.

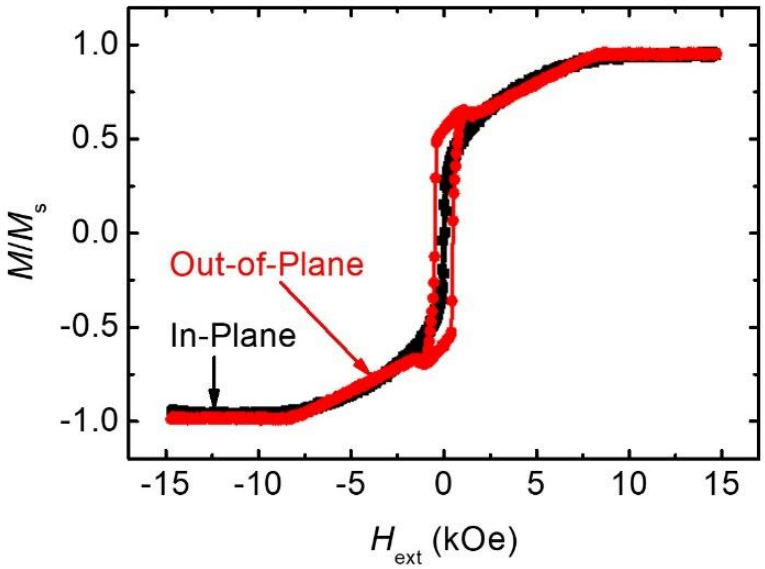

Figure 9.1. The magnetization hysteresis plot for a FePd/Ru/FePd system that is studied in this chapter. This sample is similar to a sample that has been previously published [222].

From this figure, the sample is not perfectly antiferromagnetically coupled by the large out-of-plane remanence. The partial antiferromagnetic coupling is still useful to reduce the energy required for switching by providing an initial "tilted" magnetization case for at least one of the layers in the coupled system. Typically to determine the strength of the coupling from a hysteresis plot like this, a "spin-flop" phenomena (a field where the magnetization makes a drastic change) would be necessary [229]. While previous publications with similar samples use this to extract coupling [222], the hysteresis plot seems to show a more complicated switching process taking place. More research would need to be done on the magnetic properties of the individual layers to understand this, or dynamic measurements could be used [230,231].

9.2 Understanding Magnetic Resonance in a Coupled System

Because the magnetization in the individual magnetic layers depends directly on the magnetization of the other layer, the magnetization exhibits two precessional frequencies [223,224]. Finding the resonance frequencies of this complex system can be accomplished by first stating the magnetic free energy per unit area of this system (this is different from a single layer where the energy per volume is important). The areal energy density of a two-layer system is shown in Eq. 9.1 which accounts for uniaxial anisotropy, demagnetization (shape) anisotropy, Zeeman energy (applied magnetic field), and bilinear (J_1) and biquadratic (J_2) exchange [232].

$$F = -J_1\left(\mathbf{m}_1 \cdot \mathbf{m}_2\right) - J_2\left(\mathbf{m}_1 \cdot \mathbf{m}_2\right)^2 + \sum_{i=1}^{2} d_i\left[-K_{\mathrm{u},i}\left(\mathbf{u}_i \cdot \mathbf{m}_i\right)^2 - M_{\mathrm{s},i}\mathbf{m}_i \cdot \mathbf{H}_{\mathrm{ext}} + 2\pi M_{\mathrm{s},i}^2\left(\hat{\mathbf{n}} \cdot \mathbf{m}_i\right)^2\right] \quad 9.1$$

Here $\mathbf{m}_i$ is the normalized magnetization vector direction of a given layer, d_i is the layer thickness, $K_{\mathrm{u},I}$ is the uniaxial magnetic anisotropy, $\mathbf{u}_i$ is the anisotropy direction (easy axis), $M_{\mathrm{s},I}$ is the saturation magnetization, $\mathbf{H}_{\mathrm{ext},I}$ is the applied field vector, and $\hat{\mathbf{n}}$ is surface normal direction.

Prior to determining the magnetization dynamics, it is important to determine the equilibrium magnetization directions for the two layers. The equilibrium directions for the two layers can be

found by taking the derivative of the energy with respect to the magnetization directions (in polar coordinates: θ_i, the angle from the *z*-axis, and φ_i, the angle from the *x*-axis). For the scenario of a sample with perpendicular magnetic anisotropy (**u**||$\hat{\mathbf{z}}$) in both layers and external field applied only in the *x*-*z* plane, the equilibrium direction is always in the *x*-*z* plane ($\varphi_1 = \varphi_2 = 0$), so the energy is only dependent on θ_1 and θ_2. Taking the derivative of the energy with respect to these variables, setting it equal to 0, and solving for θ_1 and θ_2 will provide the equilibrium direction. When coupling is included, solving for the minimum energy will result in a pair of coupled equations:

$$-\sin(2\theta_1)+\frac{2H_{\text{ext}}}{H_{\text{k,eff}_1}}\sin(\theta_{\text{H}}-\theta_1)=\frac{2H_{\text{x,1}}}{H_{\text{k,eff}_1}}\sin(\theta_1-\theta_2)+\frac{2H_{\text{x,2}}}{H_{\text{k,eff}_1}}\sin\left[2(\theta_1-\theta_2)\right], \tag{9.2}$$

$$\sin(2\theta_2)-\frac{2H_{\text{ext}}}{H_{\text{k,eff}_2}}\sin(\theta_{\text{H}}-\theta_2)=\frac{2H_{\text{x,3}}}{H_{\text{k,eff}_2}}\sin(\theta_1-\theta_2)+\frac{2H_{\text{x,4}}}{H_{\text{k,eff}_2}}\sin\left[2(\theta_1-\theta_2)\right], \tag{9.3}$$

where H_{ext} is the magnitude of external field $H_{\text{k,eff}_i}=2K_{\text{u}_i}/M_{\text{s}_i}-4\pi M_{\text{s}_i}$, and the so-called "exchange fields" are given by:

$$H_{\text{x}_1}=\frac{J_1}{d_1 M_{\text{s}_1}}, \tag{9.4}$$

$$H_{\text{x}_2}=\frac{J_2}{d_1 M_{\text{s}_1}}, \tag{9.5}$$

$$H_{\text{x}_3}=\frac{J_1}{d_2 M_{\text{s}_2}}, \tag{9.6}$$

$$H_{\text{ex}_4}=\frac{J_2}{d_2 M_{\text{s}_2}}. \tag{9.7}$$

The values of both θ_1 and θ_2 can be found simultaneously through numerical methods for a given external field and coupling strength. From Eqs. 9.2 and 9.3, the equilibrium directions depend only on dimensionless fields (such as $H_{\text{ext}}/H_{\text{k,eff}_1}$), not the magnetic properties of individual layers. With these dimensionless fields, a bi-layer system can be described with only five variables (of the

six dimensionless fields in Eqs. 9.2 and 9.3, only five are unique). This implies that equilibrium states are not unique for a given set of magnetic parameters, unique magnetization configurations only exist when the dimensionless fields are adjusted.

For a given system, calculating the minimum energy directions for a range external fields can estimate the magnetic hysteresis loop. For a two-layer system, the normalized magnetization can be calculated with Eq. 9.8 [232].

$$\frac{M_{\text{tot}}}{M_{s_1} + M_{s_2}} = \frac{M_{s_1}\cos(\theta_1 - \theta_H) + M_{s_2}\cos(\theta_2 - \theta_H)}{M_{s_1} + M_{s_2}} \qquad 9.8$$

The in-plane magnetization curve is given by setting $\theta_H = \pi / 2$ in Eq. 9.8 (for through-plane magnetization, $\theta_H = 0$). Comparing the magnetization curve generated by Eq. 9.8 to a real sample can provide insight into the magnitude of J_1 and J_2 (provided the magnetic properties of at least one layer are known). This is already used to explain the spin-flop phenomena and has also been used to describe ferromagnetically coupled systems as well [231]. To this end, we plan on characterizing a single layer sample of FePd and using the extracted material properties of this single layer as inputs to determine J_1 and J_2.

As part of the study of magnetization dynamics, we will be studying a perpendicular SAF sample (FePd/Ru/FePd) to determine the magnitude of coupling (both bilinear and biquadratic) from frequency and static measurements. Once the magnitude of the coupling in this system is well understood, the next step would be to apply our knowledge of coupling into the magnetic damping within the bilayer system. Similar to the resonance frequencies, it is possible that the exchange coupling causes a modification of the damping between single layer FePd and SAF FePd systems. This study of damping will require additional modeling to determine the impact of inhomogeneities within both samples on the damping.

9.3 Preliminary Measurement Results

Because these two FePd layers have high anisotropy and a relatively strong coupling, it is difficult to initiate precession with the field applied in-plane. Tilting the applied field out of plane by even 10° ($\theta_H = 80°$) breaks the symmetry and allows the two layers to precess. Since the optical penetration depth is larger than the thickness of the thin film, a single TR-MOKE measurement can track the magnetization of both layers simultaneously. While initial results from this measurement are promising, additional time is needed to both understand the magnetic configuration (including the magnitude of J_1 and J_2) and predict the frequency vs. field relationship. A summary of the preliminary results is shown in Fig. 9.2.

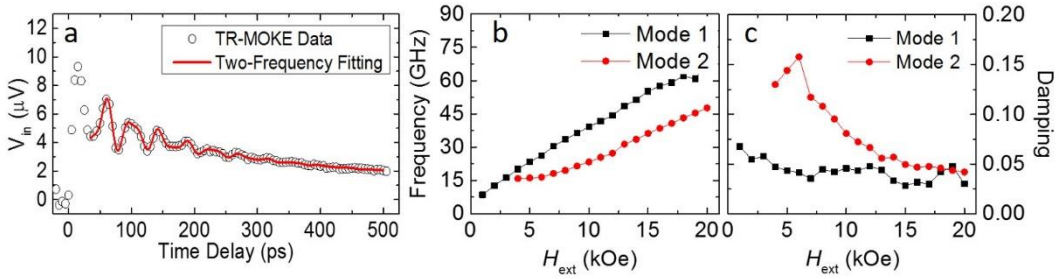

Figure 9.2. (a) Measurement of a FePd/Ru/FePd SAF structure. A representative signal from $H_{ext} = 10$ kOe. The summary of frequency of the damping for both precessional modes as well as the damping of each mode are shown in (b) and (c) respectively.

The raw TR-MOKE data appears to be more erratic than a purely single mode precession, but the two-frequency fitting is able to fit it extremely well as shown in Fig. 9.2a. This was a good indication that two separated frequency modes were precessing simultaneously. The results of the full field scan in Fig. 9.2b show how these two modes change with field. Near ~4 kOe, the two modes are nearly the same frequency and below this field only one mode is detectable. At high fields, the two modes appear to be parallel and increasing with field at the same rate. Initial understanding of these two frequency modes was that one mode (Mode 1) behaves more like an in-plane material (with nearly 0 GHz frequency without external field) while the other mode behaves

like a standard PMA material with an $H_{k,eff} \approx 5$ kOe. This would also explain the trends of effective damping (Fig. 9.2c) where Mode 2 has a peak near 7 kOe and the peak of the damping in Mode 1 is near 0 field. While this seemed to be a good explanation, it is clear from the hysteresis plot (Fig 9.1) that neither layer is completely in-plane. To understand these trends, further research must be done on the theory of coupled resonance.

9.4 Dual Resonance Theory and a Preliminary Parametric Study of Resonance in Coupling

In addition to static measurements, interlayer coupling can also be determined through a study of the magnetization dynamics, specifically the resonance frequency (f) as a function of H_{ext}. While the end result for the case with negligible damping is well-known [6], here I will present the generalized equations for coupled resonance with damping. This will be a specialized version of the proof discussed in Appendix B, so many steps will be skipped. Start with the expanded LLG equation:

$$\frac{d\mathbf{M}_i}{dt} = -\gamma_i \mathbf{M}_i \times \mathbf{H}_{\text{eff},i} + \frac{\alpha_i}{M_{\text{s},i}} \mathbf{M}_i \times \frac{d\mathbf{M}_i}{dt}. \tag{9.9}$$

As shown in Appendix A, these individual equations can be stated in the Landau-Lifshitz form:

$$\frac{d\mathbf{M}_i}{dt} = -\gamma_i \mathbf{M}_i \times \mathbf{H}_{\text{eff},i} - \frac{\alpha_i \gamma_i}{M_{\text{s},i}} \mathbf{M}_i \times \left(\mathbf{M}_i \times \mathbf{H}_{\text{eff},i} \right). \tag{9.10}$$

Following a similar path as Appendix B, it is assumed that $\mathbf{M}_1$ is parallel to $\mathbf{H}_{\text{eff},1}$ and $\mathbf{M}_2$ is parallel to $\mathbf{H}_{\text{eff},2}$.

$$\mathbf{M}_i \times \mathbf{H}_{\text{eff},i} = -M_{\text{s},i} H'_{\varphi,i} \hat{\theta}_i + M_{\text{s},i} H'_{\theta,i} \hat{\varphi}_i \tag{9.11}$$

$$\mathbf{M}_i \times \left(\mathbf{M}_i \times \mathbf{H}_{\text{eff},i} \right) = -M_{\text{s},i}^2 H'_{\theta,i} \hat{\theta}_i - M_{\text{s},i}^2 H'_{\varphi,i} \hat{\varphi}_i \tag{9.12}$$

$$\frac{d\mathbf{M}_i}{dt} = \frac{dM_{\text{s},i}}{dt} \hat{r}_i + M_{\text{s},i} \frac{d\theta_i}{dt} \hat{\theta}_i + M_{\text{s},i} \sin\left(\theta_{0,i}\right) \frac{d\varphi_i}{dt} \hat{\varphi}_i = M_{\text{s},i} \left(\dot{\theta}_i \hat{\theta}_i + \sin\left(\theta_{0,i}\right) \dot{\varphi}_i \hat{\varphi}_i \right) \tag{9.13}$$

This will result in the equation:

$$M_{\mathrm{s},i}\left(\dot{\theta}_i\hat{\theta}_i+\sin\left(\theta_{0,i}\right)\dot{\varphi}_i\hat{\varphi}_i\right)=\gamma_i\left(M_{\mathrm{s},i}H_{\varphi,i}^{'}\hat{\theta}_i-M_{\mathrm{s},i}H_{\theta,i}^{'}\hat{\varphi}_i\right)+\alpha_i\gamma_i\left(M_{\mathrm{s},i}H_{\theta,i}^{'}\hat{\theta}_i+M_{\mathrm{s},i}H_{\varphi,i}^{'}\hat{\varphi}_i\right), \quad 9.14$$

which can also be stated in the form:

$$\dot{\theta}_i=\gamma_i H_{\varphi,i}^{'}+\alpha_i\gamma_i H_{\theta,i}^{'}, \quad 9.15$$

$$\dot{\varphi}_i=\frac{1}{\sin\left(\theta_{0,i}\right)}\left(-\gamma_i H_{\theta,i}^{'}+\alpha_i\gamma_i H_{\varphi,i}^{'}\right). \quad 9.16$$

The definitions for the angular fields need to be updated to incorporate the bilayer system. Start by calculating the derivatives of the free energy:

$$\frac{\partial F}{\partial\theta_i}\approx\left.\frac{\partial F}{\partial\theta_i}\right|_{\theta_{0,i},\varphi_{0,i}}+F_{\theta_i\theta_i}\Delta\theta_i+F_{\theta_i\varphi_i}\Delta\varphi_i+F_{\theta_i\theta_j}\Delta\theta_j+F_{\theta_i\varphi_j}\Delta\varphi_j, \quad 9.17$$

$$\frac{\partial F}{\partial\varphi_i}\approx\left.\frac{\partial F}{\partial\varphi_i}\right|_{\theta_{0,i},\varphi_{0,i}}+F_{\theta_i\varphi_i}\Delta\theta_i+F_{\varphi_i\varphi_i}\Delta\varphi_i+F_{\theta_j\varphi_i}\Delta\theta_j+F_{\varphi_i\varphi_j}\Delta\varphi_j. \quad 9.18$$

This will lead to a complicated matrix that can be simplified assuming the angles are small. The result is a determinant that must be equal to 0:

$$\begin{vmatrix}A_{11} & A_{12}\\ A_{21} & A_{22}\end{vmatrix}=0, \quad 9.19$$

where A_{ij} are each 2×2 matrices:

$$A_{11}=\begin{matrix}-\gamma_1H_{31}-\alpha_1\gamma_1H_{11}-i\lambda & -\gamma_1\sin\left(\theta_1\right)H_{21}-\alpha_1\gamma_1\sin\left(\theta_1\right)H_{31}\\ \dfrac{\gamma_1H_{11}}{\sin\left(\theta_1\right)}-\dfrac{\alpha_1\gamma_1H_{31}}{\sin\left(\theta_1\right)} & \gamma_1H_{31}-\alpha_1\gamma_1H_{21}-i\lambda\end{matrix}, \quad 9.20$$

$$A_{12} = \begin{matrix} -\gamma_1 H_{41x} - \alpha_1\gamma_1 H_{11x} & -\gamma_1 H_{21x}\sin(\theta_1) - \alpha_1\gamma_1 H_{31x}\sin(\theta_1) \\ \dfrac{\gamma_1 H_{11x}}{\sin(\theta_1)} - \dfrac{\alpha_1\gamma_1 H_{41x}}{\sin(\theta_1)} & \gamma_1 H_{31x} - \alpha_1\gamma_1 H_{21x} \end{matrix}, \tag{9.21}$$

$$A_{21} = \begin{matrix} -\gamma_2 H_{32x} - \alpha_2\gamma_2 H_{12x} & -\gamma_2 H_{22x}\sin(\theta_2) - \alpha_2\gamma_2 H_{42x}\sin(\theta_2) \\ \dfrac{\gamma_2 H_{12x}}{\sin(\theta_2)} - \dfrac{\alpha_2\gamma_2 H_{32x}}{\sin(\theta_2)} & \gamma_2 H_{42x} - \alpha_2\gamma_2 H_{22x} \end{matrix}, \tag{9.22}$$

$$A_{22} = \begin{matrix} -\gamma_2 H_{32} - \alpha_2\gamma_2 H_{12} - i\lambda & -\gamma_2\sin(\theta_2) H_{22} - \alpha_2\gamma_2\sin(\theta_2) H_{32} \\ \dfrac{\gamma_2 H_{12}}{\sin(\theta_2)} - \dfrac{\alpha_2\gamma_2 H_{32}}{\sin(\theta_2)} & \gamma_2 H_{32} - \alpha_2\gamma_2 H_{22} - i\lambda \end{matrix}. \tag{9.23}$$

In order to simplify this equation to this point, seven new variables had to be defined.

$$H_{1i} = \frac{1}{M_{\mathrm{s},i}} F_{\theta_i\theta_i} \tag{9.24}$$

$$H_{2i} = \frac{1}{M_{\mathrm{s},i}\sin^2(\theta_i)} F_{\varphi_i\varphi_i} \tag{9.25}$$

$$H_{3i} = \frac{1}{M_{\mathrm{s},i}\sin(\theta_i)} F_{\theta_i\varphi_i} \tag{9.26}$$

$$H_{1ix} = \frac{F_{\theta_1\theta_2}}{M_{\mathrm{s},i}} \tag{9.27}$$

$$H_{2ix} = \frac{F_{\varphi_1\varphi_2}}{M_{\mathrm{s},i}\sin^2(\theta_i)} \tag{9.28}$$

$$H_{3ix} = \frac{F_{\theta_1\varphi_2}}{M_{\mathrm{s},i}\sin(\theta_i)} \tag{9.29}$$

$$H_{4ix} = \frac{F_{\theta_2\varphi_1}}{M_{\mathrm{s},i}\sin(\theta_i)} \tag{9.30}$$

Solving for λ will provide up to two meaningful values of resonance frequency for the entire system. Fitting the two frequency modes from a real sample to theoretical results from Eq. 9.19 will provide the magnitude of coupling (provided the magnetic properties of at least one of the two layers). Due to the complexity of the system, it is not possible to do this calculation analytically unless the damping is assumed to be negligible. For the cases where this is not true (such as in our system), everything must be done analytically. As a first attempt to understand frequency and magnetization in coupled systems, a parametric study was conducted (without damping) as a first stage in understanding how different amounts of damping will impact the results. Figure 9.3 shows the results of changing the J_1 and J_2 values for two matching layers. The bilinear coupling acts to open up a frequency gap between the two modes while the biquadratic coupling acts to change one mode to act as an in-plane mode (similar to the measured situation). While J_2 explains the in-plane mode, it also shifts the second mode to higher frequencies. More research is needed to understand the exact balance of coupling parameters in the FePd/Ru/FePd SAF structure such as analyzing the two films individually.

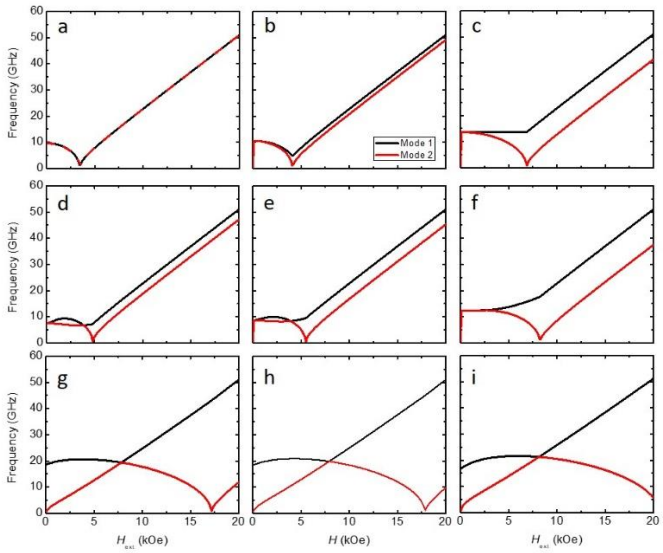

Figure 9.3. A summary of the parametric study of coupled resonance in a bilayer system. The results are shown in a grid where going from left to right is an increase in J_1 (0, -0.1, and -0.5 emu/cm^2) and going from top to bottom increases J_2 (0, -0.1, and -0.5 emu/cm^2) starting at (a) no coupling and ending at (i) maximum J_1 and J_2. Both layers have $H_{k,eff}$ = 3.4 kOe and thickness of 5 nm.

9.5 Conclusion

For future magnetic free-layers in STT-MRAM devices, previous publications have shown the possibility of using synthetic anitiferromagnets, such as the FePd/Ru/FePd structure studied here. Here, we attempted to characterize the damping in the material to extract the strength and type of coupling between the two layers as well as the damping. Through solving the LLG equation for a coupled system, I have been able to provide an equation for the resonance and relaxation for a coupled system. The complexity of this equation means that we need to know more about the system (especially the magnetic properties of individual layers) to extract coupling strengths. For this reason, I attempted to go through a parametric study of coupling strengths and it seems that a single uniaxial anisotropy and both bilinear and biquadratic coupling are not able to completely describe the system. Furthermore, further research is needed to determine how to calculate the intrinsic damping in the system from inhomogeneous broadening. We still were able to show with direct the coupled resonance of a perpendicular SAF structure in our initial study, which is a first to my knowledge.

CHAPTER 10: CONCLUSION AND OUTLOOK

As technology continues to shrink in scale and technological advancements such as the field of spintronics come to life, it becomes increasingly important to study materials' transport behaviors on the ultrafast time scale. In this chapter, we have discussed a number of applications for TR-MOKE measurements including measurements of thermal properties, magnetization dynamics, and the coupling between the two. As we have shown, TR-MOKE has been applied to understand complex materials with high anisotropy, and to increase the measurement sensitivity to the thermal transport within materials and across interfaces.

With the results of my research, I have been able to advance the understanding of the magnetization dynamics in perpendicular magnetic materials with the use of TR-MOKE. Through a numerical understanding, I was able to provide an understanding of how to increase the signal for TR-MOKE measurements which enabled me to do the rest of my research. One such advancement was with the W/CoFeB/MgO stack that was shown to have a comparable damping to the existing technologies but was also able to maintain its magnetic properties to 400 °C, which is compatible with back end of the line semiconductor processing. With this research, I hope that W-seeded technologies become to be more widely applied in STT-MRAM. Building off of this research, I also explored three new measurements to reveal new physics: magneto-acoustic coupling, temperature dependent magnetization dynamics, and resonance in coupled structures. The magneto-acoustic coupling shown in Co/Pd samples could be used for lower energy switching technologies that make use of high frequency strain to assist switching. High-temperature experiments reveal how materials (such as CoFeB and FePd) behave under high temperature operating conditions for STT-MRAM. This could act to provide additional details to assist in the design of STT-MRAM and could provide information about failure conditions as well. As the temperature continues to increase and the temperature approaches the Curie temperature, the results of my research could help improve technologies such as HAMR as it approaches a widespread

release to consumers. Lastly, the FePd SAF structure measured could also act to reduce the power in STT-MRAM, but it requires additional understanding. My research so far has provided a framework for predicting hysteresis plots and frequency trends for the coupled system and shown an initial set of results for a complex coupled system.

While the research shown has been crucial to understand magnetization in perpendicular magnetic materials, there are many aspects that I believe deserve further study in the future. The mechanism of inhomogeneous is not well understood and is often discarded in both FMR and TR-MOKE measurements. In my initial foray into the LLB equation, I tried to understand if the Gaussian heat spot could be the source of the large inhomogeneous broadening in TR-MOKE (compared to FMR). As such, I started an initial numerical simulation that averaged the magnetization dynamics over a large spot size (a pseudo-microspin model). Understanding this inhomogeneous broadening could be extremely helpful for the laser-assisted HAMR and also for the extraction of accurate damping results in TR-MOKE. Additionally, the multiple resonances in Co/Pd materials could provide a lower energy method of switching materials and requires further measurements. The SAF structure is also of great importance for reducing the large STT-MRAM switching current and being able to extract inhomogeneous broadening from TR-MOKE results from this material would require a large amount of processing power with my current methods. Lastly, with my research in the temperature dependence on magnetization and exciting new research into unique physics such as the coupling between energy carriers, the MNTTL is poised to research more into the field of caloritronics to use magnets to generate current. The results of these experimental studies can improve the design of future devices and interfaces for better thermal management.

BIBLIOGRAPHY

[1] Moore, G. E., **2006**, IEEE Solid-State Circuits Society Newsletter, 11(3), pp. 36-37.

[2] Theis, T. N., and Wong, H.-S. P., **2017**, Computing in Science & Engineering, 19(2), pp. 41-50.

[3] Baibich, M. N., Broto, J. M., Fert, A., Van Dau, F. N., Petroff, F., Etienne, P., Creuzet, G., Friederich, A., and Chazelas, J., **1988**, Physical Review Letters, 61(21), pp. 2472-2475.

[4] Binasch, G., Grünberg, P., Saurenbach, F., and Zinn, W., **1989**, Physical Review B, 39(7), pp. 4828-4830.

[5] Tehrani, S., Slaughter, J. M., Chen, E., Durlam, M., Shi, J., and DeHerren, M., **1999**, IEEE Transactions on Magnetics, 35(5), pp. 2814-2819.

[6] Slonczewski, J. C., **1996**, Journal of Magnetism and Magnetic Materials, 159(1), pp. L1-L7.

[7] Berger, L., **1996**, Physical Review B, 54(13), pp. 9353-9358.

[8] Liu, L., Pai, C.-F., Li, Y., Tseng, H. W., Ralph, D. C., and Buhrman, R. A., **2012**, Science, 336(6081), pp. 555-558.

[9] Cubukcu, M., Boulle, O., Mikuszeit, N., Hamelin, C., Brächer, T., Lamard, N., Cyrille, M., Buda-Prejbeanu, L., Garello, K., Miron, I. M., Klein, O., Loubens, G. d., Naletov, V. V., Langer, J., Ocker, B., Gambardella, P., and Gaudin, G., **2018**, IEEE Transactions on Magnetics, 54(4), pp. 1-4.

[10] Kim, J., Paul, A., Crowell, P. A., Koester, S. J., Sapatnekar, S. S., Wang, J., and Kim, C. H., **2015**, Proceedings of the IEEE, 103(1), pp. 106-130.

[11] Behin-Aein, B., Datta, D., Salahuddin, S., and Datta, S., **2010**, Nature Nanotechnology, 5(4), pp. 266-270.

[12] Camsari, K. Y., Faria, R., Sutton, B. M., and Datta, S., **2017**, Physical Review X, 7(3), p. 031014.

[13] Kiselev, S. I., Sankey, J. C., Krivorotov, I. N., Emley, N. C., Schoelkopf, R. J., Buhrman, R. A., and Ralph, D. C., **2003**, Nature, 425(6956), pp. 380-383.

[14] Kaka, S., Pufall, M. R., Rippard, W. H., Silva, T. J., Russek, S. E., and Katine, J. A., **2005**, Nature, 437(7057), pp. 389-392.

[15] Houssameddine, D., Ebels, U., Delaët, B., Rodmacq, B., Firastrau, I., Ponthenier, F., Brunet, M., Thirion, C., Michel, J. P., Prejbeanu-Buda, L., Cyrille, M. C., Redon, O., and Dieny, B., **2007**, Nature Materials, 6(6), pp. 447-453.

[16] Mizushima, K., Kudo, K., and Sato, R., **2007**, Journal of Magnetism and Magnetic Materials, 316(2), pp. e960-e962.

[17] Kryder, M. H., Gage, E. C., McDaniel, T. W., Challener, W. A., Rottmayer, R. E., Ju, G., Hsia, Y., and Erden, M. F., **2008**, Proceedings of the IEEE, 96(11), pp. 1810-1835.

[18] Challener, W. A., Peng, C., Itagi, A. V., Karns, D., Peng, W., Peng, Y., Yang, X., Zhu, X., Gokemeijer, N. J., Hsia, Y. T., Ju, G., Rottmayer, R. E., Seigler, M. A., and Gage, E. C., **2009**, Nature Photonics, 3(4), pp. 220-224.

[19] Ju, G., Peng, Y., Chang, E. K. C., Ding, Y., Wu, A. Q., Zhu, X., Kubota, Y., Klemmer, T. J., Amini, H., Gao, L., Fan, Z., Rausch, T., Subedi, P., Ma, M., Kalarickal, S., Rea, C. J., Dimitrov, D. V., Huang, P., Wang, K., Chen, X., Peng, C., Chen, W., Dykes, J. W., Seigler, M. A., Gage, E. C., Chantrell, R., and Thiele, J., **2015**, IEEE Transactions on Magnetics, 51(11), pp. 1-9.

[20] Kittel, C., **1948**, Physical Review, 73(2), pp. 155-161.

[21] Kittel, C., **1947**, Physical Review, 71(4), pp. 270-271.

[22] Rossing, T. D., **1963**, Journal of Applied Physics, 34(4), pp. 995-995.

[23] Farle, M., Silva, T., and Woltersdorf, G., **2013**, Magnetic Nanostructures: Spin Dynamics and Spin Transport, H. Zabel, and M. Farle, eds., Springer Berlin Heidelberg, Berlin, Heidelberg, pp. 37-83.

[24] van Kampen, M., Jozsa, C., Kohlhepp, J. T., LeClair, P., Lagae, L., de Jonge, W. J. M., and Koopmans, B., **2002**, Physical Review Letters, 88(22), p. 227201.

[25] Barman, A., Kimura, T., Otani, Y., Fukuma, Y., Akahane, K., and Meguro, S., **2008**, Review of Scientific Instruments, 79(12), p. 123905.

[26] Liu, J., Choi, G.-M., and Cahill, D. G., **2014**, Journal of Applied Physics, 116(23), p. 233107.

[27] Zhu, J., Park, H., Chen, J.-Y., Gu, X., Zhang, H., Karthikeyan, S., Wendel, N., Campbell, S. A., Dawber, M., Du, X., Li, M., Wang, J.-P., Yang, R., and Wang, X., **2016**, Advanced Electronic Materials, 2(5), p. 1600040.

[28] Stoner, E. C., and Wohlfarth, E. P., **1948**, Philosophical Transactions of the Royal Society of London. Series A, Mathematical and Physical Sciences, 240(826), pp. 599-642.

[29] Stoner, E. C., and Wohlfarth, E. P., **1991**, IEEE Transactions on Magnetics, 27(4), pp. 3475-3518.

[30] Gilbert, T. L., **2004**, IEEE Transactions on Magnetics, 40(6), pp. 3443-3449.

[31] Chang, H., Li, P., Zhang, W., Liu, T., Hoffmann, A., Deng, L., and Wu, M., **2014**, IEEE Magnetics Letters, 5, pp. 1-4.

[32] Schoen, M. A. W., Thonig, D., Schneider, M. L., Silva, T. J., Nembach, H. T., Eriksson, O., Karis, O., and Shaw, J. M., **2016**, Nature Physics, 12, p. 839.

[33] Brown, W. F., **1963**, Micromagnetics, Interscience Publishers, New York.

[34] Hoefer, M. A., Ablowitz, M. J., Ilan, B., Pufall, M. R., and Silva, T. J., **2005**, Physical Review Letters, 95(26), p. 267206.

[35] Silva, T. J., and Rippard, W. H., **2008**, Journal of Magnetism and Magnetic Materials, 320(7), pp. 1260-1271.

[36] Sun, J. Z., **2000**, Physical Review B, 62(1), pp. 570-578.

[37] Kamberský, V., **1970**, Canadian Journal of Physics, 48(24), pp. 2906-2911.

[38] Elliott, R. J., **1954**, Physical Review, 96(2), pp. 266-279.

[39] Kuneš, J., and Kamberský, V., **2002**, Physical Review B, 65(21), p. 212411.

[40] Steiauf, D., and Fähnle, M., **2005**, Physical Review B, 72(6), p. 064450.

[41] Fähnle, M., and Steiauf, D., **2006**, Physical Review B, 73(18), p. 184427.

[42] Kamberský, V., **2007**, Physical Review B, 76(13), p. 134416.

[43] Kamberský, V., **1976**, Czechoslovak Journal of Physics B, 26(12), pp. 1366-1383.

[44] Gilmore, K., Idzerda, Y. U., and Stiles, M. D., **2008**, Journal of Applied Physics, 103(7), p. 07D303.

[45] Iihama, S., Sakuma, A., Naganuma, H., Oogane, M., Miyazaki, T., Mizukami, S., and Ando, Y., **2014**, Applied Physics Letters, 105(14), p. 142403.

[46] Qu, T., and Victora, R. H., **2015**, Applied Physics Letters, 106(7), p. 072404.

[47] He, P., Ma, X., Zhang, J. W., Zhao, H. B., Lüpke, G., Shi, Z., and Zhou, S. M., **2013**, Physical Review Letters, 110(7), p. 077203.

[48] Iihama, S., Sakuma, A., Naganuma, H., Oogane, M., Mizukami, S., and Ando, Y., **2016**, Physical Review B, 94(17), p. 174425.

[49] Sakuma, A., **2012**, Journal of the Physical Society of Japan, 81(8), p. 084701.

[50] Daalderop, G. H. O., Kelly, P. J., and Schuurmans, M. F. H., **1991**, Physical Review B, 44(21), pp. 12054-12057.

[51] Arias, R., and Mills, D. L., **1999**, Physical Review B, 60(10), pp. 7395-7409.

[52] Landeros, P., Arias, R. E., and Mills, D. L., **2008**, Physical Review B, 77(21), p. 214405.

[53] McMichael, R. D., and Krivosik, P., **2004**, IEEE Transactions on Magnetics, 40(1), pp. 2-11.

[54] Dobin, A. Y., and Victora, R. H., **2003**, Physical Review Letters, 90(16), p. 167203.

[55] Tserkovnyak, Y., Brataas, A., and Bauer, G. E. W., **2002**, Physical Review Letters, 88(11), p. 117601.

[56] S. Mizukami, Y. Ando, and T. Miyazaki, **2001**, Japanese Journal of Applied Physics, 40(2R), p. 580.

[57] Urban, R., Woltersdorf, G., and Heinrich, B., **2001**, Physical Review Letters, 87(21), p. 217204.

[58] Iihama, S., Mizukami, S., Naganuma, H., Oogane, M., Ando, Y., and Miyazaki, T., **2014**, Physical Review B, 89(17), p. 174416.

[59] Kerr, J., **1900**, The Effects of a Magnetic Field on Radiation, E. P. Lewis, ed., American Book Company, New York, pp. 27-52.

[60] Yang, Z. J., and Scheinfein, M. R., **1993**, Journal of Applied Physics, 74(11), pp. 6810-6823.

[61] You, C. Y., and Shin, S. C., **1996**, Applied Physics Letters, 69(9), pp. 1315-1317.

[62] You, C.-Y., and Shin, S.-C., **1998**, Journal of Applied Physics, 84(1), pp. 541-546.

[63] Krinchik, G. S., and Artemev, V. A., **1968**, Soviet Journal of Experimental and Theoretical Physics, 26(6), pp. 1080-1085.

[64] Qiu, Z. Q., and Bader, S. D., **2000**, Review of Scientific Instruments, 71(3), pp. 1243-1255.

[65] Huang, B., Clark, G., Navarro-Moratalla, E., Klein, D. R., Cheng, R., Seyler, K. L., Zhong, D., Schmidgall, E., McGuire, M. A., Cobden, D. H., Yao, W., Xiao, D., Jarillo-Herrero, P., and Xu, X., **2017**, Nature, 546, p. 270.

[66] Schmidt, F., Rave, W., and Hubert, A., **1985**, IEEE Transactions on Magnetics, 21(5), pp. 1596-1598.

[67] Rave, W., Schäfer, R., and Hubert, A., **1987**, Journal of Magnetism and Magnetic Materials, 65(1), pp. 7-14.

[68] Agranat, M. B., Ashitkov, S. I., Granovskii, A. B., and Rukman, G. I., **1984**, Soviet Journal of Experimental and Theoretical Physics, 59(4), pp. 804-806.

[69] Vaterlaus, A., Beutler, T., Guarisco, D., Lutz, M., and Meier, F., **1992**, Physical Review B, 46(9), pp. 5280-5286.

[70] Beaurepaire, E., Merle, J. C., Daunois, A., and Bigot, J. Y., **1996**, Physical Review Letters, 76(22), pp. 4250-4253.

[71] Ju, G., Nurmikko, A. V., Farrow, R. F. C., Marks, R. F., Carey, M. J., and Gurney, B. A., **1999**, Physical Review Letters, 82(18), pp. 3705-3708.

[72] Ju, G., Chen, L., Nurmikko, A. V., Farrow, R. F. C., Marks, R. F., Carey, M. J., and Gurney, B. A., **2000**, Physical Review B, 62(2), pp. 1171-1177.

[73] Zhu, J., Wu, X., Lattery, D. M., Zheng, W., and Wang, X., **2017**, Nanoscale and Microscale Thermophysical Engineering, 21(3), pp. 177-198.

[74] Koopmans, B., **2003**, Spin Dynamics in Confined Magnetic Structures II, B. Hillebrands, and K. Ounadjela, eds., Springer-Verlag Berlin Heidelberg, Berlin, pp. 253-316.

[75] Kang, K., Koh, Y. K., Chiritescu, C., Zheng, X., and Cahill, D. G., **2008**, Review of Scientific Instruments, 79(11), p. 114901.

[76] Feser, J. P., Liu, J., and Cahill, D. G., **2014**, Review of Scientific Instruments, 85(10), p. 104903.

[77] Kucukgok, B., Wu, X., Wang, X., Liu, Z., Ferguson, I. T., and Lu, N., **2016**, AIP Advances, 6(2), p. 025305.

[78] Zhu, J., Zhu, Y., Wu, X., Song, H., Zhang, Y., and Wang, X., **2016**, Applied Physics Letters, 108(23), p. 231903.

[79] Zheng, K., Sun, F., Zhu, J., Ma, Y., Li, X., Tang, D., Wang, F., and Wang, X., **2016**, ACS Nano, 10(8), pp. 7792-7798.

[80] Prakash, A., Xu, P., Wu, X., Haugstad, G., Wang, X., and Jalan, B., **2017**, Journal of Materials Chemistry C, 5(23), pp. 5730-5736.

[81] Wu, X., Walter, J., Feng, T., Zhu, J., Zheng, H., Mitchell, J. F., Biškup, N., Varela, M., Ruan, X., Leighton, C., and Wang, X., **2017**, Advanced Functional Materials, 27(47), p. 1704233.

[82] Xu, D., Wang, Q., Wu, X., Zhu, J., Zhao, H., Xiao, B., Wang, X., Wang, X., and Hao, Q., **2018**, Frontiers in Energy, 12(1), pp. 127-136.

[83] Chen, L., Zhang, Y., Wang, X., Jalan, B., Chen, S., and Hou, Y., **2018**, The Journal of Physical Chemistry C, 122(21), pp. 11482-11490.

[84] Zhu, J., Feng, T., Mills, S., Wang, P., Wu, X., Zhang, L., Pantelides, S. T., Du, X., and Wang, X., **2018**, ACS Applied Materials & Interfaces, 10(47), pp. 40740-40747.

[85] Thomsen, C., Strait, J., Vardeny, Z., Maris, H. J., Tauc, J., and Hauser, J. J., **1984**, Physical Review Letters, 53(10), pp. 989-992.

[86] O'Hara, K. E., Hu, X., and Cahill, D. G., **2001**, Journal of Applied Physics, 90(9), pp. 4852-4858.

[87] Antonelli, G. A., Perrin, B., Daly, B. C., and Cahill, D. G., **2006**, MRS Bulletin, 31(8), pp. 607-613.

[88] Hohensee, G. T., Hsieh, W.-P., Losego, M. D., and Cahill, D. G., **2012**, Review of Scientific Instruments, 83(11), p. 114902.

[89] Lin, H. N., Stoner, R. J., Maris, H. J., and Tauc, J., **1991**, Journal of Applied Physics, 69(7), pp. 3816-3822.

[90] O'Handley, R. C., **2000**, Modern Magnetic Materials, John Wiley & Sons, Inc.

[91] Kotze, J., **2008**, arXiv preprint arXiv:0803.0217.

[92] Greaves, S. J., Muraoka, H., and Kanai, Y., **2012**, Journal of Applied Physics, 111(7), p. 07B706.

[93] Zhao, H., Glass, B., Amiri, P. K., Lyle, A., Zhang, Y., Chen, Y.-J., Rowlands, G., Upadhyaya, P., Zeng, Z., Katine, J. A., Langer, J., Galatsis, K., Jiang, H., Wang, K. L., Krivorotov, I. N., and Wang, J.-P., **2012**, Journal of Physics D: Applied Physics, 45(2), p. 025001.

[94] Wang, D.-S., Lai, S.-Y., Lin, T.-Y., Chien, C.-W., Ellsworth, D., Wang, L.-W., Liao, J.-W., Lu, L., Wang, Y.-H., Wu, M., and Lai, C.-H., **2014**, Applied Physics Letters, 104(14), p. 142402.

[95] Zakeri, K., Lindner, J., Barsukov, I., Meckenstock, R., Farle, M., von Hörsten, U., Wende, H., Keune, W., Rocker, J., Kalarickal, S. S., Lenz, K., Kuch, W., Baberschke, K., and Frait, Z., **2007**, Physical Review B, 76(10), p. 104416.

[96] Schoen, M. A. W., Lucassen, J., Nembach, H. T., Silva, T. J., Koopmans, B., Back, C. H., and Shaw, J. M., **2017**, Physical Review B, 95(13), p. 134410.

[97] Schoen, M. A. W., Lucassen, J., Nembach, H. T., Koopmans, B., Silva, T. J., Back, C. H., and Shaw, J. M., **2017**, Physical Review B, 95(13), p. 134411.

[98] Mizukami, S., Wu, F., Sakuma, A., Walowski, J., Watanabe, D., Kubota, T., Zhang, X., Naganuma, H., Oogane, M., Ando, Y., and Miyazaki, T., **2011**, Physical Review Letters, 106(11), p. 117201.

[99] Becker, J., Mosendz, O., Weller, D., Kirilyuk, A., Maan, J. C., Christianen, P. C. M., Rasing, T., and Kimel, A., **2014**, Applied Physics Letters, 104(15), p. 152412.

[100] Zhang, B., Cao, A., Qiao, J., Tang, M., Cao, K., Zhao, X., Eimer, S., Si, Z., Lei, N., Wang, Z., Lin, X., Zhang, Z., Wu, M., and Zhao, W., **2017**, Applied Physics Letters, 110(1), p. 012405.

[101] Lattery, D. M., Zhang, D., Zhu, J., Hang, X., Wang, J.-P., and Wang, X., **2018**, Scientific Reports, 8(1), p. 13395.

[102] Mizukami, S., Watanabe, D., Kubota, T., Zhang, X., Naganuma, H., Oogane, M., Ando, Y., and Miyazaki, T., **2010**, Applied Physics Express, 3(12), p. 123001.

[103] Capua, A., Yang, S.-h., Phung, T., and Parkin, S. S. P., **2015**, Physical Review B, 92(22), p. 224402.

[104] Wu, D., Li, W., Tang, M., Zhang, Z., Lou, S., and Jin, Q. Y., **2016**, Journal of Magnetism and Magnetic Materials, 409, pp. 143-147.

[105] Iida, S., **1963**, Journal of Physics and Chemistry of Solids, 24(5), pp. 625-630.

[106] Beaujour, J. M., Ravelosona, D., Tudosa, I., Fullerton, E. E., and Kent, A. D., **2009**, Physical Review B, 80(18), p. 180415.

[107] Ikeda, S., Miura, K., Yamamoto, H., Mizunuma, K., Gan, H. D., Endo, M., Kanai, S., Hayakawa, J., Matsukura, F., and Ohno, H., **2010**, Nature Materials, 9, p. 721.

[108] Sato, H., Enobio, E. C. I., Yamanouchi, M., Ikeda, S., Fukami, S., Kanai, S., Matsukura, F., and Ohno, H., **2014**, Applied Physics Letters, 105(6), p. 062403.

[109] Sun, J. Z., Brown, S. L., Chen, W., Delenia, E. A., Gaidis, M. C., Harms, J., Hu, G., Jiang, X., Kilaru, R., Kula, W., Lauer, G., Liu, L. Q., Murthy, S., Nowak, J., O'Sullivan, E. J., Parkin, S. S. P., Robertazzi, R. P., Rice, P. M., Sandhu, G., Topuria, T., and Worledge, D. C., **2013**, Physical Review B, 88(10), p. 104426.

[110] Zhu, J., Katine, J. A., Rowlands, G. E., Chen, Y.-J., Duan, Z., Alzate, J. G., Upadhyaya, P., Langer, J., Amiri, P. K., Wang, K. L., and Krivorotov, I. N., **2012**, Physical Review Letters, 108(19), p. 197203.

[111] Wang, W. G., Li, M. G., Hageman, S., and Chien, C. L., **2012**, Nature Materials, 11(1), pp. 64-68.

[112] Kanai, S., Yamanouchi, M., Ikeda, S., Nakatani, Y., Matsukura, F., and Ohno, H., **2012**, Applied Physics Letters, 101(12), p. 122403.

[113] Yu, G. Q., Upadhyaya, P., Fan, Y. B., Alzate, J. G., Jiang, W. J., Wong, K. L., Takei, S., Bender, S. A., Chang, L. T., Jiang, Y., Lang, M. R., Tang, J. S., Wang, Y., Tserkovnyak, Y., Amiri, P. K., and Wang, K. L., **2014**, Nature Nanotechnology, 9(7), pp. 548-554.

[114] Bhowmik, D., You, L., and Salahuddin, S., **2014**, Nature Nanotechnology, 9(1), pp. 59-63.

[115] Jiang, W. J., Upadhyaya, P., Zhang, W., Yu, G. Q., Jungfleisch, M. B., Fradin, F. Y., Pearson, J. E., Tserkovnyak, Y., Wang, K. L., Heinonen, O., te Velthuis, S. G. E., and Hoffmann, A., **2015**, Science, 349(6245), pp. 283-286.

[116] Yu, G., Upadhyaya, P., Shao, Q., Wu, H., Yin, G., Li, X., He, C., Jiang, W., Han, X., Amiri, P. K., and Wang, K. L., **2017**, Nano Letters, 17(1), pp. 261-268.

[117] Diao, Z. T., Li, Z. J., Wang, S. Y., Ding, Y. F., Panchula, A., Chen, E., Wang, L. C., and Huai, Y. M., **2007**, Journal of Physics: Condensed Matter, 19(16), p. 165209.

[118] Manipatruni, S., Nikonov, D. E., and Young, I. A., **2014**, Applied Physics Express, 7(10), p. 103001.

[119] Annunziata, A. J., Trouilloud, P. L., Bandiera, S., Brown, S. L., Gapihan, E., O'Sullivan, E. J., and Worledge, D. C., **2015**, Journal of Applied Physics, 117(17), p. 17B739.

[120] Miyakawa, N., Worledge, D. C., and Kita, K., **2013**, IEEE Magnetics Letters, 4, p. 1000104.

[121] Yang, S., Lee, J., An, G., Kim, J., Chung, W., and Hong, J., **2014**, Journal of Applied Physics, 116(11), p. 113902.

[122] Gan, H. D., Sato, H., Yamanouchi, M., Ikeda, S., Miura, K., Koizumi, R., Matsukura, F., and Ohno, H., **2011**, Applied Physics Express, 99(25), p. 252507.

[123] Suhl, H., **1998**, IEEE Transactions on Magnetics, 34(4), pp. 1834-1838.

[124] Ikeda, S., Hayakawa, J., Ashizawa, Y., Lee, Y. M., Miura, K., Hasegawa, H., Tsunoda, M., Matsukura, F., and Ohno, H., **2008**, Applied Physics Letters, 93(8), p. 082508.

[125] Liu, T., Zhang, Y., Cai, J. W., and Pan, H. Y., **2014**, Scientific Reports, 4, p. 5895.

[126] Almasi, H., Hickey, D. R., Newhouse-Illige, T., Xu, M., Rosales, M. R., Nahar, S., Held, J. T., Mkhoyan, K. A., and Wang, W. G., **2015**, Applied Physics Letters, 106(18), p. 182406.

[127] Cho, S., Baek, S.-h. C., Lee, K.-D., Jo, Y., and Park, B.-G., **2015**, Scientific Reports, 5, p. 14668.

[128] Pai, C. F., Liu, L. Q., Li, Y., Tseng, H. W., Ralph, D. C., and Buhrman, R. A., **2012**, Applied Physics Letters, 101(12), p. 122404.

[129] Liu, J., Ohkubo, T., Mitani, S., Hono, K., and Hayashi, M., **2015**, Applied Physics Letters, 107(23), p. 232408.

[130] He, C., Navabi, A., Shao, Q., Yu, G., Wu, D., Zhu, W., Zheng, C., Li, X., He, Q. L., Razavi, S. A., Wong, K. L., Zhang, Z., Amiri, P. K., and Wang, K. L., **2016**, Applied Physics Letters, 109(20), p. 202404.

[131] Skowroński, W., Nozaki, T., Lam, D. D., Shiota, Y., Yakushiji, K., Kubota, H., Fukushima, A., Yuasa, S., and Suzuki, Y., **2015**, Physical Review B, 91(18), p. 184410.

[132] Chatterjee, J., Sousa, R. C., Perrissin, N., Auffret, S., Ducruet, C., and Dieny, B., **2017**, Applied Physics Letters, 110(20), p. 202401.

[133] An, G.-G., Lee, J.-B., Yang, S.-M., Kim, J.-H., Chung, W.-S., and Hong, J.-P., **2015**, Acta Materialia, 87(Supplement C), pp. 259-265.

[134] Almasi, H., Sun, C. L., Li, X., Newhouse-Illige, T., Bi, C., Price, K. C., Nahar, S., Grezes, C., Hu, Q., Amiri, P. K., Wang, K. L., Voyles, P. M., and Wang, W. G., **2017**, Journal of Applied Physics, 121(15), p. 153902.

[135] Liu, T., Cai, J. W., and Sun, L., **2012**, AIP Advances, 2(3), p. 032151.

[136] Swamy, G. V., Rout, P. K., Manju, S., and Rakshit, R. K., **2015**, Journal of Physics D: Applied Physics, 48(47), p. 475002.

[137] Cecot, M., Karwacki, Ł., Skowroński, W., Kanak, J., Wrona, J., Żywczak, A., Yao, L., Dijken, S., Barnaś, J., and Stobiecki, T., **2017**, Scientific Reports, 7, p. 968.

[138] Bjorck, M., and Andersson, G., **2007**, Journal of Applied Crystallography, 40(6), pp. 1174-1178.

[139] Iihama, S., Mizukami, S., Inami, N., Hiratsuka, T., Kim, G., Naganuma, H., Oogane, M., Miyazaki, T., and Yasuo, A., **2013**, Japanese Journal of Applied Physics, 52(7R), p. 073002.

[140] Takahashi, Y. K., Miura, Y., Choi, R., Ohkubo, T., Wen, Z. C., Ishioka, K., Mandal, R., Medapalli, R., Sukegawa, H., Mitani, S., Fullerton, E. E., and Hono, K., **2017**, Applied Physics Letters, 110(25), p. 252409.

[141] Krivosik, P., Mo, N., Kalarickal, S., and Patton, C. E., **2007**, Journal of Applied Physics, 101(8), p. 083901.

[142] Ma, L., Li, S. F., He, P., Fan, W. J., Xu, X. G., Jiang, Y., Lai, T. S., Chen, F. L., and Zhou, S. M., **2014**, Journal of Applied Physics, 116(11), p. 113908.

[143] Mizukami, S., **2015**, Journal of the Magnetics Society of Japan, 39(1), pp. 1-7.

[144] Suhl, H., **1955**, Physical Review, 97(2), pp. 555-557.

[145] Ikeda, S., Miura, K., Yamamoto, H., Mizunuma, K., Gan, H. D., Endo, M., Kanai, S., Hayakawa, J., Matsukura, F., and Ohno, H., **2010**, Nat. Mater., 9(9), pp. 721-724.

[146] Yilgin, R., Oogane, M., Yakata, S., Ando, Y., and Miyazaki, T., **2005**, IEEE Transactions on Magnetics, 41(10), pp. 2799-2801.

[147] Skowroński, W., Cecot, M., Kanak, J., Ziętek, S., Stobiecki, T., Yao, L., Dijken, S. v., Nozaki, T., Yakushiji, K., and Yuasa, S., **2016**, Applied Physics Letters, 109(6), p. 062407.

[148] Joule, J., **1842**, Annals of Electricity, Magnetism, and Chemistry, 8, pp. 219-224.

[149] Kim, J.-W., Vomir, M., and Bigot, J.-Y., **2012**, Physical Review Letters, 109(16), p. 166601.

[150] Jäger, J. V., Scherbakov, A. V., Linnik, T. L., Yakovlev, D. R., Wang, M., Wadley, P., Holy, V., Cavill, S. A., Akimov, A. V., Rushforth, A. W., and Bayer, M., **2013**, Applied Physics Letters, 103(3), p. 032409.

[151] Jäger, J. V., Scherbakov, A. V., Glavin, B. A., Salasyuk, A. S., Campion, R. P., Rushforth, A. W., Yakovlev, D. R., Akimov, A. V., and Bayer, M., **2015**, Physical Review B, 92(2), p. 020404.

[152] Kirilyuk, A., Kimel, A. V., and Rasing, T., **2010**, Reviews of Modern Physics, 82(3), pp. 2731-2784.

[153] Li, T., Patz, A., Mouchliadis, L., Yan, J., Lograsso, T. A., Perakis, I. E., and Wang, J., **2013**, Nature, 496(7443), pp. 69-73.

[154] Temnov, V. V., **2012**, Nature Photonics, 6(11), pp. 728-736.

[155] Shen, K., and Bauer, G. E. W., **2015**, Physical Review Letters, 115(19), p. 197201.

[156] Man, H., Shi, Z., Xu, G., Xu, Y., Chen, X., Sullivan, S., Zhou, J., Xia, K., Shi, J., and Dai, P., **2017**, Physical Review B, 96(10), p. 100406.

[157] Holanda, J., Maior, D. S., Azevedo, A., and Rezende, S. M., **2018**, Nature Physics, 14(5), pp. 500-506.

[158] Kovalenko, O., Pezeril, T., and Temnov, V. V., **2013**, Physical Review Letters, 110(26), p. 266602.

[159] Graves, C. E., Reid, A. H., Wang, T., Wu, B., de Jong, S., Vahaplar, K., Radu, I., Bernstein, D. P., Messerschmidt, M., Müller, L., Coffee, R., Bionta, M., Epp, S. W., Hartmann, R., Kimmel, N., Hauser, G., Hartmann, A., Holl, P., Gorke, H., Mentink, J. H., Tsukamoto, A., Fognini, A., Turner, J. J., Schlotter, W. F., Rolles, D., Soltau, H., Strüder, L., Acremann, Y., Kimel, A. V., Kirilyuk, A., Rasing, T., Stöhr, J., Scherz, A. O., and Dürr, H. A., **2013**, Nature Materials, 12(4), pp. 293-298.

[160] Wohlhüter, P., Bryan, M. T., Warnicke, P., Gliga, S., Stevenson, S. E., Heldt, G., Saharan, L., Suszka, A. K., Moutafis, C., Chopdekar, R. V., Raabe, J., Thomson, T., Hrkac, G., and Heyderman, L. J., **2015**, Nature Communications, 6(1), p. 7836.

[161] Stupakiewicz, A., Szerenos, K., Afanasiev, D., Kirilyuk, A., and Kimel, A. V., **2017**, Nature, 542(7639), pp. 71-74.

[162] Vodungbo, B., Gautier, J., Lambert, G., Sardinha, A. B., Lozano, M., Sebban, S., Ducousso, M., Boutu, W., Li, K., Tudu, B., Tortarolo, M., Hawaldar, R., Delaunay, R., López-Flores, V., Arabski, J., Boeglin, C., Merdji, H., Zeitoun, P., and Lüning, J., **2012**, Nature Communications, 3(1), p. 999.

[163] Yang, Y., Wilson, R. B., Gorchon, J., Lambert, C.-H., Salahuddin, S., and Bokor, J., **2017**, Science Advances, 3(11), p. e1603117.

[164] Roy, K., Bandyopadhyay, S., and Atulasimha, J., **2011**, Applied Physics Letters, 99(6), p. 063108.

[165] Lei, N., Devolder, T., Agnus, G., Aubert, P., Daniel, L., Kim, J.-V., Zhao, W., Trypiniotis, T., Cowburn, R. P., Chappert, C., Ravelosona, D., and Lecoeur, P., **2013**, Nature Communications, 4(1), p. 1378.

[166] De Ranieri, E., Roy, P. E., Fang, D., Vehsthedt, E. K., Irvine, A. C., Heiss, D., Casiraghi, A., Campion, R. P., Gallagher, B. L., Jungwirth, T., and Wunderlich, J., **2013**, Nature Materials, 12(9), pp. 808-814.

[167] Zhao, Z., Jamali, M., D'Souza, N., Zhang, D., Bandyopadhyay, S., Atulasimha, J., and Wang, J.-P., **2016**, Applied Physics Letters, 109(9), p. 092403.

[168] Malinowski, G., Dalla Longa, F., Rietjens, J. H. H., Paluskar, P. V., Huijink, R., Swagten, H. J. M., and Koopmans, B., **2008**, Nature Physics, 4(11), pp. 855-858.

[169] Bigot, J.-Y., Vomir, M., and Beaurepaire, E., **2009**, Nature Physics, 5(7), pp. 515-520.

[170] Zhang, G. P., Hübner, W., Lefkidis, G., Bai, Y., and George, T. F., **2009**, Nature Physics, 5(7), pp. 499-502.

[171] Müller, G. M., Walowski, J., Djordjevic, M., Miao, G.-X., Gupta, A., Ramos, A. V., Gehrke, K., Moshnyaga, V., Samwer, K., Schmalhorst, J., Thomas, A., Hütten, A., Reiss, G., Moodera, J. S., and Münzenberg, M., **2009**, Nature Materials, 8(1), pp. 56-61.

[172] Koopmans, B., Malinowski, G., Dalla Longa, F., Steiauf, D., Fähnle, M., Roth, T., Cinchetti, M., and Aeschlimann, M., **2010**, Nature Materials, 9, pp. 259-265.

[173] Eschenlohr, A., Battiato, M., Maldonado, P., Pontius, N., Kachel, T., Holldack, K., Mitzner, R., Föhlisch, A., Oppeneer, P. M., and Stamm, C., **2013**, Nature Materials, 12(4), pp. 332-336.

[174] Scherbakov, A. V., Salasyuk, A. S., Akimov, A. V., Liu, X., Bombeck, M., Brüggemann, C., Yakovlev, D. R., Sapega, V. F., Furdyna, J. K., and Bayer, M., **2010**, Physical Review Letters, 105(11), p. 117204.

[175] Thevenard, L., Peronne, E., Gourdon, C., Testelin, C., Cubukcu, M., Charron, E., Vincent, S., Lemaître, A., and Perrin, B., **2010**, Physical Review B, 82(10), p. 104422.

[176] Bombeck, M., Jäger, J. V., Scherbakov, A. V., Linnik, T., Yakovlev, D. R., Liu, X., Furdyna, J. K., Akimov, A. V., and Bayer, M., **2013**, Physical Review B, 87(6), p. 060302.

[177] Bombeck, M., Salasyuk, A. S., Glavin, B. A., Scherbakov, A. V., Brüggemann, C., Yakovlev, D. R., Sapega, V. F., Liu, X., Furdyna, J. K., Akimov, A. V., and Bayer, M., **2012**, Physical Review B, 85(19), p. 195324.

[178] Thevenard, L., Gourdon, C., Prieur, J. Y., von Bardeleben, H. J., Vincent, S., Becerra, L., Largeau, L., and Duquesne, J. Y., **2014**, Physical Review B, 90(9), p. 094401.

[179] Deb, M., Popova, E., Hehn, M., Keller, N., Mangin, S., and Malinowski, G., **2018**, Physical Review B, 98(17), p. 174407.

[180] Jamali, M., Narayanapillai, K., Qiu, X., Loong, L. M., Manchon, A., and Yang, H., **2013**, Physical Review Letters, 111(24), p. 246602.

[181] Pal, S., Klos, J. W., Das, K., Hellwig, O., Gruszecki, P., Krawczyk, M., and Barman, A., **2014**, Applied Physics Letters, 105(16), p. 162408.

[182] Pal, S., Polley, D., Mitra, R. K., and Barman, A., **2015**, Solid State Communications, 221, pp. 50-54.

[183] Gilbert, D. A., Maranville, B. B., Balk, A. L., Kirby, B. J., Fischer, P., Pierce, D. T., Unguris, J., Borchers, J. A., and Liu, K., **2015**, Nature Communications, 6(1), p. 8462.

[184] Chesnel, K., Safsten, A., Rytting, M., and Fullerton, E. E., **2016**, Nature Communications, 7(1), p. 11648.

[185] Hashimoto, S., Ochiai, Y., and Aso, K., **1989**, Japanese Journal of Applied Physics, 28(Part 1, No. 9), pp. 1596-1599.

[186] Schelp, L. F., Viegas, A. D. C., Carara, M., and Schmidt, J. E., **1995**, Journal of Magnetism and Magnetic Materials, 139(1), pp. 59-64.

[187] Chen, J.-Y., Zhu, J., Zhang, D., Lattery, D. M., Li, M., Wang, J.-P., and Wang, X., **2016**, The Journal of Physical Chemistry Letters, 7(13), pp. 2328-2332.

[188] Berk, C., Jaris, M., Yang, W., Dhuey, S., Cabrini, S., and Schmidt, H., **2019**, Nature Communications, 10(1), p. 2652.

[189] Qu, T., and Victora, R. H., **2016**, Physical Review B, 93(22), p. 224426.

[190] Yuasa, S., Suzuki, Y., Katayama, T., and Ando, K., **2005**, Applied Physics Letters, 87(24), p. 242503.

[191] Liu, X., Zhang, W., Carter, M. J., and Xiao, G., **2011**, Journal of Applied Physics, 110(3), p. 033910.

[192] Xu, B. X., Liu, Z. J., Ji, R., Toh, Y. T., Hu, J. F., Li, J. M., Zhang, J., Ye, K. D., and Chia, C. W., **2012**, Journal of Applied Physics, 111(7), p. 07B701.

[193] Jiao, Y., Liu, Z., and Victora, R. H., **2015**, Journal of Applied Physics, 117(17), p. 17E317.

[194] Atxitia, U., and Chubykalo-Fesenko, O., **2011**, Physical Review B, 84(14), p. 144414.

[195] Zhao, Y., Song, Q., Yang, S.-H., Su, T., Yuan, W., Parkin, S. S. P., Shi, J., and Han, W., **2016**, Scientific Reports, 6(1), p. 22890.

[196] Richardson, D., Katz, S., Wang, J., Takahashi, Y. K., Srinivasan, K., Kalitsov, A., Hono, K., Ajan, A., and Wu, M., **2018**, Physical Review Applied, 10(5), p. 054046.

[197] Shima, H., Oikawa, K., Fujita, A., Fukamichi, K., Ishida, K., and Sakuma, A., **2004**, Physical Review B, 70(22), p. 224408.

[198] Stillrich, H., Menk, C., Frömter, R., and Oepen, H. P., **2009**, Journal of Applied Physics, 105(7), p. 07C308.

[199] Shaw, J. M., Nembach, H. T., Weiler, M., Silva, T. J., Schoen, M., Sun, J. Z., and Worledge, D. C., **2015**, IEEE Magnetics Letters, 6, pp. 1-4.

[200] Alzate, J. G., Amiri, P. K., Yu, G., Upadhyaya, P., Katine, J. A., Langer, J., Ocker, B., Krivorotov, I. N., and Wang, K. L., **2014**, Applied Physics Letters, 104(11), p. 112410.

[201] Nagasaka, K., Varga, L., Shimizu, Y., Eguchi, S., and Tanaka, A., **2000**, Journal of Applied Physics, 87(9), pp. 6433-6435.

[202] Rottmayer, R. E., Batra, S., Buechel, D., Challener, W. A., Hohlfeld, J., Kubota, Y., Li, L., Lu, B., Mihalcea, C., Mountfield, K., Pelhos, K., Peng, C., Rausch, T., Seigler, M. A., Weller, D., and Yang, X., **2006**, IEEE Transactions on Magnetics, 42(10), pp. 2417-2421.

[203] Greaves, S. J., Kanai, Y., and Muraoka, H., **2013**, IEEE Transactions on Magnetics, 49(6), pp. 2665-2670.

[204] ASRC, 2019, "ASTC Technology Roadmap," http://asrc.idema.org/documents-roadmap/.

[205] Victora, R. H., and Huang, P., **2013**, IEEE Transactions on Magnetics, 49(2), pp. 751-757.

[206] Evans, R. F. L., Fan, W. J., Chureemart, P., Ostler, T. A., Ellis, M. O. A., and Chantrell, R. W., **2014**, Journal of Physics: Condensed Matter, 26(10), p. 103202.

[207] Atxitia, U., Chubykalo-Fesenko, O., Kazantseva, N., Hinzke, D., Nowak, U., and Chantrell, R. W., **2007**, Applied Physics Letters, 91(23), p. 232507.

[208] Garanin, D. A., **1997**, Physical Review B, 55(5), pp. 3050-3057.

[209] Vogler, C., Abert, C., Bruckner, F., and Suess, D., **2014**, Physical Review B, 90(21), p. 214431.

[210] Varaprasad, B. S. D. C. S., Chen, M., Takahashi, Y. K., and Hono, K., **2013**, IEEE Transactions on Magnetics, 49(2), pp. 718-722.

[211] Hono, K., Takahashi, Y. K., Ju, G., Thiele, J.-U., Ajan, A., Yang, X., Ruiz, R., and Wan, L., **2018**, MRS Bulletin, 43(2), pp. 93-99.

[212] Papusoi, C., Jain, S., Admana, R., Ozdol, B., Ophus, C., Desai, M., and Acharya, R., **2017**, Journal of Physics D: Applied Physics, 50(28), p. 285003.

[213] Ho, H., Sharma, A. A., Ong, W.-L., Malen, J. A., Bain, J. A., and Zhu, J.-G., **2013**, Applied Physics Letters, 103(13), p. 131907.

[214] Chernyshov, A., Treves, D., Le, T., Zong, F., Ajan, A., and Acharya, R., **2014**, Journal of Applied Physics, 115(17), p. 17B735.

[215] Cahill, D. G., **2004**, Review of Scientific Instruments, 75(12), pp. 5119-5122.

[216] Ohtake, M., Ouchi, S., Kirino, F., and Futamoto, M., **2012**, Journal of Applied Physics, 111(7), p. 07A708.

[217] Miyata, N., Asami, H., Mizushima, T., and Sato, K., **1990**, Journal of the Physical Society of Japan, 59(5), pp. 1817-1824.

[218] Slack, G. A., **1962**, Physical Review, 126(2), pp. 427-441.

[219] Mryasov, O. N., Nowak, U., Guslienko, K. Y., and Chantrell, R. W., **2005**, Europhysics Letters, 69(5), pp. 805-811.

[220] Xu, X. G., Zhang, D. L., Li, X. Q., Bao, J., Jiang, Y., and Jalil, M. B. A., **2009**, Journal of Applied Physics, 106(12), p. 123902.

[221] You, C.-Y., **2013**, Applied Physics Letters, 103(4), p. 042402.

[222] Zhang, D.-L., Sun, C., Lv, Y., Schliep, K. B., Zhao, Z., Chen, J.-Y., Voyles, P. M., and Wang, J.-P., **2018**, Physical Review Applied, 9(4), p. 044028.

[223] Belmeguenai, M., Martin, T., Woltersdorf, G., Maier, M., and Bayreuther, G., **2007**, Physical Review B, 76(10), p. 104414.

[224] Stenning, G. B. G., Shelford, L. R., Cavill, S. A., Hoffmann, F., Haertinger, M., Hesjedal, T., Woltersdorf, G., Bowden, G. J., Gregory, S. A., Back, C. H., Groot, P. A. J. d., and Laan, G. v. d., **2015**, New Journal of Physics, 17(1), p. 013019.

[225] Ruderman, M. A., and Kittel, C., **1954**, Physical Review, 96(1), pp. 99-102.

[226] Kasuya, T., **1956**, Progress of Theoretical Physics, 16(1), pp. 45-57.

[227] Yosida, K., **1957**, Physical Review, 106(5), pp. 893-898.

[228] Parkin, S. S. P., and Mauri, D., **1991**, Physical Review B, 44(13), pp. 7131-7134.

[229] Bloemen, P. J. H., van Kesteren, H. W., Swagten, H. J. M., and de Jonge, W. J. M., **1994**, Physical Review B, 50(18), pp. 13505-13514.

[230] Mandal, R., Ogawa, D., Tamazawa, Y., Ishioka, K., Shima, T., Kato, T., Iwata, S., Takahashi, Y. K., Hirosawa, S., and Hono, K., **2018**, Journal of Magnetism and Magnetic Materials, 468, pp. 273-278.

[231] Wu, G., Chen, S., Lou, S., Liu, Y., Jin, Q. Y., and Zhang, Z., **2019**, Applied Physics Letters, 115(14), p. 142402.

[232] Layadi, A., **2002**, Physical Review B, 65(10), p. 104422.

APPENDIX A: CONVERTING THE LANDAU-LIFSHITZ-GILBERT EQUATION

This appendix will show how the Landau-Lifshitz equation and the Landau-Lifshitz-Gilbert Equation can be equal as discussed by Ref. [105]. We start with the LLG equation:

$$\frac{d\mathbf{M}}{dt} = -\gamma \mathbf{M} \times \mathbf{H}_{\text{eff}} + \frac{\alpha}{M_{\text{s}}} \mathbf{M} \times \frac{d\mathbf{M}}{dt}. \tag{A1}$$

Taking the cross product of both sides leaves:

$$\mathbf{M} \times \frac{d\mathbf{M}}{dt} = -\gamma \mathbf{M} \times \left(\mathbf{M} \times \mathbf{H}_{\text{eff}} \right) + \frac{\alpha}{M_{\text{s}}} \mathbf{M} \times \left(\mathbf{M} \times \frac{d\mathbf{M}}{dt} \right). \tag{A2}$$

Plugging Eq. A2 into Eq. A1 gives

$$\frac{d\mathbf{M}}{dt} = -\gamma \mathbf{M} \times \mathbf{H}_{\text{eff}} - \frac{\alpha\gamma}{M_{\text{s}}} \mathbf{M} \times \left(\mathbf{M} \times \mathbf{H}_{\text{eff}} \right) + \frac{\alpha^2}{M_{\text{s}}^2} \mathbf{M} \times \left(\mathbf{M} \times \frac{d\mathbf{M}}{dt} \right). \tag{A3}$$

From here, using the triple product identity, it can be shown:

$$\mathbf{M} \times \left(\mathbf{M} \times \frac{d\mathbf{M}}{dt} \right) = \mathbf{M} \left(\mathbf{M} \cdot \frac{d\mathbf{M}}{dt} \right) - \frac{d\mathbf{M}}{dt} \left(\mathbf{M} \cdot \mathbf{M} \right) = \mathbf{M} \left(\mathbf{M} \cdot \frac{d\mathbf{M}}{dt} \right) - \frac{d\mathbf{M}}{dt} M_{\text{s}}^2. \tag{A4}$$

To further simplify Eq. A4, take the dot product of Eq. A1.

$$\mathbf{M} \cdot \frac{d\mathbf{M}}{dt} = -\gamma \mathbf{M} \cdot \left(\mathbf{M} \times \mathbf{H}_{\text{eff}} \right) + \frac{\alpha}{M_{\text{s}}} \mathbf{M} \cdot \left(\mathbf{M} \times \frac{d\mathbf{M}}{dt} \right) \tag{A5}$$

Since the cross-product of two vectors is perpendicular to both vectors, $\mathbf{M} \cdot \left(\mathbf{M} \times \mathbf{H}_{\text{eff}} \right) = 0$. We can also use a scalar triple product identity to show that:

$$\mathbf{M} \cdot \left(\mathbf{M} \times \frac{d\mathbf{M}}{dt} \right) = \frac{d\mathbf{M}}{dt} \cdot \left(\mathbf{M} \times \mathbf{M} \right) = 0. \tag{A6}$$

Using Eqs. A5 and A6, Eq. A4 can be simplified:

$$\mathbf{M} \times \left(\mathbf{M} \times \frac{d\mathbf{M}}{dt} \right) = -\frac{d\mathbf{M}}{dt} M_{\text{s}}^2. \tag{A7}$$

Plugging Eq. A7 into Eq. A3 leaves

$$\frac{d\mathbf{M}}{dt} = -\gamma \mathbf{M} \times \mathbf{H}_{\text{eff}} - \frac{\alpha\gamma}{M_{\text{s}}} \mathbf{M} \times \left(\mathbf{M} \times \mathbf{H}_{\text{eff}} \right) - \alpha^2 \frac{d\mathbf{M}}{dt}. \tag{A8}$$

To get this into the form of the LLG, separate the time derivatives and cross products.

$$\left(1 + \alpha^2 \right) \frac{d\mathbf{M}}{dt} = -\gamma \mathbf{M} \times \mathbf{H}_{\text{eff}} - \frac{\alpha\gamma}{M_{\text{s}}} \mathbf{M} \times \left(\mathbf{M} \times \mathbf{H}_{\text{eff}} \right) \tag{A9}$$

Finally, if we define a new reduced gyromagnetic ratio

$$\gamma' = \frac{\gamma}{1+\alpha^2}, \qquad \text{A10}$$

then Eq. A9 simplifies to the Landau-Lifshitz equation.

$$\frac{d\mathbf{M}}{dt} = -\gamma'\mathbf{M}\times\mathbf{H}_{\text{eff}} - \frac{\alpha\gamma'}{M_{\text{s}}}\mathbf{M}\times\left(\mathbf{M}\times\mathbf{H}_{\text{eff}}\right). \qquad \text{A11}$$

APPENDIX B: SMIT-SUHL APPROACH TO FERROMAGNETIC RESONANCE

As with most complex systems, it is often useful to make some simplifying assumptions to develop a concept or simplified model of the behavior. Here, we consider the response of the magnetization to a small perturbation away from equilibrium.

To determine the resonance condition for the LL equation (Eq. 2.7), we begin by defining our coordinate system as shown in Fig. B1. We can describe the magnetization in either a Cartesian coordinate system (with the *z*-axis defined as parallel to the surface normal of the magnetic thin film) or a spherical coordinate system using the inclination angle θ (from the z-axis) and the azimuthal angle φ (from the *x*-axis). The spherical coordinate system is often used for convenience when deriving analytical solutions.

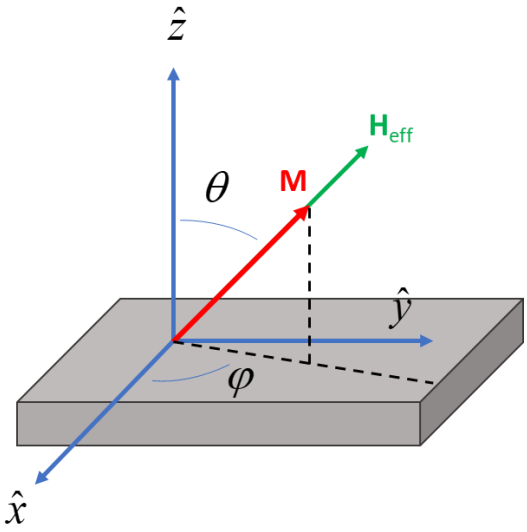

Figure B1. Coordinate system for the magnetization in thin films.

At equilibrium, the two vectors **M** and $\mathbf{H}_{\text{eff}}$ are aligned and are given by Eqs. B1 and B1 in Cartesian coordinates and B3 and B4 in spherical coordinates.

$$\mathbf{M} = M_s \begin{pmatrix} \sin(\theta_0)\cos(\varphi_0) \\ \sin(\theta_0)\sin(\varphi_0) \\ \cos(\theta_0) \end{pmatrix} = \begin{pmatrix} M_x \\ M_y \\ M_z \end{pmatrix} \tag{B1}$$

$$\mathbf{H}_{\text{eff}} = \begin{pmatrix} -\dfrac{\partial F}{\partial M_x} \\ -\dfrac{\partial F}{\partial M_y} \\ -\dfrac{\partial F}{\partial M_z} \end{pmatrix} = \begin{pmatrix} H_x \\ H_y \\ H_z \end{pmatrix} \tag{B2}$$

$$\mathbf{M} = \begin{pmatrix} M_s \\ \theta_0 \\ \varphi_0 \end{pmatrix} \tag{B3}$$

$$\mathbf{H}_{\text{eff}} = \begin{pmatrix} H_x \sin(\theta_0)\cos(\varphi_0) + H_y \sin(\theta_0)\sin(\varphi_0) + H_z \cos(\theta_0) \\ H_x \cos(\theta_0)\cos(\varphi_0) + H_y \cos(\theta_0)\sin(\varphi_0) + H_z \sin(\theta_0) \\ -H_x \sin(\varphi_0) + H_y \cos(\varphi_0) \end{pmatrix} = \begin{pmatrix} -\dfrac{\partial F}{\partial M_s} \\ -\dfrac{1}{M_s}\dfrac{\partial F}{\partial \theta} \\ -\dfrac{1}{M_s \sin(\theta_0)}\dfrac{\partial F}{\partial \varphi} \end{pmatrix} = \begin{pmatrix} H_r \\ H_\theta \\ H_\varphi \end{pmatrix} \tag{B4}$$

The equilibrium angles are defined as θ_0 and φ_0, which is where the magnetic free energy density F is minimized. If we move the magnetization vector out of equilibrium by some angle ($\Delta\theta$ and $\Delta\varphi$), we see that the cross-product in the LLG equation is no longer zero. To solve for the dynamics, it is beneficial to create a new spherical coordinate system such that the angles are defined with respect to **M**, i.e. the vectors become:

$$\mathbf{M} = \begin{pmatrix} M_s \\ 0 \\ 0 \end{pmatrix} \tag{B5}$$

$$\mathbf{H}_{\text{eff}} = \begin{pmatrix} H_r \\ H_\theta\big|_{\theta_0+\Delta\theta} \\ H_\varphi\big|_{\varphi_0+\Delta\varphi} \end{pmatrix} \equiv \begin{pmatrix} H_r \\ H_\theta^{'} \\ H_\varphi^{'} \end{pmatrix}. \tag{B6}$$

The cross-product calculations now become trivial:

$$\mathbf{M} \times \mathbf{H}_{\text{eff}} = -M_s H_\varphi^{'} \hat{\theta} + M_s H_\theta^{'} \hat{\varphi} \tag{B7}$$

$$\mathbf{M} \times (\mathbf{M} \times \mathbf{H}_{\text{eff}}) = -M_s^2 H_\theta^{'} \hat{\theta} - M_s^2 H_\varphi^{'} \hat{\varphi}. \tag{B8}$$

A derivative in spherical coordinates is necessary to calculate the left side of Eq. 2.7, assuming that the saturation magnetization is not changing with time.

$$\frac{d\mathbf{M}}{dt} = \frac{dM_s}{dt}\hat{r} + M_s \frac{d\theta}{dt}\hat{\theta} + M_s \sin(\theta_0)\frac{d\varphi}{dt}\hat{\varphi} = M_s\left(\dot{\theta}\hat{\theta} + \sin(\theta_0)\dot{\varphi}\hat{\varphi}\right) \tag{B9}$$

This assumption will result in the limitation of the application of this equation and makes the Landau-Lifshitz-Bloch (LLB) equation more applicable to TR-MOKE measurements (discussed in Appendix D). Combining Eqs. 2.7, B7, B8, and B9 results in two coupled differential equations of motion.

$$\dot{\theta} = \gamma' H_\varphi^{'} + \alpha\gamma' H_\theta^{'} \tag{B10}$$

$$\dot{\varphi} = \frac{1}{\sin(\theta_0)}\left(-\gamma' H_\theta' + \alpha\gamma' H_\varphi'\right) \tag{B11}$$

The derivatives of the magnetic free energy can then be plugged into Eqs. B10 and B11. With the small angle assumption made earlier, we can approximate the free energy density using a Taylor series expansion.

$$\frac{\partial F}{\partial \theta} \approx \left.\frac{\partial F}{\partial \theta}\right|_{\theta_0,\varphi_0} + F_{\theta\theta}\Delta\theta + F_{\theta\varphi}\Delta\varphi = F_{\theta\theta}\Delta\theta + F_{\theta\varphi}\Delta\varphi \tag{B12}$$

$$\frac{\partial F}{\partial \varphi} \approx \left.\frac{\partial F}{\partial \varphi}\right|_{\theta_0,\varphi_0} + F_{\theta\varphi}\Delta\theta + F_{\varphi\varphi}\Delta\varphi = F_{\theta\varphi}\Delta\theta + F_{\varphi\varphi}\Delta\varphi \tag{B13}$$

where

$$F_{x_i x_j} \equiv \frac{\partial^2 F}{\partial x_i \partial x_j}. \tag{B14}$$

Using this approximation, Eqs. B10 and B11 can be put into matrix form as shown in Eq. B15.

$$\begin{bmatrix}\dot{\theta}\\ \dot{\varphi}\end{bmatrix} = \begin{bmatrix} -\frac{\gamma'}{M_s}\frac{F_{\theta\varphi}}{\sin(\theta_0)} - \frac{\alpha\gamma'}{M_s}F_{\theta\theta} & -\frac{\gamma'}{M_s}\frac{F_{\varphi\varphi}}{\sin(\theta_0)} - \frac{\alpha\gamma'}{M_s}F_{\theta\varphi} \\ \frac{\gamma'}{M_s}\frac{F_{\theta\theta}}{\sin(\theta_0)} - \frac{\alpha\gamma'}{M_s}\frac{F_{\theta\varphi}}{\sin^2(\theta_0)} & \frac{\gamma'}{M_s}\frac{F_{\theta\varphi}}{\sin(\theta_0)} - \frac{\alpha\gamma'}{M_s}\frac{F_{\varphi\varphi}}{\sin^2(\theta_0)} \end{bmatrix}\begin{bmatrix}\Delta\theta\\ \Delta\varphi\end{bmatrix} \tag{B15}$$

Because this is a first order differential equation, we will assume the solutions to be:

$$\theta = C_1 \exp(i\omega t - \eta t) \equiv C_1 \exp(i\lambda t) \tag{B16}$$

$$\varphi = C_2 \exp(i\omega t - \eta t) \equiv C_2 \exp(i\lambda t) \tag{B17}$$

where the variable λ contains a real and imaginary part corresponding to the resonance frequency (ω) and the inverse relaxation time (η) respectively.

This now becomes eigenvalue (λ) and eigenvector (C_1, C_2) problem. Plugging our assumed solutions (Eqs. B16 and B17) into Eq. B15 will result in:

$$\begin{bmatrix} -\frac{\gamma'}{M_s}\frac{F_{\theta\varphi}}{\sin(\theta_0)} - \frac{\alpha\gamma'}{M_s}F_{\theta\theta} - i\lambda & -\frac{\gamma'}{M_s}\frac{F_{\varphi\varphi}}{\sin(\theta_0)} - \frac{\alpha\gamma'}{M_s}F_{\theta\varphi} \\ \frac{\gamma'}{M_s}\frac{F_{\theta\theta}}{\sin(\theta_0)} - \frac{\alpha\gamma'}{M_s}\frac{F_{\theta\varphi}}{\sin^2(\theta_0)} & \frac{\gamma'}{M_s}\frac{F_{\theta\varphi}}{\sin(\theta_0)} - \frac{\alpha\gamma'}{M_s}\frac{F_{\varphi\varphi}}{\sin^2(\theta_0)} - i\lambda \end{bmatrix}\begin{bmatrix}\Delta\theta\\ \Delta\varphi\end{bmatrix} = \begin{bmatrix}0\\0\end{bmatrix}. \tag{B18}$$

The meaningful solutions will occur when the determinant of this matrix is equal to 0. Calculating the determinant and solving for λ will result in:

$$\lambda = i\eta_0 \pm \sqrt{\left(1+\alpha^2\right)\omega_0^2 - \eta_0^2} \qquad \text{B19}$$

where ω_0 is the resonance frequency for the case without damping, which is given by Eq. B20 and η_0 is the inverse relaxation time given by Eq. B21. Note, that only the positive solution provides a physically meaningful result.

$$\omega_0 = \gamma' \sqrt{H_1 H_2 - H_3^2} \qquad \text{B20}$$

$$\eta_0 = \frac{\alpha\gamma'}{2}\left(H_1 + H_2\right) \qquad \text{B21}$$

Here we have adopted the use of commonly accepted symbols to simplify these equations, which are defined as:

$$H_1 = \frac{1}{M_s} F_{\theta\theta} \qquad \text{B22}$$

$$H_2 = \frac{1}{M_s \sin^2\left(\theta_0\right)} F_{\varphi\varphi} \qquad \text{B23}$$

$$H_3 = \frac{1}{M_s \sin\left(\theta_0\right)} F_{\theta\varphi}\,. \qquad \text{B24}$$

Based on this solution for λ, we can see:

$$\mathrm{Re}\{\lambda\} = \omega = \sqrt{\left(1+\alpha^2\right)\omega_0^2 - \eta_0^2} \qquad \text{B25}$$

$$\mathrm{Im}\{\lambda\} = \eta = \eta_0\,. \qquad \text{B26}$$

This solution will simplify to the resonance frequency for a system without damping if $\alpha = 0$. In fact, the resonance frequency will barely change as long as $\alpha << 1$, which is the case for most materials. To illustrate this, Figure B2 shows the calculated resonance frequency for an arbitrary sample with perpendicular magnetic anisotropy ($H_{k,eff}$ = 5 kOe) and a few different magnitudes of damping (α = 0, 0.01, 0.1, 1). Notice that if the damping becomes too high, there is a significant field region near $H_{k,eff}$ where Re (λ) = 0 (i.e. there is no allowable precessional mode, ω = 0) because the system is over-damped.

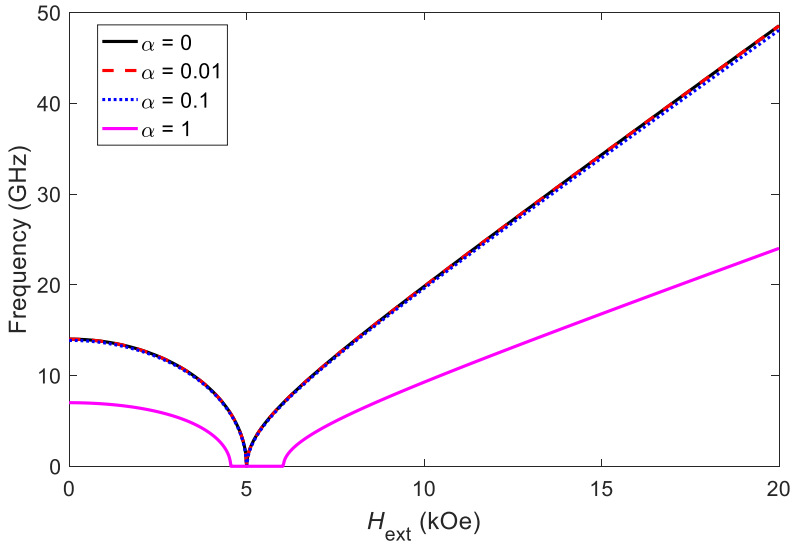

Figure B2. The Resonance frequency for a sample with $H_{k,eff}$ = 5 kOe and varying values of damping.

APPENDIX C: TWO-MAGNON SCATTERING DERIVATION

Like most aspects of magnetism, start by defining the energy of the system. Because the existence of magnons requires the existence of multiple magnetizations, uniform magnetization can no longer be assumed. The total energy of this system is the sum of the Zeeman energy, the demagnetizing energy, the exchange energy, and the anisotropy energy.

$$E = E_Z + E_d + E_{ex} + E_a \tag{C1}$$

$$E = -\int_V \mathbf{M}\cdot\mathbf{H}_{ext}\,d^3\mathbf{r} - \frac{1}{2}\int_V \mathbf{M}\cdot\mathbf{H}_d\,d^3\mathbf{r} + \frac{A}{M_s^2}\int_V \left[\left|\nabla\cdot\mathbf{M}\right|^2\right]d^3\mathbf{r} - \int_V \left[\left(\frac{\left|\mathbf{M}\cdot z\right|^2}{M_s^2}\right)\left(K_{u,1}+2K_{u,2}\right) - \left(\frac{\left|\mathbf{M}\cdot z\right|^4}{M_s^4}\right)K_{u,2}\right]d^3\mathbf{r} \tag{C2}$$

where **r** is a vector with origin at 0,0,0 that ends at a location in *x*,*y*,*z* space. Integrating over **r** indicates integration over the volume.

We will begin by defining our coordinate system:

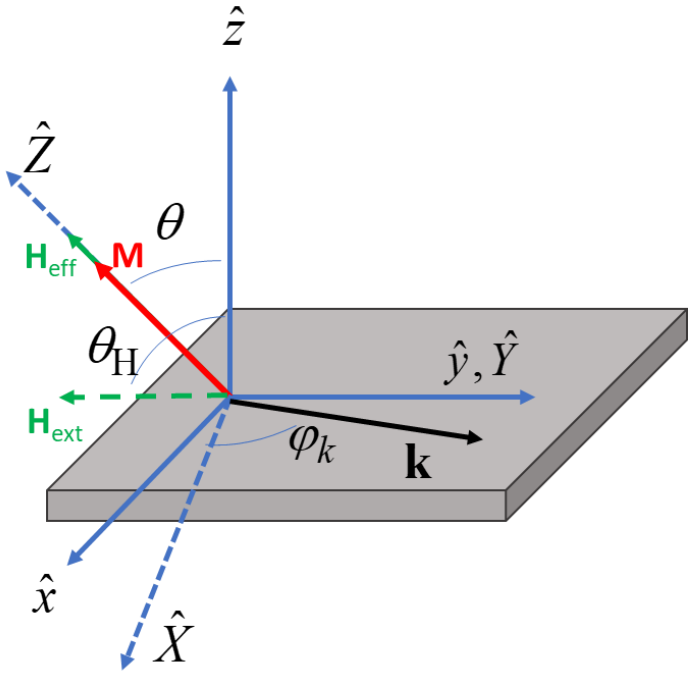

The global coordinate system (*x*, *y*, *z*) is defined such that the *z*-axis is through plane. The local coordinate system (*X*, *Y*, *Z*) is simply a transform of the global system such that the *Z*-axis is defined as the equilibrium direction of the magnetization. By doing this, we can define the magnetization in terms of two components that vary in time (M_X, M_Y) and one that doesn't (M_Z) which simplifies the derivations.

$$\mathbf{M}(\mathbf{r}) = M_Z(\mathbf{r})\hat{Z} + m_X(\mathbf{r})\hat{Z} + m_Y(\mathbf{r})\hat{Y} = M_Z(\mathbf{r})\hat{Z} + \mathbf{m}(\mathbf{r}) \tag{C3}$$

We need to allow for a variation in these vectors as the spin waves propagate in space, but we must also force the total magnetization to remain constant with a value of M_s.

$$M_Z^2 + \mathbf{m}^2 = M_s^2 \tag{C4}$$

The *m* term will be made of small oscillations caused by the spin waves which will cause a change in M_Z, or in other words:

$$M_Z = \sqrt{M_s^2 - m^2} = M_s\sqrt{1-\frac{m^2}{M_s^2}}\,. \tag{C5}$$

This form is only going to complicate things, and because *m* should be small, we will use a Taylor series expansion as an approximation:

$$M_Z = M_s\sqrt{1-\frac{m^2}{M_s^2}} \approx M_s - \frac{m^2}{2M_s} \tag{C6}$$

We can now rewrite our magnetization vector **M** in terms that are uniform (0), linear (1), and quadratic (2) in terms of our perturbations, m.

$$\mathbf{M}(\mathbf{r}) = M^{(0)}(\mathbf{r}) + M^{(1)}(\mathbf{r}) + M^{(2)}(\mathbf{r}) = M_s\hat{Z} + m(\mathbf{r}) - \frac{m^2(\mathbf{r})}{2M_s}\hat{Z} \tag{C7}$$

Now we need to start calculating the energy (Eq. 2), but in order to do this, we want our magnetization to be in terms of the global coordinate system.

$$\mathbf{M}(\mathbf{r}) = \left(M_s\cos(\theta)\hat{z} + M_s\sin(\theta)\hat{x}\right) + \left(m_X\cos(\theta)\hat{x} - m_X\sin(\theta)\hat{z} + m_Y\hat{y}\right) - \left(\frac{m^2}{2M_s}\left[\cos(\theta)\hat{z} + \sin(\theta)\hat{x}\right]\right) \tag{C8}$$

Start by finding the Zeeman energy:

$$E_Z = -\int_V \mathbf{M}\cdot\mathbf{H}_{ext}d^3\mathbf{r} = -\int_V \mathbf{M}^{(0)}\cdot\mathbf{H}_{ext}d^3\mathbf{r} - \int_V \mathbf{M}^{(1)}\cdot\mathbf{H}_{ext}d^3\mathbf{r} - \int_V \mathbf{M}^{(2)}\cdot\mathbf{H}_{ext}d^3\mathbf{r} \tag{C9}$$

$$-\int_V \mathbf{M}^{(0)}\cdot\mathbf{H}_{ext}d^3\mathbf{r} = -M_sH_{\text{ext}}\left[\sin(\theta)\sin(\theta_H) + \cos(\theta)\cos(\theta_H)\right]\int_V d^3\mathbf{r} = -VM_sH_{\text{ext}}\cos(\theta-\theta_H) \tag{C10}$$

$$-\int_V \mathbf{M}^{(1)}\cdot\mathbf{H}_{ext}d^3\mathbf{r} = -H_{\text{ext}}\left[\cos(\theta)\sin(\theta_H) - \sin(\theta)\cos(\theta_H)\right]\int_V m_X\,d^3\mathbf{r} = -H_{\text{ext}}\sin(\theta_H-\theta)\int_V m_X\,d^3\mathbf{r} \tag{C11}$$

$$-\int_V \mathbf{M}^{(2)}\cdot\mathbf{H}_{ext}d^3\mathbf{r} = \frac{H_{\text{ext}}\cos(\theta_H-\theta)}{2M_s}\int_V m^2(\mathbf{r})d^3\mathbf{r} \tag{C12}$$

Because the static energy (0 order) term has nothing to do with dynamics, we will not include it.

$$E_Z = -\int_V \mathbf{M}\cdot\mathbf{H}_{ext}\,d^3\mathbf{r} = -H_{\text{ext}}\sin\left(\theta_{\text{H}}-\theta\right)\int_V m_X\,d^3\mathbf{r} + \frac{H_{\text{ext}}\cos\left(\theta_{\text{H}}-\theta\right)}{2M_{\text{s}}}\int_V m^2\left(\mathbf{r}\right)d^3\mathbf{r} \qquad \text{C13}$$

We will redefine the magnetization variables in terms of a Fourier series to rewrite the energy.

$$m_{X,Y}\left(\mathbf{r}\right) = \frac{1}{d}\int_{-d/2}^{d/2} m_{X,Y}\left(\mathbf{r}\right)dz = \sum_{\mathbf{k}} m_{X,Y}\left(\mathbf{k}\right)\exp\left(i\mathbf{k}\cdot\mathbf{r}\right) \qquad \text{C14}$$

$$E_Z = -H_{\text{ext}}\sin\left(\theta_{\text{H}}-\theta\right)\sum_{\mathbf{k}} m_X + \frac{H_{\text{ext}}\cos\left(\theta_{\text{H}}-\theta\right)}{2M_{\text{s}}}\sum_{\mathbf{k}}\left(m_X m_X^* + m_Y m_Y^*\right) \qquad \text{C15}$$

The next part is the internal demagnetizing field. First, treat the field to be a static, linear, and quadratic term, then:

$$\mathbf{M}\cdot\mathbf{H}_{\text{d}} = \left[\mathbf{M}^{(0)}+\mathbf{M}^{(1)}+\mathbf{M}^{(2)}\right]\cdot\left[\mathbf{H}_{\text{d}}^{(0)}+\mathbf{H}_{\text{d}}^{(1)}+\mathbf{H}_{\text{d}}^{(2)}\right] \qquad \text{C16}$$

$$\mathbf{M}\cdot\mathbf{H}_{\text{d}} = \left[\mathbf{M}^{(0)}+2\mathbf{M}^{(1)}+2\mathbf{M}^{(2)}\right]\cdot\mathbf{H}_{\text{d}}^{(0)} + \mathbf{M}^{(1)}\cdot\mathbf{H}_{\text{d}}^{(1)} + \left[2\mathbf{M}^{(1)}+\mathbf{M}^{(2)}\right]\cdot\mathbf{H}_{\text{d}}^{(2)} \qquad \text{C17}$$

We will only use the 0th and 1st order demagnetizing field terms:

$$\mathbf{M}\cdot\mathbf{H}_{\text{d}} \approx \left[\mathbf{M}^{(0)}+2\mathbf{M}^{(1)}+2\mathbf{M}^{(2)}\right]\cdot\mathbf{H}_{\text{d}}^{(0)} + \mathbf{M}^{(1)}\cdot\mathbf{H}_{\text{d}}^{(1)} \qquad \text{C18}$$

We will use the definition:

$$\mathbf{H}_{\text{d}}^{(0)} = -4\pi M_{\text{s}}\cos\left(\theta\right)\hat{z} \qquad \text{C19}$$

Applying this and the above equation, we can get:

$$E_{\text{d}} = -\frac{1}{2}\int_V \mathbf{M}\cdot\mathbf{H}_{\text{d}}\,d^3\mathbf{r} = 2\pi M_{\text{s}}\cos\left(\theta\right)\int_V\left[M_{\text{s}}\cos\left(\theta\right) - 2m_X\sin\left(\theta\right) - \frac{m^2}{M_{\text{s}}}\cos\left(\theta\right)\right]d^3\mathbf{r} - \frac{1}{2}\int_V \mathbf{M}^{(1)}\cdot\mathbf{H}_{\text{d}}^{(1)}\,d^3\mathbf{r} \qquad \text{C20}$$

Make a few simplifications:

$$E_{\text{d}} = 2\pi M_{\text{s}}^2 V\cos^2\left(\theta\right) - 2\pi M_{\text{s}}\sin\left(2\theta\right)\int_V m_X\,d^3\mathbf{r} - 2\pi\cos^2\left(\theta\right)\int_V \frac{m^2}{M_{\text{s}}}\,d^3\mathbf{r} - \frac{1}{2}\int_V \mathbf{M}^{(1)}\cdot\mathbf{H}_{\text{d}}^{(1)}\,d^3\mathbf{r} \qquad \text{C21}$$

Use a Fourier transform to convert the terms "*m*" in space to "*m*" in terms of wavevector (k).

This is basically showing that the magnetization through plane is averaged through the thickness, (i.e., the magnetization is uniform in plane). We can then change the demagnetizing energy (ignoring the constant term) to:

$$E_{\mathrm{d}} = -2\pi M_{\mathrm{s}} \sin(2\theta) \sum_{\mathbf{k}} m_X - 2\pi \cos^2(\theta) \sum_{\mathbf{k}} \left(m_X m_X^* + m_Y m_Y^* \right) - \frac{1}{2} \int_V \mathbf{M}^{(1)} \cdot \mathbf{H}_{\mathrm{d}}^{(1)} d^3\mathbf{r} \qquad \text{C22}$$

The derivation of the linear demagnetizing field is very long.

Start with Maxwell's equations for magnetostatics:

$$\nabla \times \mathbf{H} = 0 \qquad \text{C23}$$

$$\nabla \cdot \mathbf{B} = 0 \qquad \text{C24}$$

The only way that the curl of a vector is always zero is if it is the gradient of a scalar potential (φ), so:

$$\mathbf{H}(\mathbf{r}) \propto \nabla \varphi(\mathbf{r}) \qquad \text{C25}$$

We will use the standard understanding that the field will go against the gradient of the potential, or:

$$\mathbf{H}(\mathbf{r}) = -\nabla \varphi(\mathbf{r}) \qquad \text{C26}$$

We know that the internal **B** field of a material is given by:

$$\mathbf{B} = \mathbf{H} + 4\pi \mathbf{M} \qquad \text{C27}$$

We will then plug this back into the 2nd magnetostatic equation:

$$\nabla \cdot \mathbf{B} = \nabla \cdot \mathbf{H} + 4\pi \nabla \cdot \mathbf{M} = 0 \qquad \text{C28}$$

This gives the result:

$$\nabla^2 \varphi = 4\pi \nabla \cdot \mathbf{M} \qquad \text{C29}$$

We can easily calculate the divergence of the magnetization vector based on previous results. We will restrict this only to the terms linear to **m**.

$$4\pi \nabla \cdot \mathbf{M}^{(1)}(\mathbf{r}) = 4\pi \left[\frac{\partial m_X(\mathbf{r})}{\partial x} \cos(\theta) + \frac{\partial m_Y(\mathbf{r})}{\partial y} - \frac{\partial m_X(\mathbf{r})}{\partial z} \sin(\theta) \right] \qquad \text{C30}$$

In the limits of a thin film, the magnetization does not vary through the depth of the material, so:

$$4\pi \nabla \cdot \mathbf{M}^{(1)} = 4\pi \left[\frac{\partial m_X}{\partial x} \cos(\theta) + \frac{\partial m_Y}{\partial y} \right] \qquad \text{C31}$$

We now have to solve for the Laplacian of the potential. We will do this by assuming that the film is an infinite plane with a finite thickness along the *z*-direction, and define it by:

$$\varphi(\mathbf{r}) = \sum_{\mathbf{k}} \varphi_{\mathbf{k}}(z) \exp(i\mathbf{k} \cdot \mathbf{r}) \qquad \text{C32}$$

Taking the Laplacian of this results in:

$$\nabla^2\varphi(\mathbf{r}) = -\sum_{\mathbf{k}} k^2 \varphi_{\mathbf{k}}(z)\exp(i\mathbf{k}\cdot\mathbf{r}) + 2i\sum_{\mathbf{k}} k_z \frac{\partial\varphi_{\mathbf{k}}(z)}{\partial z}\exp(i\mathbf{k}\cdot\mathbf{r}) + \sum_{\mathbf{k}} \frac{\partial^2\varphi_{\mathbf{k}}(z)}{\partial z^2}\exp(i\mathbf{k}\cdot\mathbf{r}) \quad \text{C33}$$

We will again make a thin-film assumption and assume that the propagation of magnons is not in the depth direction and is purely in plane. This means that $k_z \approx 0$, resulting in:

$$\nabla^2\varphi(\mathbf{r}) = -\sum_{\mathbf{k}} k^2 \varphi_{\mathbf{k}}(z)\exp(i\mathbf{k}\cdot\mathbf{r}) + \sum_{\mathbf{k}} \frac{\partial^2\varphi_{\mathbf{k}}(z)}{\partial z^2}\exp(i\mathbf{k}\cdot\mathbf{r}) \quad \text{C34}$$

We will also treat the magnetization here as a sum over all **k** vectors within the film.

$$\mathbf{M}^{(1)}(\mathbf{r}) = \sum_{\mathbf{k}} \mathbf{m}_{\mathbf{k}}(z)\exp(i\mathbf{k}\cdot\mathbf{r}) \quad \text{C35}$$

This results in:

$$4\pi\nabla\cdot\mathbf{M}^{(1)} = 4\pi i\sum_{\mathbf{k}}\left[k_x m_X(\mathbf{k})\cos(\theta) + k_y m_Y(\mathbf{k})\right]\exp(i\mathbf{k}\cdot\mathbf{r}) \quad \text{C36}$$

Combining these terms leaves:

$$-k^2\varphi_{\mathbf{k}}(z) + \frac{\partial^2\varphi_{\mathbf{k}}(z)}{\partial z^2} = f \quad \text{C37}$$

where:

$$f = 4\pi i\left[k_x m_X(\mathbf{k})\cos(\theta) + k_y m_Y(\mathbf{k})\right] \quad \text{C38}$$

Outside of the thin film, the magnetization goes to 0 and the potential must also go to zero at positive and negative infinity. We will treat this film with thickness d where 0 is halfway between the film and assume a solution where:

$$\varphi_{\mathbf{k}}(z) = \begin{cases} A\exp(-kz) & z > d/2 \\ a\exp(-kz) + b\exp(kz) - \dfrac{f}{k^2} & -d/2 \le z \le d/2 \\ B\exp(kz) & z < -d/2 \end{cases} \quad \text{C39}$$

We require that this term is continuous at the interfaces, which leads to:

$$A\exp\left(-\frac{kd}{2}\right) = a\exp\left(-\frac{kd}{2}\right) + b\exp\left(\frac{kd}{2}\right) - \frac{f}{k^2} \quad \text{C40}$$

Solving for A gives:

$$A = a + b\exp(kd) - \frac{f}{k^2}\exp\left(\frac{kd}{2}\right) \quad \text{C41}$$

Repeating this process for the other limit gives:

$$B = a\exp(kd) + b - \frac{f}{k^2}\exp\left(\frac{kd}{2}\right) \quad \text{C42}$$

The **B** field must also be continuous at the interface. This means that:

$$-\nabla\varphi + 4\pi m_z = -\nabla\varphi^{\pm} \quad \text{C43}$$

where the +/- corresponds to the top and bottom of the film. Following this boundary condition:

$$ka\exp\left(-\frac{kd}{2}\right) - kb\exp\left(\frac{kd}{2}\right) - 4\pi m_X \sin(\theta) = kA\exp\left(-\frac{kd}{2}\right) \quad \text{C44}$$

Solving for *A* gives:

$$A = a - b\exp(kd) - 4\pi m_X \sin(\theta)\exp\left(\frac{kd}{2}\right)/k \quad \text{C45}$$

We will use define a variable g such that:

$$g = -4\pi m_X \sin(\theta)/k \quad \text{C46}$$

Then *A* becomes:

$$A = a - b\exp(kd) + g\exp\left(\frac{kd}{2}\right) \quad \text{C47}$$

Repeating this process for the other limit gives:

$$ka\exp\left(\frac{kd}{2}\right) - kb\exp\left(-\frac{kd}{2}\right) - 4\pi m_X \sin(\theta) = -kB\exp\left(-\frac{kd}{2}\right) \quad \text{C48}$$

$$B = -a\exp(kd) + b - g\exp\left(\frac{kd}{2}\right) \quad \text{C49}$$

We can then solve for the two constants *a* and *b* by combining the equations above.

$$-a\exp(kd) + b - g\exp\left(\frac{kd}{2}\right) = a\exp(kd) + b - \frac{f}{k^2}\exp\left(\frac{kd}{2}\right) \quad \text{C50}$$

$$a = \frac{1}{2}\left[\frac{f}{k^2} - g\right]\exp\left(-\frac{kd}{2}\right) \quad \text{C51}$$

$$a - b\exp(kd) + g\exp\left(\frac{kd}{2}\right) = a + b\exp(kd) - \frac{f}{k^2}\exp\left(\frac{kd}{2}\right) \quad \text{C52}$$

$$b = \frac{1}{2}\left[\frac{f}{k^2} + g\right]\exp\left(-\frac{kd}{2}\right) \quad \text{C53}$$

These constants can then be plugged back in to find an equation for the potential within the film:

$$\varphi_{\mathbf{k}}(z) = \frac{1}{2}\left[\frac{f}{k^2} - g\right]\exp\left(-\frac{kd}{2}\right)\exp(-kz) + \frac{1}{2}\left[\frac{f}{k^2} + g\right]\exp\left(-\frac{kd}{2}\right)\exp(kz) - \frac{f}{k^2} \quad \text{C54}$$

This can be simplified using the identities for hyperbolic sine and cosine.

$$\varphi_{\mathbf{k}}(z) = \left[\cosh(kz)\exp\left(-\frac{kd}{2}\right) - 1\right]\frac{f}{k^2} + g\sinh(kz)\exp\left(-\frac{kd}{2}\right) \quad \text{C55}$$

While this provides the potential within the thickness in the film, it only works at a single location. To extend this into the entire film, plug this equation back into the original definition:

$$\varphi(\mathbf{r}) = \sum_{\mathbf{k}}\varphi_{\mathbf{k}}(z)\exp(i\mathbf{k}\cdot\mathbf{r}) = \sum_{\mathbf{k}}\left[\cosh(kz)\mathrm{e}^{-kd/2} - 1\right]\frac{f}{k^2}\exp(i\mathbf{k}\cdot\mathbf{r}) + g\sinh(kz)\mathrm{e}^{-kd/2}\exp(i\mathbf{k}\cdot\mathbf{r}) \quad \text{C56}$$

We can now find the demagnetizing field vector by taking the gradient:

$$H_{\mathrm{d},x}^{(1)} = -\frac{\partial\varphi}{\partial x} = -i\sum_{\mathbf{k}}\left[\cosh(kz)\mathrm{e}^{-kd/2} - 1\right]\frac{f}{k^2}k_x\exp(i\mathbf{k}\cdot\mathbf{r}) + gk_x\sinh(kz)\mathrm{e}^{-kd/2}\exp(i\mathbf{k}\cdot\mathbf{r}) \quad \text{C57}$$

$$H_{\mathrm{d,y}}^{(1)} = -\frac{\partial\varphi}{\partial y} = -i\sum_{\mathbf{k}}\left[\cosh(kz)\mathrm{e}^{-kd/2} - 1\right]\frac{f}{k^2}k_y\exp(i\mathbf{k}\cdot\mathbf{r}) + gk_y\sinh(kz)\mathrm{e}^{-kd/2}\exp(i\mathbf{k}\cdot\mathbf{r}) \quad \text{C58}$$

We can still use the thin film approximation and in this case, $\mathbf{k}$ is only made of k_x and k_y. In this case, we can ignore the derivative of the exponential term.

$$H_{\mathrm{d},z}^{(1)} = -\frac{\partial\varphi}{\partial z} = -\sum_{\mathbf{k}}\left[\sinh(kz)\mathrm{e}^{-kd/2}\frac{f}{k} + gk\cosh(kz)\mathrm{e}^{-kd/2}\right]\exp(i\mathbf{k}\cdot\mathbf{r}) \quad \text{C59}$$

Remember from previously that the definition of $\mathbf{M}^{(1)}$ is

$$\mathbf{M}^{(1)} = m_X\cos(\theta)\hat{x} + m_Y\hat{y} - m_X\sin(\theta)\hat{z} \quad \text{C60}$$

We can now integrate to solve for the integral. I used the symbolic integration function in MatLab here.

$$\begin{aligned}-\frac{1}{2}\int_V \mathbf{M}^{(1)}\cdot\mathbf{H}_{\mathrm{d}}^{(1)}d^3\mathbf{r} = -\sum_{\mathbf{k}}\frac{1}{2k^3}[&2gk^3m_X\sinh(kd/2)\sin(\theta) - 2ifk_xm_X\sinh(kd/2)\cos(\theta)\\ &- 2ifk_ym_Y\sinh(kd/2) + idfkk_ym_Y\exp(kd/2)\\ &+ idfkk_xm_X\exp(kd/2)\cos(\theta)]\exp(-kd/2)\exp(i\mathbf{k}\cdot\mathbf{r})\end{aligned} \quad \text{C61}$$

$$-\frac{1}{2}\int_V \mathbf{M}^{(1)}\cdot\mathbf{H}_{\mathrm{d}}^{(1)}d^3\mathbf{r} = -\frac{\sin(\theta)}{2d}\sum_{\mathbf{k}} gm_X\left(1-\mathrm{e}^{kd}\right)+ \\ \frac{i}{2}\sum_{\mathbf{k}}\left[\left(k_x m_X\cos(\theta)+k_y m_Y\right)\left(1-\mathrm{e}^{kd}\right)/kd - kd\left(k_y m_Y + k_x m_X\cos(\theta)\right)/kd\right]\frac{f}{k^2} \tag{C62}$$

$$-\frac{1}{2}\int_V \mathbf{M}^{(1)}\cdot\mathbf{H}_{\mathrm{d}}^{(1)}d^3\mathbf{r} = -\frac{\sin(\theta)}{2d}\sum_{\mathbf{k}} gm_X\left(1-\mathrm{e}^{kd}\right)+\frac{i}{2}\sum_{\mathbf{k}}\left(k_x m_X\cos(\theta)+k_y m_Y\right)\left[\frac{1-\mathrm{e}^{kd}}{kd}-1\right]\frac{f}{k^2} \tag{C63}$$

Because m_X and m_Y can be complex and the energy must be real, we have to change a few of these components:

$$-\frac{1}{2}\int_V \mathbf{M}^{(1)}\cdot\mathbf{H}_{\mathrm{d}}^{(1)}d^3\mathbf{r} = -\frac{\sin(\theta)}{2d}\sum_{\mathbf{k}} gm_X^*\left(1-\mathrm{e}^{kd}\right)+\frac{i}{2}\sum_{\mathbf{k}}\left(k_x m_X^*\cos(\theta)+k_y m_Y^*\right)\left[\frac{1-\mathrm{e}^{kd}}{kd}-1\right]\frac{f}{k^2} \tag{C64}$$

We will then reinsert the earlier definitions of *g* and *f*.

$$-\frac{1}{2}\int_V \mathbf{M}^{(1)}\cdot\mathbf{H}_{\mathrm{d}}^{(1)}d^3\mathbf{r} = 2\pi\sin^2(\theta)\sum_{\mathbf{k}} m_X m_X^*\frac{1-\mathrm{e}^{kd}}{kd} \\ -2\pi\sum_{\mathbf{k}}\frac{1}{k^2}\left(k_x^2 m_X m_X^*\cos^2(\theta)+k_y^2 m_Y m_Y^*+k_x k_y\cos(\theta)\left(m_X^* m_Y + m_X m_Y^*\right)\right)\left[\frac{1-\mathrm{e}^{kd}}{kd}-1\right] \tag{C65}$$

We can further simplify this by defining a new variable N_{k}:

$$N_k = \frac{1-\mathrm{e}^{-kd}}{kd} \tag{C66}$$

We will also make use of the angle of the wavevector from the *x*-axis, such that:

$$\cos(\varphi_k) = \frac{k_x}{k} \tag{C67}$$

$$\sin(\varphi_k) = \frac{k_y}{k} \tag{C68}$$

$$-\frac{1}{2}\int_V \mathbf{M}^{(1)}\cdot\mathbf{H}_{\mathrm{d}}^{(1)}d^3\mathbf{r} = 2\pi\sin^2(\theta)\sum_{\mathbf{k}} N_k m_X m_X^* \\ -2\pi\sum_{\mathbf{k}}\left(m_X m_X^*\cos^2(\varphi_k)\cos^2(\theta)+m_Y m_Y^*\sin^2(\varphi_k)\right)\left(N_k-1\right) \\ -2\pi\sum_{\mathbf{k}}\left(m_X^* m_Y + m_X m_Y^*\right)\sin(\varphi_k)\cos(\varphi_k)\cos(\theta)\left(N_k-1\right) \tag{C69}$$

Now this can be plugged back into the demagnetizing energy (Eq. C22):

$$
\begin{aligned}
E_{\mathrm{d}} = & -2\pi M_{\mathrm{s}} \sin(2\theta) \sum_{\mathbf{k}} m_X \\
& + \frac{1}{2M_{\mathrm{s}}} \sum_{\mathbf{k}} 2\pi M_{\mathrm{s}} \left(-2\cos^2(\theta) + 2N_k \sin^2(\theta) - 2(N_k - 1)\cos^2(\varphi_k)\cos^2(\theta) \right) m_X m_X^* \\
& + \frac{1}{2M_{\mathrm{s}}} \sum_{\mathbf{k}} 2\pi M_{\mathrm{s}} \left(-2\cos^2(\theta) - 2(N_k - 1)\sin^2(\varphi_k) \right) m_Y m_Y^* \\
& - \frac{1}{2M_{\mathrm{s}}} \sum_{\mathbf{k}} 2\pi M_{\mathrm{s}} (N_k - 1)\sin(2\varphi_k)\cos(\theta) \left(m_X m_Y^* + m_Y m_X^* \right)
\end{aligned}
\qquad \text{C70}
$$

We will now move on to calculating the exchange energy:

$$
E_{\mathrm{ex}} = \frac{A}{M_{\mathrm{s}}^2} \int_V \left[\left| \nabla \cdot \mathbf{M} \right|^2 \right] d^3\mathbf{r} \qquad \text{C71}
$$

I'm not sure about this one, but Landeros et al. ([52]) just assume that it is actually expressed as:

$$
E_{\mathrm{ex}} = \frac{A}{M_{\mathrm{s}}^2} \int_V \left[\left| \nabla m_X \right|^2 + \left| \nabla m_Y \right|^2 \right] d^3\mathbf{r} \qquad \text{C72}
$$

We will use the *k*-vector definitions of the magnetization components:

$$
m_{X,Y}(\mathbf{r}) = \sum_{\mathbf{k}} m_{X,Y}(\mathbf{k}) \exp(i\mathbf{k} \cdot \mathbf{r}) \qquad \text{C73}
$$

Taking the gradient of these components gives:

$$
\nabla m_{X,Y}(\mathbf{r}) = k \sum_{\mathbf{k}} m_{X,Y}(\mathbf{k}) \exp(i\mathbf{k} \cdot \mathbf{r}) \qquad \text{C74}
$$

Plugging this into the energy expression gives:

$$
E_{\mathrm{ex}} = \frac{A}{M_{\mathrm{s}}^2} \sum_{\mathbf{k}} k^2 \left(m_X m_X^* + m_Y m_Y^* \right) \qquad \text{C75}
$$

Transforming this into a form that is more consistent with other energy terms will give:

$$
E_{\mathrm{ex}} = \frac{1}{2M_{\mathrm{s}}} \sum_{\mathbf{k}} Dk^2 \left(m_X m_X^* + m_Y m_Y^* \right) \qquad \text{C76}
$$

where

$$
D = \frac{2A}{M_{\mathrm{s}}}. \qquad \text{C77}
$$

Finally, we will discuss the anisotropy terms:

$$
E_a = -\int_V \left[\left(\frac{\left| \mathbf{M} \cdot z \right|^2}{M_{\mathrm{s}}^2} \right) \left(K_{\mathrm{u},1} + 2K_{\mathrm{u},2} \right) - \left(\frac{\left| \mathbf{M} \cdot z \right|^4}{M_{\mathrm{s}}^4} \right) K_{\mathrm{u},2} \right] d^3\mathbf{r} \qquad \text{C78}
$$

Starting with the 2nd order terms, we get:

$$E_{a,2} = -\frac{1}{2M_\mathrm{s}}\left(\frac{2K_{\mathrm{u},1}}{M_\mathrm{s}} + \frac{4K_{\mathrm{u},2}}{M_\mathrm{s}}\right)\int_V M_z^2 d^3\mathbf{r} = -\frac{1}{2M_\mathrm{s}} H_{\mathrm{a},1}\int_V M_z^2 d^3\mathbf{r} \tag{C79}$$

Using our previous definition of M_z, we can see that the magnetization along the z-direction squared is:

$$\begin{aligned} M_z^2 = {} & M_\mathrm{s}^2\cos^2(\theta) - M_\mathrm{s} m_X \sin(2\theta) - \left(m_X^2 + m_Y^2\right)\cos^2(\theta) + m_X^2\sin^2(\theta) \\ & + \frac{m_X\left(m_X^2 + m_Y^2\right)}{2M_\mathrm{s}}\sin(2\theta) + \frac{\left(m_X^2 + m_Y^2\right)^2}{4M_\mathrm{s}^2}\cos^2(\theta) \end{aligned} \tag{C80}$$

We will treat the 3rd and 4th order terms here to be negligible and will also not use the constant term in our calculations, so:

$$E_{a,2} = -\frac{1}{2M_\mathrm{s}} H_{\mathrm{a},1}\int_V \left[-M_\mathrm{s} m_X \sin(2\theta) - \left(m_X^2 + m_Y^2\right)\cos^2(\theta) + m_X^2\sin^2(\theta)\right] d^3\mathbf{r} \tag{C81}$$

Following the process we have outlined before, this becomes:

$$E_{a,2} = \frac{1}{2M_\mathrm{s}} H_{\mathrm{a},1}\sum_{\mathbf{k}} M_\mathrm{s} m_X \sin(2\theta) + \frac{1}{2M_\mathrm{s}} H_{\mathrm{a},1}\cos(2\theta)\sum_{\mathbf{k}} m_X m_X^* + \frac{1}{2M_\mathrm{s}} H_{\mathrm{a},1}\cos^2(\theta)\sum_{\mathbf{k}} m_Y m_Y^* \tag{C82}$$

We can now repeat the past few steps for the 4th order anisotropy (2nd order uniaxial).

$$E_{a,4} = \frac{1}{2M_\mathrm{s}}\left(\frac{2K_{\mathrm{u},2}}{M_\mathrm{s}}\right)\frac{1}{M_\mathrm{s}^2}\int_V M_z^4 d^3\mathbf{r} = \frac{1}{2M_\mathrm{s}} H_{a,2}\frac{1}{M_\mathrm{s}^2}\int_V M_z^4 d^3\mathbf{r} \tag{C83}$$

As discussed previously, we only want the terms that are quadratic or lower order, so we can approximate:

$$M_z^4 \approx M_\mathrm{s}^4\cos^4(\theta) - 4M_\mathrm{s}^3 m_X\cos^3(\theta)\sin(\theta) - 4M_\mathrm{s}^3\frac{\left(m_X^2 + m_Y^2\right)}{2M_\mathrm{s}}\cos^4(\theta) + 6M_\mathrm{s}^2 m_X^2\sin^2(\theta)\cos^2(\theta) \tag{C84}$$

Plugging this in will give:

$$\begin{aligned} E_{a,4} = {} & \frac{1}{2M_\mathrm{s}} H_{a,2} M_\mathrm{s}^2\cos^4(\theta)\int_V d^3\mathbf{r} - \frac{1}{2M_\mathrm{s}} H_{a,2}\cos^3(\theta)\sin(\theta)\int_V 4M_\mathrm{s} m_X d^3\mathbf{r} \\ & + \frac{1}{2M_\mathrm{s}} H_{a,2}\int_V \left[-2\left(m_X^2 + m_Y^2\right)\cos^4(\theta) + 6m_X^2\sin^2(\theta)\cos^2(\theta)\right] d^3\mathbf{r} \end{aligned} \tag{C85}$$

This then becomes:

$$E_{a,4} = -\frac{1}{2M_s} 4M_s H_{a,2} \cos^3(\theta)\sin(\theta)\sum_{\mathbf{k}} m_X - \frac{1}{2M_s} H_{a,2}\left[\cos(2\theta)+\cos(4\theta)\right]\sum_{\mathbf{k}} m_X m_X^* - \frac{1}{2M_s} 2H_{a,2}\cos^4(\theta)\sum_{\mathbf{k}} m_Y m_Y^* \quad \text{C86}$$

Now that all of the energy terms have been expressed in this way, we can sum up all of the different terms. We will start by looking at all of the linear terms. They should (theoretically) cancel out.

$$E_{\text{linear}} = -\sum_{\mathbf{k}}\left[H_{\text{ext}}\sin(\theta_H - \theta) + 2\pi M_s \sin(2\theta) - \frac{1}{2}H_{a,1}\sin(2\theta) + 2H_{a,2}\cos^3(\theta)\sin(\theta)\right] m_X \quad \text{C87}$$

We will now use the equilibrium condition to determine whether this indeed does cancel. For the uniform mode, the energy density is:

$$F = -\mathbf{M}\cdot\mathbf{H}_{\text{ext}} - \left(K_{u,1} + 2K_{u,2}\right)\cos^2(\theta) + 2\pi M_s^2\cos^2(\theta) + K_{u,2}\cos^4(\theta) \quad \text{C88}$$

The equilibrium condition here (where the derivative is equal to 0) has been published by Iihama et al. and Beaujour et al. ([48] and [106]) to be:

$$H_{\text{ext}}\sin(\theta_H - \theta) - \frac{1}{2}\left(\frac{2K_{u,1}}{M_s} + \frac{4K_{u,2}}{M_s} - 4\pi M_s\right)\sin(2\theta) + \frac{1}{2}\left(\frac{4K_{u,2}}{M_s}\right)\cos^2(\theta)\sin(2\theta) = 0 \quad \text{C89}$$

Using the definitions for the anisotropy fields presented earlier in this document, rewrite this equilibrium condition:

$$H_{a,1} = \frac{2K_{u,1}}{M_s} + \frac{4K_{u,2}}{M_s} \quad \text{C90}$$

$$H_{a,2} = \frac{2K_{u,2}}{M_s} \quad \text{C91}$$

These terms will leave you with:

$$H_{\text{ext}}\sin(\theta_H - \theta) - \frac{1}{2}H_{a,1}\sin(2\theta) + 2\pi M_s\sin(2\theta) + 2H_{a,2}\cos^3(\theta)\sin(\theta) = 0 \quad \text{C92}$$

This means that $E_{\text{linear}} = 0$, which is a promising result because only the quadratic or higher terms should impact the dynamics.

Let's now organize the energy to be in the form of:

$$E = \frac{1}{2M_s}\sum_{\mathbf{k}} H_{xx,k} m_X m_X^* + H_{yy,k} m_Y m_Y^* + H_{xy,k} m_X m_Y^* + H_{yx,k} m_Y m_X^* \; . \quad \text{C93}$$

This form can only be achieved if:

$$H_{xx,k} = H_{\text{ext}}\cos\left(\theta_{\text{H}} - \theta\right) + H_{a,1}\cos\left(2\theta\right) - H_{a,2}\left(\cos\left(2\theta\right) + \cos\left(4\theta\right)\right) + 4\pi M_{\text{s}}\left[-\left(\left(N_k - 1\right)\cos^2\left(\varphi_k\right) + 1\right)\cos^2\left(\theta\right) + N_k\sin^2\left(\theta\right)\right] + Dk^2 \quad \text{C94}$$

$$H_{yy,k} = H_{\text{ext}}\cos\left(\theta_{\text{H}} - \theta\right) + H_{a,1}\cos^2\left(\theta\right) - 2H_{a,2}\cos^4\left(\theta\right) - 4\pi M_{\text{s}}\left[\left(N_k - 1\right)\sin^2\left(\varphi_k\right) + \cos^2\left(\theta\right)\right] + Dk^2 \quad \text{C95}$$

$$H_{xy,k} = H_{yx,k} = -2\pi M_{\text{s}}\left(N_k - 1\right)\sin\left(2\varphi_k\right)\cos\left(\theta\right) \quad \text{C96}$$

I'm going to skip a few steps and just say that the frequency dispersion (with small damping) can then be given by:

$$\omega\left(\mathbf{k}\right) = \gamma\sqrt{H_{xx,k}H_{yy,k} - H_{xy,k}^2} \quad \text{C97}$$

We can check that this is the correct result by trying to find the frequency of the uniform mode ($k = 0$). Plugging $k = 0$ into Eqs. C94 – C96 gives:

$$H_{xx,0} = H_{\text{ext}}\cos\left(\theta_{\text{H}} - \theta\right) + \left(H_{a,1} - 4\pi M_{\text{s}}\right)\cos\left(2\theta\right) - H_{a,2}\left(\cos\left(2\theta\right) + \cos\left(4\theta\right)\right) \quad \text{C98}$$

$$H_{yy,0} = H_{\text{ext}}\cos\left(\theta_{\text{H}} - \theta\right) + \left(H_{a,1} - 4\pi M_{\text{s}}\right)\cos^2\left(\theta\right) - 2H_{a,2}\cos^4\left(\theta\right) \quad \text{C99}$$

$$H_{xy,0} = H_{yx,0} = 0 \quad \text{C100}$$

This gives exactly the same frequency as the uniform mode in [48] (except the H_{xx} and H_{yy} are backwards).

Sometimes we use a simplification that reduces the dispersion to the form:

$$\omega^2\left(\mathbf{k}\right) = \omega_0^2 - Ak + BDk^2\,. \quad \text{C101}$$

I will attempt to do that here. Start by rewriting $H_{xx,k}$ and $H_{yy,k}$ in terms of $H_{xx,0}$ and H_{yy},0.

$$H_{xx,k} = H_{xx,0} + 4\pi M_{\text{s}}\left(N_k - 1\right)\left[\sin^2\left(\theta\right) - \cos^2\left(\varphi_k\right)\cos^2\left(\theta\right)\right] + Dk^2 \quad \text{C102}$$

$$H_{xx,k} = H_{xx,0} + 4\pi M_{\text{s}}\left(N_k - 1\right)\left[\sin^2\left(\varphi_k\right)\cos^2\left(\theta\right) - \cos\left(2\theta\right)\right] + Dk^2 \quad \text{C103}$$

$$H_{yy,k} = H_{yy,0} - 4\pi M_{\text{s}}\left(N_k - 1\right)\sin^2\left(\varphi_k\right) + Dk^2 \quad \text{C104}$$

This turns out to be the same result as that expressed in Beaujour et al. and Landeros et al. with the two important assumptions/changes [106] and [52].

$$\varphi = \frac{\pi}{2} - \theta \quad \text{C105}$$

$$N_k = 1 - \frac{kd}{2} \quad \text{C106}$$

DAMPING CAUSED BY TWO-MAGNON SCATTERING

I will use the methods laid out by Krivosik et al. to determine the amount of increased damping caused by a magnon dispersion [138]. This 2007 paper discusses the process of extracting the complex resonance conditions using methods from quantum mechanics (starting from a Hamiltonian and using the Primakoff transformations). The result is the expression:

$$i\tilde{\omega} + \tilde{\eta} = i\sum_{\mathbf{k}\neq 0}\left\{\frac{\left|G_{0,\mathbf{k}}\right|^2}{\omega_0 - \omega_{\mathbf{k}} + i\eta_{\mathbf{k}}} - \frac{\left|F_{0,\mathbf{k}}\right|^2}{\omega_0 + \omega_{\mathbf{k}} + i\eta_{\mathbf{k}}}\right\} . \qquad \text{C107}$$

For most situations of interest (near resonance), the second term is negligible, so we only need an expression for the first term. Krivosik et al. also provide an expression for this term that is a function of "inhomogeneous stiffness field tensor components" $\left\langle \tilde{h}_{ij}^2 \right\rangle$ that represent a field associated with some form of inhomogeneity. For most purposes, it is assumed that the inhomogeneity is a random perturbation field ($\tilde{h}$), which we will simplify the first term in Eq. C107.

$$\left|G_{0,\mathbf{k}}\right|^2 = \tilde{h}^2 \frac{\gamma^2}{\alpha^2}\frac{\eta_0\eta_{\mathbf{k}}}{\omega_0\omega_{\mathbf{k}}}C_{\mathbf{k}} \qquad \text{C108}$$

In the ultrathin film limit, the correlation function *C* is given by:

$$C_{\mathbf{k}} = \frac{8\pi}{A}\frac{\xi^2}{\left[1+\left(k\xi\right)^2\right]^{3/2}} . \qquad \text{C109}$$

For the ease of fitting the data, I will incorporate this area term (*A*) into the perturbation field ($\tilde{h}$) which one will have to remember has the units of field per area. We now combine these equations to determine the enhanced relaxation from two-magnon scattering:

$$\eta_{2\text{mag}} = \frac{\gamma^2}{\alpha^2}\frac{\eta_o}{\omega_0}\tilde{h}^2\sum_{\mathbf{k}\neq 0}\frac{1}{\omega_{\mathbf{k}}}\frac{\eta_{\mathbf{k}}^2}{\eta_{\mathbf{k}}^2 + \left(\omega_0 - \omega_{\mathbf{k}}\right)^2}\frac{\xi^2}{\left[1+\left(k\xi\right)^2\right]^{3/2}} . \qquad \text{C110}$$

To compare this model to theory, one would use two fitting parameters: x which is the size of the inhomogeneity, and h which is the amplitude of inhomogeneity. Because *h* is a constant coefficient, it will not influence the trend of the relaxation rate, whereas ξ will greatly influence the results.

APPENDIX D: LANDAU-LIFSHITZ-BLOCH EQUATIONS

As the research starts to look more into temperature dependence, I have started to incorporate the Landau-Lifshitz-Bloch equation. In this section, I would like to list some of the equations that are important to the macrospin simulations and understanding based on Garanin et al. [208]. First start with the LLB equation:

$$\frac{d\mathbf{M}}{dt} = -\gamma \mathbf{M} \times \mathbf{H}_{\text{eff}} + \frac{\alpha_{\|} \gamma M_0}{M_s^2} \mathbf{M} \left(\mathbf{M} \cdot \mathbf{H}_{\text{eff}} \right) - \frac{\alpha_{\perp} \gamma M_0}{M_s^2} \mathbf{M} \times \left(\mathbf{M} \times \mathbf{H}_{\text{eff}} \right) \tag{D1}$$

where

$$\alpha_{\perp} = \begin{cases} \left(1 - \frac{T}{3T_C} \right) \alpha_0 & T < T_C \\ \frac{2T}{3T_C} \alpha_0 & T \geq T_C \end{cases} \tag{D2}$$

$$\alpha_{\|} = \frac{2T}{3T_C} \alpha_0 \tag{D3}$$

where the subscript "0" indicates the values when the temperature is 0 K.

ANALYTICAL RESULTS OF THE LLB

Following the steps laid out in Appendix B, the result is the matrix:

$$\begin{bmatrix} \dot{\theta} \\ \dot{\varphi} \\ \dot{M}_s \end{bmatrix} = \begin{bmatrix} -\frac{\gamma}{M_s \sin(\theta)} F_{\theta\varphi} - \frac{\alpha_{\perp} \gamma M_0}{M_s^2} F_{\theta\theta} & -\frac{\gamma}{M_s \sin(\theta)} F_{\varphi\varphi} - \frac{\alpha_{\perp} \gamma M_0}{M_s^2} F_{\theta\varphi} & -\frac{\gamma}{M_s \sin(\theta)} F_{\varphi M} - \frac{\alpha_{\perp} \gamma M_0}{M_s^2} F_{\theta M} \\ \frac{\gamma}{M_s \sin(\theta)} F_{\theta\theta} - \frac{\alpha \gamma M_0}{M_s^2 \sin^2(\theta)} F_{\theta\varphi} & \frac{\gamma}{M_s \sin(\theta)} F_{\theta\varphi} - \frac{\alpha \gamma M_0}{M_s^2 \sin^2(\theta)} F_{\varphi\varphi} & \frac{\gamma}{M_s \sin(\theta)} F_{\theta M} - \frac{\alpha_{\perp} \gamma M_0}{M_s^2 \sin^2(\theta)} F_{\varphi M} \\ -\alpha_{\|} \gamma M_0 F_{M\theta} & -\alpha_{\|} \gamma M_0 F_{M\varphi} & -\alpha_{\|} \gamma M_0 F_{MM} \end{bmatrix} \begin{bmatrix} \Delta\theta \\ \Delta\varphi \\ \Delta M_s \end{bmatrix} \tag{D4}$$

This matrix is exactly like the matrix in B15 if two things are true: the system is at 0 K (indicated by $M_0 = M_s$) temperature and the saturation magnetization does not change in time. While the first assumption could be valid if $T << T_C$, that is never the case for my measurement. Provided that the change in T is small, the second assumption can be reasonable.

If it is assumed that M_s does not change in time and thus that ΔM_s is negligible, the result is that the relaxation time and resonance frequency found in Appendix B holds as long as the damping is redefined to be:

$$\alpha = \frac{M_0}{M_s} \left(1 - \frac{T}{3T_C} \right) \alpha_0 . \tag{D3}$$

For values much lower than T_C, this should provide a reasonable trend for damping. In fact, initial attempts to compare this equation to numerical results show that this is a very good assumption in most cases. To show this, Dingbin Huang and I made a series of numerical simulations conducted at various temperatures and with differing temperature rises on an arbitrary sample. We then

resulting simulated TR-MOKE signal to our standard LLG fitting process to extract damping. The result is shown in Fig. D1.

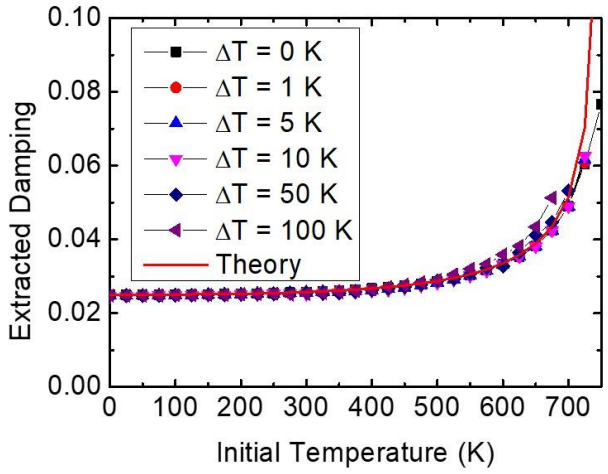

Figure D1. Comparison of the damping extracted from a macrospin LLB simulation with various temperature rises (ΔT) and the damping predicted from theory shown in Eq. D3. The magnetic properties input into the simulation are: M_0 = 1000 emu/cc, $K_{u,0}$ = 10 Merg/cc, α_0 = 0.025, and T_C = 750 K. The determination of temperature dependent properties of anisotropy and magnetization are determined through methods outlined in the next section.

LLB SIMULATIONS

While we have shown that it is often safe to make the assumptions necessary to just use a simplified expression for damping, having access to a macrospin LLB simulation allows to simulate more cases. For all of the LLB simulations that I ran, I made use of a few simplifications or equations to allow for testing these simulations.

The main difference between my simplified model and real macrospin simulations is in the inclusion of the "restorative field" (an additional field that acts along the direction of magnetization that acts to lengthen the magnetization when the current M_s does not equal the equilibrium M_s). Including this field into the effective field provides:

$$\mathbf{H}_{\text{eff}} = \mathbf{H}_{\text{ext}} + \mathbf{H}_{\text{ani}} + H_{\text{LLB}}\mathbf{m} \tag{D4}$$

where:

$$H_{\text{LLB}} = \begin{cases} \dfrac{1}{2\chi_{\parallel}}\left(1-\left(\dfrac{m}{m_{\text{eq}}}\right)^2\right) & T < T_C \\ -\dfrac{1}{\chi_{\parallel}}\left(1+\dfrac{3T_C m^2}{5(T-T_C)}\right) & T \geq T_C \end{cases}. \tag{D5}$$

In these equations, we make use of the value m which stands for the normalized magnetization at the current time step, and also m_{eq}, the equilibrium normalized magnetization (i.e., m_{eq} is M_s at that temperature normalized by M_0). The longitudinal susceptibility ($\chi_{\parallel}$) is defined as:

$$\chi_{\parallel} \equiv \frac{\partial m}{\partial H} = g\mu_s \frac{\beta L'}{1-\beta L' 3k_B T_C}. \qquad \text{D6}$$

where L' is the derivative of the Langevin equation (shown in Eq. 3.6). The right equal sign is only true with the application of the mean field theory (which is also discussed in section 3.3.2). For temperature dependent anisotropy, we use the theoretical equation presented by Mryasov et al [219]:

$$K_u(T) = \left(\alpha_K \left(\frac{M_s}{M_0} \right)^2 + (1-\alpha_K) \left(\frac{M_s}{M_0} \right)^3 \right) K_{u,0}. \qquad \text{D5}$$

where I let $\alpha_K = 0.91$. In the future, it would be better to have real measurements for temperature dependent magnetization and anisotropy.

The actual numerical algorithm used is a 4th order Runge-Kutta. A 1st order Runge-Kutta (a forward Euler approach) works fine, but we find it requires smaller time steps in order to converge.